



# Dynamic behavior of microcapsule flowing through microchannel

Xing-Yi Wang

## ► To cite this version:

Xing-Yi Wang. Dynamic behavior of microcapsule flowing through microchannel. Biomechanics [physics.med-ph]. Université de Technologie de Compiègne, 2021. English. NNT : 2021COMP2620 . tel-03642068

**HAL Id: tel-03642068**

**<https://theses.hal.science/tel-03642068>**

Submitted on 14 Apr 2022

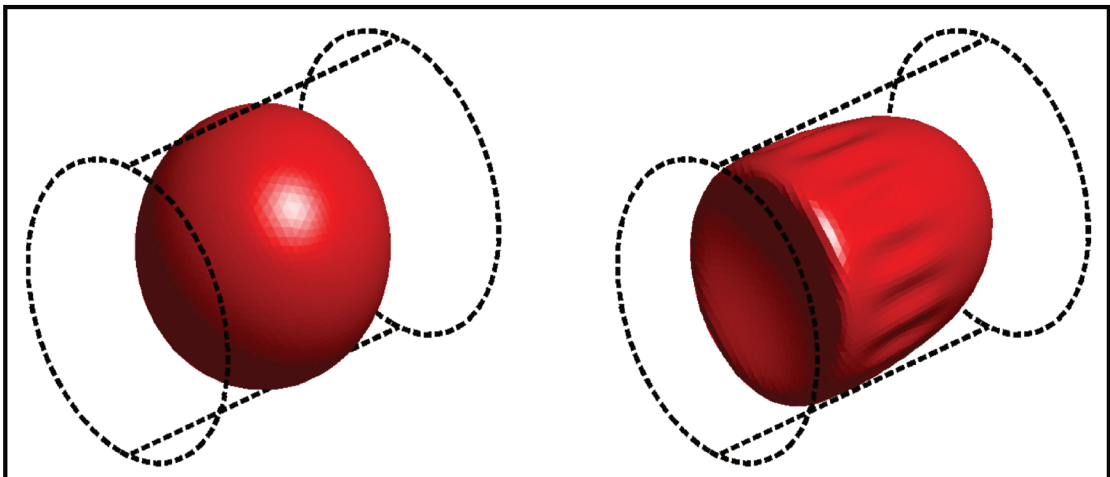
**HAL** is a multi-disciplinary open access archive for the deposit and dissemination of scientific research documents, whether they are published or not. The documents may come from teaching and research institutions in France or abroad, or from public or private research centers.

L'archive ouverte pluridisciplinaire **HAL**, est destinée au dépôt et à la diffusion de documents scientifiques de niveau recherche, publiés ou non, émanant des établissements d'enseignement et de recherche français ou étrangers, des laboratoires publics ou privés.

Par **Xing-Yi WANG**

*Dynamic behavior of microcapsule flowing  
through microchannel*

Thèse présentée  
pour l'obtention du grade  
de Docteur de l'UTC



Soutenue le 8 juillet 2021

**Spécialité** : Biomécanique : Unité de Recherche Biomécanique  
et Bio-ingénierie (UMR-7338)

D2620



Thèse présentée pour l'obtention du grade de Docteur de  
Université de Technologie de Compiègne

Réalisée au sein du du Laboratoire de BioMécanique et BioIngénierie  
de l'Université de Technologie de Compiègne

**Discipline : Biomécanique**

---

# Dynamic behavior of microcapsule flowing through microchannel

---

**PAR : Xing-Yi Wang**

MEMBRES DU JURY:

M <sup>me</sup> Delphine BRANCHERIE	Université de Technologie de Compiègne	Présidente
M. Simon MENDEZ	Université de Montpellier	Rapporteur
M. José-Maria FULLANA	Université Pierre et Marie Curie	Rapporteur
M <sup>me</sup> Anne-Virginie SALSAC	Université de Technologie de Compiègne	Directrice de Thèse
M <sup>me</sup> Dominique BARTHÈS-BIESEL	Université de Technologie de Compiègne	Directrice de Thèse
M <sup>me</sup> Marina VIDRASCU	Inria Paris	Invitée
M. Patrick LE TALLEC	École Polytechnique	Invité
M. Xu-Qu HU	Université de Hunan, Chine	Invité

**Date de soutenance : 08 juillet 2021**





# Acknowledgements

---

I would like to express my sincere gratitude to all those who have helped me during my life at UTC.

My deepest gratitude goes first and foremost to Dr. Anne-Virginie Salsac and Prof. Dominique Barthès-Biesel, my supervisors, for their constant and illuminating guidance. My knowledge and abilities have improved rapidly in the past three and a half years. Without their pushing me ahead, the completion of this thesis would be impossible. It is memorable and passionate to work together with them.

I am deeply grateful to Dr. Marina Vidrascu and Prof. Patrick Le Tallec, who have provided plenty of invaluable help and constructive suggestions during my Ph.D. It is a great honor to cooperate with them, and I have benefited a lot. I would also like to thank the rest of my committee members, Prof. Delphine Brancherie, Prof. José-Maria Fullana, and Dr. Simon Mendez, for their participation and organization of my defense.

I must thank Dr. Claire Dupont and Dr. Adlan Merlo for their selfless contributions to help me finish this dissertation. I appreciate the time working with my office colleagues, Clément and Nicolas. I thank all suggestions I received from teachers and colleagues in the team IFSB of laboratory BMBI, especially Badr. I also thank all my friends at UTC for their kind help to make my study and life in France a wonderful time.

I would like to extend my special thanks to Prof. Xu-Qu Hu for his continuous encouragement and advice at every stage of my postgraduate life. My appreciation also goes to my parents and my girlfriend Xinxin for their spiritual encouragement and support all through my studies.

Finally, I must thank the financial support from CSC. It is my fortune to have the opportunity to do my study in France with the help of CSC.

---

# Contents

---

<b>Abstract</b>	<b>vii</b>
<b>Résumé</b>	<b>ix</b>
<b>Principal notations</b>	<b>xi</b>
<b>1 Introduction</b>	<b>1</b>
1.1 Capsule in confined flow: definition and application . . . . .	1
1.2 Capsule motion and deformation in a straight channel . . . . .	3
1.2.1 Numerical simulations . . . . .	4
1.2.1.1 Analytical model . . . . .	4
1.2.1.2 Axisymmetric model . . . . .	5
1.2.1.3 Membrane model . . . . .	6
1.2.1.4 Shell model . . . . .	8
1.2.2 Experimental observations . . . . .	9
1.3 Determination of capsule membrane mechanical properties . . . . .	11
1.3.1 Compression and micropipette aspiration . . . . .	11
1.3.2 Flow in microfluidic channel . . . . .	12
1.4 Objectives . . . . .	14
<b>2 Mechanics of a capsule in confined flow</b>	<b>15</b>
2.1 Problem description . . . . .	15
2.2 Fluid problem . . . . .	17
2.2.1 Internal and external flows . . . . .	17
2.2.2 Boundary integral formulation . . . . .	18
2.3 Solid problem . . . . .	19
2.3.1 Geometric definition of a shell . . . . .	19
2.3.2 Differential geometry on mid-surface and shell . . . . .	21
2.3.3 Shell kinematics . . . . .	22
2.3.4 Constitutive law . . . . .	24
2.3.5 Shell equilibrium . . . . .	25
2.3.6 Shell mathematical model . . . . .	26

---

2.4	Numerical implementation . . . . .	27
2.4.1	Mesh discretization for capsule and channel . . . . .	28
2.4.2	Finite element formulation for shell equilibrium . . . . .	31
2.4.3	Boundary integral formulation for capsule flow . . . . .	33
2.4.4	Coupling Shell FEM + BIM procedure . . . . .	34
2.5	Validation . . . . .	35
2.5.1	Convergence study . . . . .	35
2.5.2	Comparison with membrane model . . . . .	37
<b>3</b>	<b>Capsule in unbounded parabolic flow</b>	<b>39</b>
3.1	Validation . . . . .	40
3.2	Capsule axial deformation . . . . .	41
3.3	Bending energy-curvature relationship . . . . .	44
3.3.1	Physical model accounts for bending . . . . .	44
3.3.2	Comparison of bending measurement . . . . .	46
3.3.3	Comparison of bending energy density . . . . .	48
3.4	Discussion . . . . .	51
3.5	Conclusion . . . . .	52
<b>4</b>	<b>Capsule in bounded Poiseuille flow</b>	<b>53</b>
4.1	Application condition . . . . .	54
4.2	Capsule axial deformation . . . . .	55
4.3	Effect of capsule size . . . . .	58
4.4	Capsule typical curvature . . . . .	59
4.5	Membrane wrinkle . . . . .	61
4.6	Experimental observation . . . . .	65
4.7	Identification of membrane thickness . . . . .	66
4.7.1	Wrinkle measurement . . . . .	66
4.7.2	Curvature measurement . . . . .	68
4.8	Identification of bending modulus . . . . .	68
4.9	Conclusion . . . . .	69
<b>5</b>	<b>Membrane property determination</b>	<b>71</b>
<b>6</b>	<b>Conclusions and perspectives</b>	<b>91</b>
6.1	Conclusions . . . . .	91
6.2	Perspectives . . . . .	92
<b>A</b>	<b>Formula derivation</b>	<b>97</b>



---

# Abstract

---

Microcapsules are liquid droplets enclosed by an elastic membrane. They are in practice often subjected to confined flow fields where the membrane withstands hydrodynamic forces and exhibits complex buckling behaviors, such as a parachute shape or wrinkles. The capsule dynamic behavior depends on membrane mechanical properties. However, conventional approaches for measuring membrane properties are difficult since capsules are micron-sized and fragile. Subjecting capsule suspensions to hydrodynamic stresses under controlled flow conditions facilitates capsule manipulation. But a numerical model is necessary to get a deeper understanding of capsule motion and deformation and determine the membrane mechanical properties of artificial capsules.

We construct a three-dimensional numerical model for a liquid-filled capsule flowing in a cylindrical channel. The internal and external flows are in the Stokes flow regime, and the membrane is assumed to be a thin shell characterized by a mid-surface and a finite thickness. The fluid-structure interaction problem is solved by coupling a Boundary Integral Method for capsule flow with a Shell Finite Element Method for shell deformation. This model is adapted to a confined flow case for the first time to fulfill three main objectives. (i) Investigate the effect of membrane bending resistance and channel confinement on capsule mechanical behaviors. (ii) Investigate the relationship between membrane bending energy and curvature. (iii) Determine membrane mechanical properties for a population of artificial capsules.

The numerical model is first tested in unbounded parabolic flow. The results obtained for different wall thicknesses and flow strengths indicate that the bending energy density is not a quadratic function of mean curvature change. We next consider the case in which an initially spherical capsule flows in a straight cylindrical channel. The corresponding study consists of (i) investigating capsule rheological behavior when the membrane is governed by a neo-Hookean (NH) or a generalized Hooke's (GH) law and (ii) exploring capsule dynamic responses for different wall thicknesses or bending resistances. The simulation results show that under high flow strength, a membrane governed by NH law exhibits strain-softening elastic behavior, while it is strain-hardening for membrane governed by GH law. The bending resistance is found to restrict capsule deformation for a given flow strength. When the capsule flows in a tube with comparable dimensions, wrinkles may be present at steady-state due to channel confinement effects depending on wall thickness

and flow strength. We find a constitutive relationship between wrinkle wavelength and shell thickness when the membrane rheological behavior follows the NH law.

In order to characterize membrane mechanical properties, we have performed experiments with flowing capsules in a cylindrical capillary tube. An automatic microfluidic method is proposed for measuring the elastic properties of a population of microcapsules based on experimental observation and analysis of their deformed profiles. We find that ovalbumin membrane exhibits strain-softening elastic behavior since a fairly constant value of membrane elastic modulus is found by assuming NH law. Using indirect inverse analyses, it is possible to determine membrane thickness by means of measuring wavelengths or rear bending curvatures from experimental images.

The present work combines numerical simulations with microfluidic experiments through inverse analysis techniques, which provide flexible approaches to measure membrane elastic properties and further extend to the characterization of finite thickness walls.

**Keywords:** Microcapsule, fluid-structure interaction, numerical model, buckling and wrinkling, microfluidics, inverse analysis technique, membrane property, wall thickness



# Résumé

---

Les microcapsules sont des gouttelettes entourées d'une membrane élastique. Elles sont en pratique souvent soumises à des écoulements confinés où la membrane résiste aux forces hydrodynamiques et présente des comportements de flambage complexes, comme une forme de parachute ou des plis. Le comportement dynamique de la capsule dépend des propriétés mécaniques de la membrane. Cependant, les approches conventionnelles pour mesurer les propriétés de la membrane sont difficiles à appliquer car les capsules sont de très petite taille et fragiles. Soumettre les suspensions de capsules à des contraintes hydrodynamiques dans des conditions d'écoulement contrôlé facilite la manipulation des capsules. Un modèle numérique est alors nécessaire pour mieux comprendre le mouvement et la déformation de la capsule et déterminer les propriétés mécaniques de la membrane des capsules artificielles.

Nous construisons un modèle numérique tridimensionnel d'une capsule à coeur liquide s'écoulant en écoulement dans un canal cylindrique. Les écoulements internes et externes sont des écoulements de Stokes, et la membrane est supposée être une coque mince caractérisée par une surface moyenne et une épaisseur finie. Le problème d'interaction fluide-structure est résolu en couplant une méthode des intégrales de frontière pour l'écoulement de la capsule avec une méthode d'éléments finis de coque pour la déformation de la coque. Ce modèle est adapté pour la première fois à un cas d'écoulement confiné pour remplir trois objectifs principaux. (i) Étudier l'effet de la résistance à la flexion de la membrane et du confinement du canal sur le comportement mécanique de la capsule. (ii) Étudier la relation entre l'énergie de flexion de la membrane et la courbure. (iii) Déterminer les propriétés mécaniques de la membrane pour une population de capsules artificielles.

Le modèle numérique est d'abord testé dans un écoulement parabolique infini. Les résultats obtenus pour différentes épaisseurs de la membrane et différentes forces d'écoulement indiquent que la densité d'énergie de flexion n'est pas une fonction quadratique du changement de courbure moyenne. Nous considérons ensuite le cas dans lequel une capsule initialement sphérique s'écoule dans un canal cylindrique rectiligne. L'étude correspondante consiste à (i) étudier le comportement rhéologique de la capsule lorsque la membrane est régie par une loi néo-hookéenne (NH) ou de Hooke généralisée (GH) et (ii) explorer les réponses dynamiques de la capsule pour différentes épaisseurs de la membrane ou résistances à la flexion. Les résultats des simulations montrent que sous une

force d'écoulement importante, une membrane régie par la loi NH présente un comportement élastique adoucissant (strain-softening), alors qu'il est renforçant (strain-hardening) pour une membrane régie par la loi GH. On constate que la résistance à la flexion limite la déformation de la capsule pour une force d'écoulement donnée. Lorsque la capsule s'écoule dans un tube de dimensions comparables, des plis peuvent être présents à l'état stationnaire en raison des effets de confinement du canal dépendants de l'épaisseur de la membrane et de la force d'écoulement. Nous trouvons une relation constitutive entre la longueur d'onde des plis et l'épaisseur de la membrane lorsque le comportement rhéologique de la membrane suit la loi NH.

Afin de caractériser les propriétés mécaniques de la membrane, nous avons réalisé des expériences avec des capsules en écoulement dans un tube capillaire cylindrique. Une méthode microfluidique automatique est proposée pour mesurer les propriétés élastiques d'une population de microcapsules basée sur l'observation expérimentale et l'analyse de leurs profils déformés. Nous constatons qu'une membrane en ovalbumine présente un comportement élastique adoucissant puisqu'une valeur relativement constante du module élastique de la membrane est trouvée en supposant la loi NH. En utilisant des analyses inverses indirectes, il est possible de déterminer l'épaisseur de la membrane en mesurant des longueurs d'onde ou des courbures de flexion à l'arrière de la capsule à partir d'images expérimentales.

Le présent travail combine des simulations numériques avec des expériences microfluidiques à travers des techniques d'analyse inverse, qui fournissent des approches modulables pour mesurer les propriétés élastiques de la membrane et s'étendent d'autre part à la caractérisation des membranes d'épaisseur finie.

**Mots clés:** Microcapsule, interaction fluide-structure, modèle numérique, flambage et plissement, microfluidique, technique d'analyse inverse, propriété de membrane, épaisseur de membrane

# Principal notations

---

## Latin symbols

$a$	Radius of initially spherical capsule.
$\underline{\underline{a}}$	2D metric tensor.
$\underline{a}_1, \underline{a}_2, \underline{a}_3$	Covariant base vectors in the current configuration.
$\underline{\underline{A}}_1, \underline{\underline{A}}_2, \underline{\underline{A}}_3$	Covariant base vectors in the reference configuration.
$Ca_v$	Bulk capillary number.
$Ca_s$	Surface capillary number.
$\underline{\underline{C}}_s$	Cauchy-Green deformation tensor.
$C^{\alpha\beta\lambda\mu}$	Plane-stress in-plane constitutive coefficient.
$D^{\alpha\lambda}$	Plane-stress transverse constitutive coefficient.
$\underline{\underline{e}}$	3D Green-Lagrange strain tensor.
$\underline{\underline{e}}_s$	2D Green-Lagrange strain tensor.
$\underline{e}_1, \underline{e}_2, \underline{e}_3$	Cartesian base.
$\underline{f}$	Disturbance wall friction.
$\underline{\underline{F}}$	3D Transformation gradient.
$\underline{\underline{F}}_s$	2D transformation gradient.
$G$	Bulk shear modulus.
$G_s$	Surface shear modulus.
$\underline{\underline{g}}$	3D metric tensor.
$\underline{g}_1, \underline{g}_2, \underline{g}_3$	3D covariant base in the current configuration.
$\underline{\underline{G}}_1, \underline{\underline{G}}_2, \underline{\underline{G}}_3$	3D covariant base in the reference configuration.
$I_{s1}, I_{s2}$	Invariants of the 2D transformation.
$J$	Jacobian.
$\underline{\underline{J}}$	Green kernel.
$K_M, K_G$	Mean and Gaussian curvatures.
$K_0$	Curvature in the reference configuration.
$K_\varphi$	Curvature in the meridional plane.
$K_b$	Bending number.
$K_s$	Area dilatation modulus.
$l$	Hydraulic radius of the channel.

$L_z, L_y, L_p$	Typical lengths of deformed capsule.
$M_b$	Bending modulus.
$\underline{q}$	Viscous load exerted by the fluids on the shell.
$\underline{q}_s$	Viscous load exerted by the fluids on the mid-surface.
$Re$	Reynolds number.
$r, s, z$	Intrinsic local Cartesian coordinates.
$S_t$	Mid-surface of capsule membrane.
$\underline{\underline{T}}$	Cauchy stress tensor.
$\underline{u}$	Displacement field.
$\underline{v}$	Velocity field of the fluids.
$\underline{v}^\infty$	Undisturbed velocity of the fluids.
$V$	Flow characteristic velocity.
$w_s$	Strain energy density.
$\underline{x}$	Position vector in the current configuration.
$\underline{X}$	Position vector in the reference configuration.

## Greek symbols

$\alpha$	Wall thickness ratio
$\underline{\underline{\gamma}}$	Membrane strain tensor.
$\underline{\underline{\chi}}$	Bending strain tensor.
$\underline{\underline{\zeta}}$	Shear strain tensor.
$\delta^\alpha_\beta$	Kronecker symbol.
$\eta$	Capsule wall thickness.
$\underline{\theta}$	Rotation vector.
$\underline{\underline{\kappa}}$	Curvature tensor.
$\lambda$	Viscosity ratio between the internal and external fluids.
$\lambda^{(i)}$	Shape functions.
$\lambda_{s1}, \lambda_{s2}$	Surface principal dilatation ratio.
$\mu$	Viscosity of the external fluid.
$\nu$	Poisson ratio.
$\nu_s$	Surface Poisson ratio.
$\xi^1, \xi^2, \xi^3$	Curvilinear coordinates.
$\underline{\underline{\Sigma}}$	3D Piola-Kirchhoff stress tensor.
$\underline{\underline{\Sigma}}_s$	2D Piola-Kirchhoff tension tensor.
$\underline{\Phi}$	3D chart.
$\underline{\phi}$	2D chart.

$\rho$	Fluid density.
$\underline{\sigma}$	Stress field of the fluids.
$\underline{\underline{\psi}}$	Bending deformation tensor.
$\underline{\underline{\Psi}}_M, \underline{\underline{\Psi}}_G$	Mean and Gaussian bending deformation.
$\Delta P$	Disturbance pressure drop.
$\Delta P^\infty$	Undisturbed pressure drop.
$\Delta t$	Time step.
$\Delta x$	Mesh size.

## Other symbols

$\mathcal{F}$	Laboratory reference frame.
$\mathbb{R}^3$	3D mathematical space.
$\mathbb{R}^2$	2D mathematical space.
$\mathcal{V}$	Sobolev space.
$\mathbb{I}$	Identity tensor.
$\nabla$	Divergent operator.
$\underline{\underline{\mathcal{H}}}_s$	2D elasticity tensor.
$\cdot_s$	Subscript used to identify the quantities relative to the mid-surface.



# Introduction

## 1.1 Capsule in confined flow: definition and application

Micro-capsules are liquid droplets surrounded by thin membranes. The membrane is semi-permeable and highly deformable, and acts as a protector to prevent (or control) the deterioration (or the release) of internal medium (Barthès-Biesel, 2016). Consequently, the membrane plays a significant role in regulating capsule dynamic response, which is different from rigid particles.

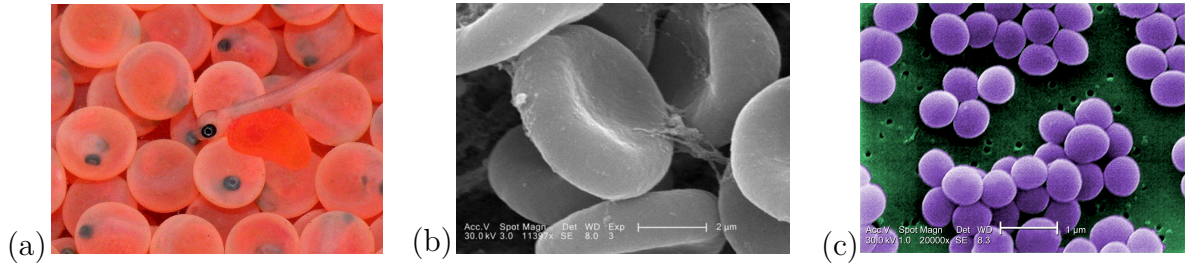


Figure 1.1 – Examples of various forms of capsules in nature. (a) Fish eggs (image from fishfarmingexpert.com); (b) Human red blood cells and (c) *Staphylococcus aureus* bacteria (images b and c from Janice Haney Carr, Centers for Disease Control, USA).

Biological capsules can be found in various forms in nature, for example, red blood cells (RBCs), fish eggs, bacteria, etc., as shown in figure 1.1. They are usually suspended in fluids, often in confined environments where combined hydrodynamic effects, including wall repulsive and viscous forces, are exerted onto the membranes (Elgeti *et al.*, 2010; Fedosov *et al.*, 2010). RBCs flowing in blood vessels is one prototypical case: on the one hand, compared with the tank-treading or tumbling motion in simple shear flow (Skotheim & Secomb, 2007; Dupire *et al.*, 2012), RBCs in confined conduits exhibit the parachute-like or slipper-like shapes with large deformations (Abkarian *et al.*, 2008; Zheng *et al.*, 2013; Kihm *et al.*, 2018). On the other hand, the irregularly bifurcating boundaries lead to non-uniform RBCs partitioning between daughter branches, affecting the transport of oxygen, carbon dioxide, or other nutrients in the living bodies (Clavica *et al.*, 2016). As a result, understanding the law of cell motion and deformation in a confined flow field becomes a necessity.

Encapsulation techniques fabricate artificial capsules that can either release the internal active substances (like aromas, flavors, and drugs) through the semi-permeable membrane and deform or even break up under control. (Barthès-Biesel, 2011). There are several prevalent methods of preparing capsules: (i) polymerization, including interfacial cross-linking (Peyratout & Daehne, 2004) or polycondensation (Janssen & Te Nijenhuis, 1992), (ii) coacervation (Stassen *et al.*, 1994), (iii) spray drying (I Ré, 1998). These controllable capsules have been widely used in many industries, such as cosmetics, pharmaceuticals, medical diagnosis and treatment, and bioengineering.

In cosmetics and pharmaceuticals, the encapsulation technique fulfills the controlled release of vulnerable and volatile aromas, fragrances, or drugs during application. Soft gelatin or various polymer capsules are usually applied due to their features of good biological compatibility, large bioavailability, easy solubility, high stability, etc., (Serajuddin *et al.*, 1986; Benza & Munyendo, 2011). For example, Ghirardi *et al.* (1977) found that the formulation of soft gelatin capsules showed a quicker dissolution rate and higher bioavailability of digoxin than a commercial tablet form. Miyazawa *et al.* (2000) fabricated a low oxygen permeability soft microcapsule for cosmetic applications, rendering no significant loss of oxygen-sensitive agents inside the capsule after the four-week experiments. Shalaka *et al.* (2009) enclosed Vitamin E by a membrane consisting of two natural polymers of pectin and sodium alginate, in which their ratios influenced the capsule properties.

In medical diagnosis and treatment, the polyelectrolyte multilayer microcapsules are commonly used in the drug delivery system. There are several advantages of such capsules (Petrov *et al.*, 2005; Johnston *et al.*, 2006): (i) high mildness of preparation conditions, (ii) diversified function of capsule shell (by varying the layer thickness or compositions), (iii) high scalability of capsule surface (by embedding organics such as lipids or proteins). It is worth noting that shell thickness and components greatly influence the capsule property and release efficiency of encapsulants. Dong *et al.* (2005) obtained a critical shell thickness to determine the capsule stability and shell integrity. Pavlov *et al.* (2011) improved the release efficiency as much as 4-fold by adding gold nanoparticles in the shell. Cuomo *et al.* (2015) employed a model to analyze the mechanism by which the permeability of small molecules decrease as the polyelectrolyte layer increases.

In bioengineering, an increasing number of researchers have explored new capsule preparation methods to fulfill the control of the shell thickness. Caruso (2000) synthesized a uniform hollow capsule with controlled size, geometry, and wall thickness (nanometer-sized) using colloidal templating and self-assembly processes. Yang *et al.* (2013) developed a nanocomposite microcapsule by which the capsule size and shell thickness were tunable with varying the concentration of silica nanoparticles in the interfacial polymerization. Similar studies are numerous. However, using microfluidic devices to fabricate



thickness-controllable capsules show high potentials. Various microfluidic flow-focusing devices are employed to generate size-controlled biphasic droplets in the first place. Then the core-shell geometry is formed by polymerization or other physical or chemical methods. For example, with the help of microfluidic devices shown in Fig. 1.2, Kim *et al.* (2011) produced stable microcapsules with ultra-thin shells of a few tens of nanometers, and Nisisako & Hatsuzawa (2016) generated microcapsules with a shell thickness ratio that can vary in a wide range of 0.4 – 30%.

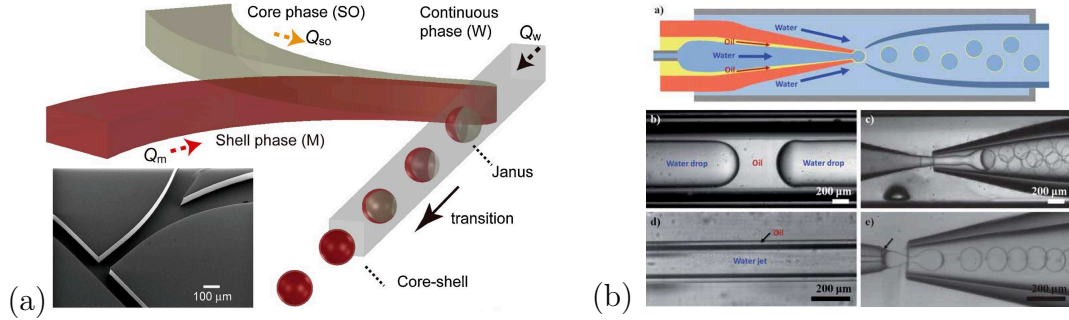


Figure 1.2 – Various microfluidic devices for producing biphasic droplets. (a) Image from Nisisako & Hatsuzawa (2016); (b) Image from Kim *et al.* (2011).

From the above reviews, the shell thickness and confinement of the flow boundary are two significant factors in reality that can highly influence the capsule dynamic responses. A good understanding of this fluid-structure interaction problem benefits both industrial application and scientific research. Therefore, this dissertation specifically focuses on a fundamental case: the motion and deformation of a liquid-filled capsule with a finite-thickness membrane when it flows into a straight channel. The corresponding studies resort to experimental and numerical works.

## 1.2 Capsule motion and deformation in a straight channel

Unlike rigid particles and simple droplets that do not have elastic membranes, artificial capsules flowing in a tight tube exhibit fairly large deformations under high flow strengths and boundary confinements. Usually, the formation of a parachute-shape with sharp edges and high curvature increases the possibility of membrane ruptures. In the meantime, wrinkles would occur in the region facing the channel wall, revealing a combined effect of bending resistance, compressive forces, and channel confinements on the capsule membranes. Consequently, numerous numerical and experimental works have been devoted to study artificial capsules or cells' dynamic behaviors in microchannels, which are briefly summarized in this section.

### 1.2.1 Numerical simulations

Experimental studies on microcapsule behaviors are indispensable, but they are also difficult, costly, and time-consuming. Numerical methods and models have become a powerful tool in predicting and analyzing capsule deformations in the past few decades. In general, microfluidic flows correspond to low Reynolds number regimes by which viscous forces are dominated and, therefore, Stokes equations are used to describe the internal and external flows. A widely used membrane model assumes the membrane as a 2D hyperelastic isotropic surface, neglecting the thickness and bending resistance. The in-plane membrane deformation can be modeled by several constitutive laws. However, a physical membrane must be a finite thickness shell, and thus there are finite transverse forces across the thickness during deformation. Therefore, different bending theories are brought out to account for the membrane bending resistance. In this section, we briefly summarize the numerical works concerning microcapsules flowing through microchannels.

#### 1.2.1.1 Analytical model

The modeling of flow-induced capsule motion and deformation started in the early 1980s. Barthès-Biesel (1980) is the pioneer who provided the initial theoretical solution dealing with the deformation of an initially spherical capsule suspended in a linear shear flow. The internal and external flows were described by Stokes equations, while the dynamic equilibrium of viscous and elastic forces was solved through the regular perturbation analysis. This analytical study not only predicted the tank-treading motion but also revealed that the capsule orientation depends on the viscosity ratios. Barthès-Biesel later improved the model by reformulating the membrane mechanics according to Cartesian tensors in the same reference frame as the fluid problem. This model was used to study the time-dependent deformation of a capsule enclosed with a purely elastic membrane (Barthès-Biesel & Rallison, 1981), as well as the orientation and deformation of a capsule enclosed with a visco-elastic membrane (Barthès-Biesel & Sgaier, 1985).

If considering closely fitting cells in the tube, there is a thin liquid film in the narrow gaps between the cell and the wall, which allows the lubrication theory to solve the pressure gradient in the film. Secomb & Skalak (1982) used an approximate two-dimensional model to study the motion of asymmetry RBC in capillary flow. Lubrication theory solved the flow between the cell and the capillary wall. The driving pressure and resultant shear stresses maintained the cell shapes. This simplified model was able to predict the tank-treading motion resulting from the cell asymmetries. Secomb *et al.* (1986) later adapted this lubrication model for the motion of axisymmetric RBC shape in capillaries. The membrane shear- and bending- stresses were introduced together with the membrane tension to balance the external fluid forces. However, the membrane was assumed to be

two-dimensional without thickness, and bending moments were proportional to the curvature variation of the surface, widely known as Helfrich bending theory (Helfrich, 1973). A similar study can be found in Halpern & Secomb (1989), who studied the squeezing of RBCs through a very narrow tube, at which the cell presented a long slug shape with either convex or concave ends.

Analytical models opened a precedent for studying the flow-induced capsule deformation, however, they are only validated in the limit of small deformations while the non-linear problems of large deformations are usually involved. The initial capsule shapes are also restricted to spherical or specific ones. Therefore, accounting for large deformations and non-spherical capsule shapes call for numerical models.

### 1.2.1.2 Axisymmetric model

A variety of capsule models were successively developed to consider large deformations starting in the late 1980s. Due to computer limitations in the early days, initial numerical models only deal with axisymmetric situations when the capsule and channel are coaxial. The boundary integral method (BIM) became the first choice for solving the axisymmetric capsule deformations in various flows. The advantage is that the boundary integral formulation of the Stokes equations relates the velocity of any point in the fluid domain to the velocity and stresses on the capsule boundaries, which avoids solving the Stokes equations in the differential form over the whole flow fields. Details may be found in the book by Pozrikidis (1992). In this section, the axisymmetric model refers to the model for solving axisymmetric capsule flow based on the boundary integral technique.

The axisymmetric model was initially used to study the flow-induced deformation of gas bubbles (Youngren & Acrivos, 1976) and liquid droplets (Rallison & Acrivos, 1978). Then it was extended by Barthès-Biesel and the co-authors to study the large deformations of initially ellipsoidal capsules with a neo-Hookean type of membrane in an elongational flow (Li *et al.*, 1988). Large deformations were obtained by using a smoothing method to alleviate the problem of profile oscillations. One may be interested in the relevant studies of capsules in unbounded flows such as simple shear flow (Pozrikidis, 2001) or extensional flow (Diaz *et al.*, 2000; Kwak & Pozrikidis, 2001).

Incorporating boundary effects into the simulation were also initiated by Barthès-Biesel. Leyrat-Maurin & Barthès-Biesel (1994) modeled the transient motion of neo-Hookean type capsules through a hyperbolic constriction and the entry and exit phenomena through the pore were observed. They showed that the entry process forced the large capsule to have a maximum energy expenditure when it was 1 diameter away upstream of the throat. The entrance or exit plugging predicted by their model also showed a good agreement with experiments. Quéguiner & Barthès-Biesel (1997) studied the movements

of capsules with a neo-Hookean or area-incompressible membrane through a cylindrical channel with hyperbolic inlet and outlet. They concluded that the entrance length of capsules in the pore increased with capsule sizes and no sensitivity with downstream conditions. The elastic behavior of the membrane and the size of the capsule determined the channel length required to reach a steady state. Diaz & Barthès-Biesel (2001) supplemented the study of the influence of non-equal viscosity ratio (a ratio between internal and external fluids) on capsule flow in a cylindrical channel with a hyperbolic entrance. The viscosity ratio did not significantly impact the deformed profile for initially spherical capsules, while it greatly influenced the deformed shape for initially ellipsoidal ones. Lefebvre & Barthès-Biesel (2007) further studied the deformation of an initially pre-inflated capsule subjected to a channel flow. They concluded that the pre-swelling effects could enhance the membrane apparent rigidity and thus resisting the deformation. They also found that 3% pre-inflation for capsules with Skalak membrane can fit well with the experimental results of Risso *et al.* (2006). Afterward, Lefebvre *et al.* (2008) used the axisymmetric model to characterize the membrane mechanical properties by comparing the numerical and experimental results. This will be detailed in section 1.3.2.

The axisymmetric model is versatile, not only predicting a parachute-like or slug-like shape when the capsule flows into a channel but also determining the membrane properties by comparing with experimental data. However, how accurate the axisymmetric model used to analyze the capsule deformation is a question, which calls for more general three-dimensional (3D) numerical models.

### 1.2.1.3 Membrane model

Benefited from the development of computers and motivated by new experimental devices (Barthès-Biesel, 2011), full 3D models for capsule simulations have been developed since the 21st century. The capsule flow and membrane deformation can be solved independently and sequentially, and the fluid-solid interface is tracked with time evolutions. In brief, at a given time, the deformation of the nodes on the capsule surface is known by comparing the positions between the deformed and initial states. Thus the elastic forces of the membrane are computed by assuming a constitutive law. The membrane equilibrium condition leads to knowing viscous forces exerted by fluids on the interface. Then the fluid motion is solved from Stokes (or Navier-Stokes) equations. Finally, the integration of velocity over time gives rise to the new position of the membrane nodes. By convention, the membrane model refers to a type of model that assumes the capsule membrane as a two-dimensional infinitely thin surface without considering the thickness. Various numerical techniques are used for solving the fluid and solid problems.

Pozrikidis (2005) gave a general three-dimensional boundary integral formulations for the flow of capsules in a cylindrical channel. The hydrodynamics coupled with the membrane mechanics were solved by the boundary Integral method. The study simulated the initial capsule shape as spherical, oblate ellipsoidal, and biconcave ones enclosed by a neo-Hookean membrane. It found that off-center spherical capsules slowly migrated toward the channel centerline, and in-center discoidal capsules developed parachute-like shapes. However, this model suffers numerical instabilities when the capsule undergoes large deformations with in-plane compressive tensions.

Doddi & Bagchi (2008) investigated the lateral migration of an initially spherical capsule in a bounded Poiseuille flow using a hybrid model. The fluid problem was solved by a second-order finite difference scheme, and the fluid-capsule interaction was solved by a front-tracking technique based on immersed boundary method. They concluded that increasing the capillary number and capsule-to-channel size ratio could increase the migration velocity and capsule deformation while increasing the viscosity ratio and distance from the wall led to the opposite effects. Whereafter, Doddi & Bagchi (2009) adapted the same model to study the single- or multi-file motion of red blood cells in a straight tube.

In order to simulate the non-linear large deformations and tackle the instability caused by in-plane compressions, Walter *et al.* (2010) developed a coupled code based on boundary integral method (BIM) solving for the fluid problem and finite element method (FEM) solving for the solid problem. Although the membrane has been subjected to compressive forces, the inherent numerical stiffness introduced by FEM could maintain the simulation stable. Hu *et al.* (2012) further adapted this code to a confined flow field either for a circular-section or square-section channel. Because of channel confinement effects, the compressive forces in the middle of the capsule led to membrane wrinkles or folds, which could not be predicted by an axisymmetric model. However, this phenomenon is non-physical due to the lack of consideration of membrane bending resistance.

A linear constitutive law accounting for bending is Helfrich law, which assumes the energy resulting from bending is a quadratic function of the mean curvature (Helfrich, 1973). Thus the bending energy can be easily combined with the membrane elastic energy without assuming a three-dimensional membrane with a finite thickness. For example, Huang *et al.* (2012) employed an improved penalty immersed boundary method for simulating the capsule flow. The buckling and wrinkling phenomenon in the case of no bending resistance was suppressed after including the bending rigidity. Based on an immersed-boundary lattice Boltzmann code, Wang *et al.* (2016, 2018) studied the motion of a spherical capsule in branched tubes either with a circular cross-section or a square cross-section. Guckenberger *et al.* (2018) used a boundary integral model to study the shape bistability of red blood cells flowing in a microchannel. However, including

the bending rigidity in those studies is mainly used for resisting the numerical instabilities arising from the membrane buckling. The membrane folding or wrinkling can not be properly predicted. Besides, the bending modulus in membrane models is just a parameter independent of the material thickness, and unrealistic large values are usually used. Therefore, there is a necessity in developing numerical models accounting for the membrane thickness to study the effect of bending resistance on capsule deformations.

#### 1.2.1.4 Shell model

The mechanical response of capsules with a finite thickness membrane can be described by the Reissner-Mindlin shell or the Kirchhoff-Love shell (see Chapelle & Bathe, 2010, chap. 4). In the thin shell model, the membrane is assumed as a three-dimensional material characterized by a mid-surface and a finite thickness. A material line across the shell is initially orthogonal to the mid-surface and remains straight and unstretched during the deformations. For a given displacement field, the Reissner-Mindlin kinematical assumption states that the material line can rotate and no longer be normal to the mid-surface in the deformed state. In contrast, the Kirchhoff-Love kinematical assumption states that the material line is always orthogonal to the mid-surface in the course of deformations. Consequently, the Kirchhoff-Love assumption is stronger than the Reissner-Mindlin assumption due to no transverse shearing.

Le & Tan (2010) developed a thin shell model based on the Kirchhoff-Love assumption to simulate the capsule motion and deformation. This model allowed for thickness stretching, large deflections, and bending strains. The immersed boundary method was used for computing the hydrodynamics and fluid-structure interactions. The effect of bending resistance on capsule deformation in simple shear flow was subsequently studied by Le (2010), who found that raising bending stiffness could amplify the shape oscillations in the tank-treading motion but reduce it in the tumbling motion. Dupont *et al.* (2015) improved the FEM+BIM model of Walter *et al.* (2010) into a Shell FEM+BIM one, in which the membrane is assumed as a thin shell followed by the Reissner-Mindlin assumption. They found that the wavelength of membrane wrinkles in simple shear flow was only a function of the membrane thickness. The correlation law coincided with the analytical solution provided by Cerda & Mahadevan (2003).

The shell model is the state of the art to study the membrane buckling effect since the bending resistance regulates the formation of wrinkles or folds. However, the application of shell models to capsule simulations is relatively rare, and the studies in the literature are restricted to the analysis of capsule deformation in simple shear flow. To the best of our knowledge, the effect of shell bending resistance on the dynamics of a capsule suspended in a confined flow field is still an open question.

### 1.2.2 Experimental observations

The pioneering experimental work was performed by (Lee & Fung, 1969), who fabricated the biconcave rubber cells to simulate RBCs and subjected them to a cylindrical tube. Due to technical limitations at the time, both the capsule and channel radius were centimeter-size. With the improvement of fabrication process, the capsule size can reach the millimeter or even micrometer level (depending on the material) in the 1990s, see the methods in Edwards-Lévy *et al.* (1993); Lévy & Edwards-Levy (1996) for example. When microcapsules flow in a Newtonian fluid in a narrow tube where the cross dimension has the same order as the capsule size, the buoyancy and inertial effects can be neglected.

#### • Parachute or Slug shape

The first comprehensive experimental study of artificial capsules flowing in a narrow tube was performed by Risso *et al.* (2006). They prepared almost spherical capsules with a cross-linked human serum albumin (HSA)-alginate membrane and flowed them into a microchannel with an inner diameter of 4mm. The radii of capsules were also millimeter-sized ranging between 1.4 and 1.9 mm. As seen in Fig. 1.3 (a), it shows the shape variations with increasing the flow velocity for a given capsule size. When applying a small flow strength, the capsule deformation is small with two convex ends, while typical parachute-like shapes with curvature inversion in the rear are obtained at large flow strengths. The parachute depth and concave curvatures are also increased with the flow intensity.

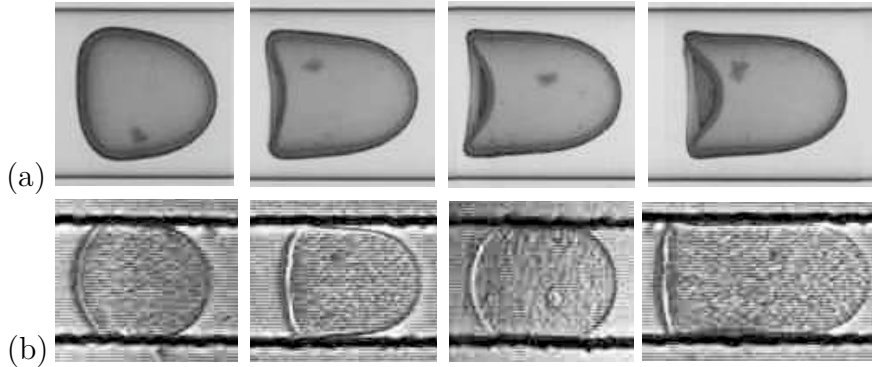


Figure 1.3 – (a) Capsules with a cross-linked HSA-alginate membrane flowing in a cylindrical microchannel with inner diameter 4 mm. Images from Risso *et al.* (2006); (b) Capsules with a cross-linked ovalbumin membrane flowing in a square-section microchannel with inner diameter 75  $\mu\text{m}$ . Images from Lefebvre *et al.* (2008).

Lefebvre *et al.* (2008) flowed a batch of cross-linked ovalbumin capsules with a mean diameter of 67  $\mu\text{m}$  in circular and square-section microchannels with an inner diameter of 75  $\mu\text{m}$ . The parachute shape was observed as well when the capsule flowed through the cylindrical channel. However, in a square-section channel, the capsule was less deformed

than the one in a circular-section channel with the same flow velocity. As seen in Fig. 1.3 (b), the capsules exhibited slug shapes with convexes in the two ends. It reveals a less confinement effect of the square channel for which a higher flow intensity is needed to form the parachute.

### • Wrinkle

The wrinkling phenomenon usually occurs in stretched thin sheets and membranes, resulting from structural instability under compressive stresses. (Nayyar *et al.*, 2011). They may fatigue the capsule membrane, weaken its elasticity and eventually lead to the breakup. Thus, it is important to predict these phenomena for practical applications that require reliable control of membrane wrinkles or ruptures. In this section, we discuss on capsule wrinkles due to dynamic mechanical reasons.

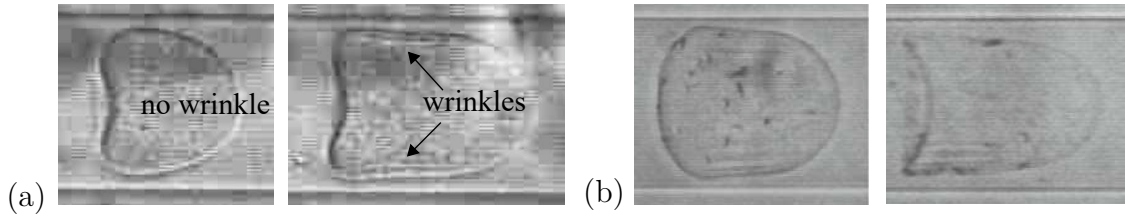


Figure 1.4 – Capsules with a cross-linked ovalbumin membrane flowing in a cylindrical microchannel with inner diameter  $75\ \mu\text{m}$ . Images from (a) Lefebvre *et al.* (2008) and (b) Chu *et al.* (2011).

Lefebvre *et al.* (2008) and Chu *et al.* (2011) have separately observed membrane wrinkles when cross-linked ovalbumin capsules flow through a cylindrical microchannel, as seen in Fig. 1.4. Wrinkles are formed on the contact area where the lubricating layer interacts with the capsule. Combining the experimental results above, the conditions for the formation of wrinkles mainly depend on two factors:

- *Confinement effect.* On the one hand, larger capsules are easier to form wrinkles because they are more squeezed by the channel wall and lubricating layer than small capsules, as seen in Fig. 1.4 (a). On the other hand, capsules in a circular-section channel with a strong confinement effect are easier to form wrinkles than in a square-section channel under the same flow conditions, as seen in Fig. 1.3 (b).
- *Membrane thickness.* A thicker membrane with an enhanced bending rigidity would resist the generation of compressive forces. The membrane of HSA-alginate capsules in the study of Risso *et al.* (2006) is probably too thick to form wrinkles, in which the membrane thickness within a range of  $20\text{--}30\ \mu\text{m}$ . However, the study of measuring the membrane thickness of ovalbumin capsules is not available in the literature, which becomes one part of the investigations in this dissertation.



### 1.3 Determination of capsule membrane mechanical properties

As membrane mechanical properties significantly influence capsules' dynamic response, their characterizations are essential for industrial applications and scientific research. However, the measurement of the membrane properties is challenging due to the smallness and fragility of microcapsules. Different assessment methods have been proposed in the past few decades, and three representative ones have been highlighted in this section: compression between two plates, micropipette aspiration, and microfluidic technique. Those techniques are all based on recording the capsule deformation under controlled stress in the first place. Then mechanical properties can be inferred by employing continuum mechanics models to predict the same deformations as the experimental data.

#### 1.3.1 Compression and micropipette aspiration

Compressing a single millimeter-sized capsule between two parallel plates is a simple method to determine capsule's mechanical properties (Carin *et al.*, 2003; Rachik *et al.*, 2006). As shown in Fig. 1.5, an initially spherical capsule with radius  $r_0$  will be compressed by two parallel plates under a constant velocity. The distance  $d(t)$  between the plates and the resultant force  $F(t)$  on the capsule surface are recorded simultaneously during the experiment. The prediction of the same deformations by a mechanical model is used to estimate the intrinsic mechanical properties.

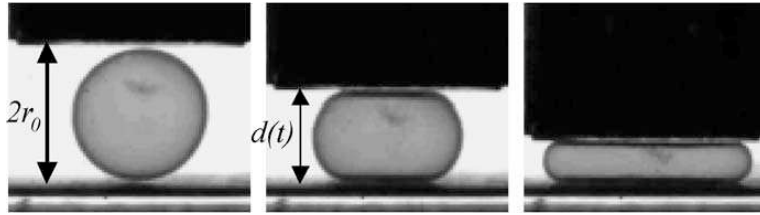


Figure 1.5 – Compression technique for an initially spherical capsule (Rachik *et al.*, 2006).

Carin *et al.* (2003) performed compression experiments with respect to HSA-alginate capsules. Different constitutive models that account for shear and surface dilatation effects are used to analyze the correlation between compression forces and plate separations. The value of area dilatation modulus was found to keep constant with increasing the capsule deformations. Rachik *et al.* (2006) explored the limit of thin shell approximation through a 3D numerical model and compression tests of serum albumin-alginate capsules. They gave a limitation of 5% membrane thickness ratio for which the deformation can satisfy the thin shell approximation. However, a 3D shell model is necessary for the computation of thicker membrane deformations.

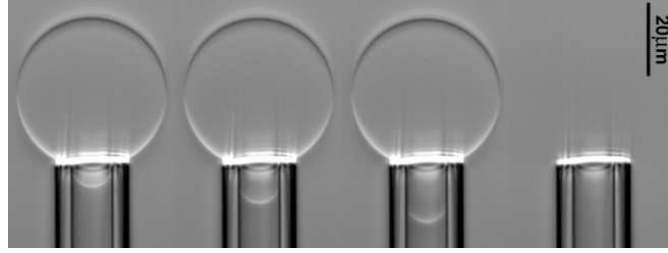


Figure 1.6 – Aspiration of a phospholipid vesicle by a micropipette under a linear pressure (Heinrich & Rawicz, 2005).

Another method is the micropipette aspiration technique that can precisely examine the physical properties of micron-sized biological capsules or cells. Under a linearly increasing pressure, the microcapsule is sucked into a pipette with an inner diameter of several microns until it ruptures at high pressure, as shown in Fig. 1.6. The capsule contours are continuously recorded by microscopy as a function of the applied pressure, and they are subsequently compared with the ones predicted by theoretical/numerical models.

Trickey *et al.* (2006) determined the Poisson's ratio of chondrocytes by combining aspiration experiments with theoretical finite element analyses. They found that chondrocytes are probably compressible according to a measured value of Poisson's ratio varying within 0.36-0.38. Shojaei-Baghini *et al.* (2013) developed an automated micropipette aspiration system using vision-based control and position control for mechanically characterizing single cells. It enabled a higher efficiency and accuracy by this system for measuring cell's elastic and viscoelastic properties.

The compression technique and micropipette aspiration technique can impose the capsule deformation under well control. They also show good accuracy in the measured membrane properties. However, those techniques are difficult to use, requiring expensive equipment and limiting to manipulating an individual capsule once rather than simultaneously characterizing a large group of capsules.

### 1.3.2 Flow in microfluidic channel

Flowing a batch of capsules through a microfluidic channel with a comparable cross-dimension coupled with an inverse analysis technique can efficiently determine the membrane mechanical properties. Fig. 1.7 shows a general process of this technique: the capsule deformed profile extracted from experimental images yields a value of total length and approximate size ratio. Those two indicators help find a combination of size ratio and flow strength from the numerical database to generate the same contour as the experimental one. With knowing the numerical velocity, experimental viscosity and experimental mean flow rate, the surface shear modulus is deduced.

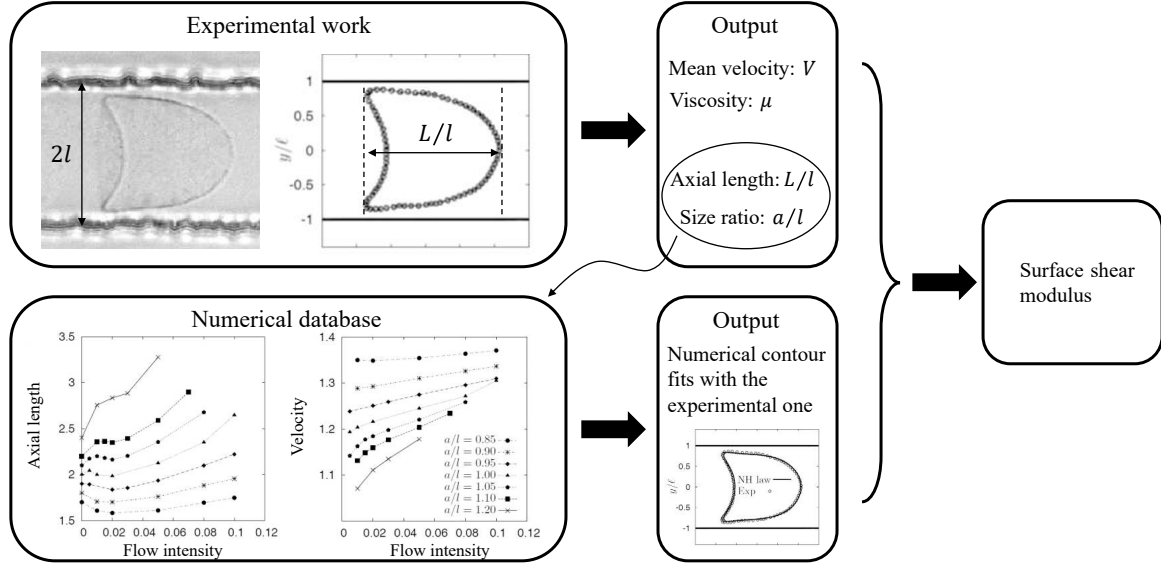


Figure 1.7 – Principle of inverse analysis technique by flowing microcapsules into a microfluidic channel. Figures are taken from Hu *et al.* (2013).

The inverse analysis technique was initially proposed by Lefebvre *et al.* (2008), who used an axisymmetric model to analyze the experimental data, in which ovalbumin capsules with a mean diameter of  $67 \mu\text{m}$  flowed through circular and square-section microchannels with an inner diameter of  $75 \mu\text{m}$ . They found that the technique generated an almost constant value of membrane shear modulus for different capsule sizes and deformation when assuming a Neo-Hookean constitutive law. Chu *et al.* (2011) used the same approach to determine the membrane shear modulus of ovalbumin capsules fabricated at different reaction pH and reticulation time. The chart including the mean value of shear modulus varying with pH and time can help discriminate the various cross-linking degrees of microcapsules. By using the inverse analysis technique based on a full 3D numerical model, Hu *et al.* (2013) reconfirmed the conclusion that ovalbumin membranes tend to have a strain-softening behavior, i.e., obeys Neo-Hookean law. The measured value of membrane shear modulus in this study complied with the one measured by Chu *et al.* (2011) based on an axisymmetric model.

Most of the analytical/numerical models used in the above various techniques for measuring membrane mechanical property are based on the hypothesis that the membrane is an infinitely thin surface devoid of thickness and bending resistance. Admittedly, the bending forces are very small compared with the membrane forces when the thickness ratios less than 10% (Hu *et al.*, 2012). Thus it is certain that those measurements are qualitatively correct. However, if one wants to determine the thickness and bending modulus of capsule membrane, a thin shell model and new techniques are requisite.

## 1.4 Objectives

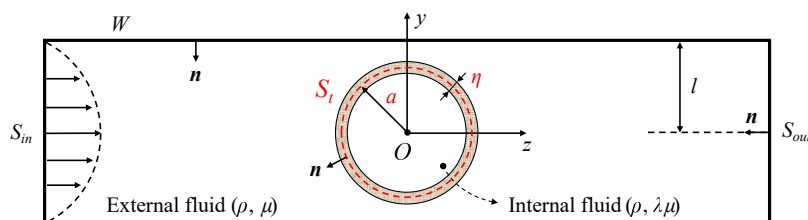
The mechanical behavior of a capsule flowing in a confined flow field is a complicated fluid-structure interaction problem, including viscous flows, channel confinements, and shell deformations. It is known that the flow conditions and membrane mechanical properties determine capsule dynamic responses, while some aspects are still not fully studied yet. The first one is related to membrane wrinkling due to channel confinements, which has been experimentally observed when a capsule flowing in a tightly confined channel (Fig. 1.4). In the meantime, the capsule reaches a steady parachute shape that exhibits drastic curvature changes (in value and sign) from the capsule tip to its rear. Thus the second question is related to the relationship between membrane bending energy and curvature. Since the above capsule buckling behaviors may weaken the capsule wall, the membrane could break up, and the internal fluid liberates before reaching the desirable place. Consequently, the final question is the determination of membrane mechanical properties.

In order to answer the three open questions, we investigate the dynamic behavior of an initially spherical capsule flowing through a microchannel with the following objectives:

- *Effect of bending resistance and channel confinement effects on capsule deformation.*
- *The relationship between membrane bending energy with respect to the curvature.*
- *Determination of membrane mechanical properties: membrane thickness, bending modulus, shear modulus.*

Based on the numerical model developed by Dupont *et al.* (2015), who couple a Boundary Integral Method for internal and external flows with a Shell Finite Element Method for shell deformation, we adapt it to a confined flow case for the first time to take into account the channel confinements. The problem description and the new numerical model are presented in Chapter 2. Chapter 3 and Chapter 4 investigate the influence of the bending resistance on the dynamics of an initially spherical capsule in an unbounded parabolic flow and a bounded Poiseuille flow, respectively, including the membrane bending energy-curvature relationship and the relationship between wrinkle wavelength and wall thickness. For the purpose of determining membrane mechanical properties for a population of artificial capsules, the membrane thickness is characterized by indirect inverse analyses in Chapter 4, and the surface shear modulus is characterized by an automatic microfluidic method in Chapter 5. The effects of different membrane constitutive laws on capsule rheological behaviors are also discussed in this chapter. Conclusions and perspectives are made in Chapter 6 in the end.

## 2.1 Problem description



As shown in Fig. 2.1, we consider the situation where an initially spherical capsule, which consists of an internal droplet with volume  $V_{vol}$  and a hyperelastic shell, is subjected to an external confined flow field. Since the membrane is assumed to be impermeable, the mass and volume do not change over time. The capsule initial radius  $a$  is thus defined as the radius of the sphere with the same volume of the droplet

$$a = \left( \frac{3V_{vol}}{4\pi} \right)^{\frac{1}{3}}. \quad (2.1)$$

The capsule membrane is considered as a three-dimensional incompressible homogeneous shell, described by a mid-surface  $S_t$  and wall thickness  $\eta$ . The shell can be characterized by a bulk shear modulus  $G$  and a bending modulus  $M_b$ , linked by

$$M_b = \frac{G\eta^3}{6(1-\nu)}, \quad (2.2)$$

where  $\nu$  is Poisson ratio. If the shell is simplified as a two-dimensional elastic surface  $S_t$  without accounting for thickness,  $S_t$  is characterized by a surface shear modulus  $G_s = G\eta$ , and the material bending resistance is neglected in this case.

The capsule is assumed to flow along the centerline of a long straight channel with a constant circular cross-section. The characteristic hydraulic radius of the channel is  $l$ . By neglecting the inertia forces and buoyancy effects, the capsule will keep in the center of the channel during deformation (Quéguiner & Barthès-Biesel, 1997; Doddi & Bagchi, 2008). The internal and external liquids are both incompressible and Newtonian with the same density  $\rho$ , and viscosity  $\lambda\mu$  and  $\mu$  respectively. Diaz & Barthès-Biesel (2001) have demonstrated that the viscosity ratio  $\lambda$  does not affect the steady-state capsule shape when the capsule is flowing in a straight channel. As this dissertation mainly investigates the capsule deformation at steady-state, thus  $\lambda = 1$  is taken without losing generality.

Several non-dimensional parameters govern this capsule flow problem:

- **size ratio (or confinement ratio)  $a/l$ .**

It determines the relative size of the capsule to the cross-dimension of the channel.

- **wall thickness ratio  $\alpha$ .**

$$\alpha = \frac{\eta}{a}. \quad (2.3)$$

It represents the bending rigidity of the shell. Another representation of bending resistance is the bending number  $K_b$ , which compares the bending forces to the shear elastic forces

$$K_b = \frac{M_b}{G\eta a^2} = \frac{M_b}{G_s a^2}. \quad (2.4)$$

For an incompressible homogeneous material with Poisson ratio  $\nu = 0.5$ ,  $K_b = \alpha^2/3$  simplified from Eq. (2.2).

- **bulk capillary number  $Ca_v$ .**

$$Ca_v = \frac{\mu V}{Ga}. \quad (2.5)$$

which compares the viscous forces exerted by the fluid to the elastic forces of the deformed shell.  $V$  represents the flow characteristic velocity.

- surface capillary number  $Ca_s$ .

$$Ca_s = \frac{\mu V}{G_s} = \frac{Ca_v}{\alpha}. \quad (2.6)$$

which compares the viscous forces exerted by the fluid to the surface elastic forces of the mid-surface. In this dissertation, the subscript "s" is used to denote quantities associated with the mid-surface.

## 2.2 Fluid problem

### 2.2.1 Internal and external flows

We assume the suspending flow inside the cylindrical channel is a fully developed Poiseuille flow with mean velocity  $V$  and flow rate  $Q$ . Because of a very small particle Reynolds number  $Re = \rho V l / \mu \ll 1$ , the motions of internal and external liquids satisfy the Stokes equations

$$\nabla \cdot \underline{v}^{(\beta)} = 0, \quad \nabla \cdot \underline{\sigma}^{(\beta)} = \underline{0}, \quad \beta = 1, 2. \quad (2.7)$$

where  $\underline{v}^{(\beta)}$  and  $\underline{\sigma}^{(\beta)}$  represent the velocity and stress fields of the fluids ( $\beta = 1$  for suspending and  $\beta = 2$  for internal), which are solved in a domain bounded by the entrance  $S_{in}$ , the exit  $S_{out}$ , the channel wall  $W$  and the mid-surface  $S_t$ . The channel is long enough so that the entrance and exit effects due to capsule disturbance are neglected. The boundary conditions of the problem are:

- (1) No flow disturbance on  $S_{in}$  and  $S_{out}$ :

$$\underline{v}^{(1)}(\underline{x}, t) \rightarrow \underline{v}^\infty(\underline{x}), \quad \underline{x} \in S_{in} \cup S_{out}, \quad (2.8)$$

- (2) Pressure on  $S_{in}$  and  $S_{out}$ :

$$p^{(1)}(\underline{x}, t) = 0, \quad \underline{x} \in S_{in}; \quad p^{(1)}(\underline{x}, t) = \Delta P(t) + \Delta P^\infty, \quad \underline{x} \in S_{out}, \quad (2.9)$$

where  $p$  denotes the pressure field,  $\Delta P^\infty$  is the undisturbed pressure drop between  $S_{in}$  and  $S_{out}$  in the absence of capsule and  $\Delta P$  is the disturbance pressure drop due to capsule presence.

- (3) No slip on channel wall  $W$ :

$$\underline{v}^{(1)}(\underline{x}, t) = \underline{0}, \quad \underline{x} \in W, \quad (2.10)$$

(4) No slip on the mid-surface  $S_t$ :

$$\underline{v}^{(1)}(\underline{x}_s, t) = \underline{v}^{(2)}(\underline{x}_s, t) = \frac{\partial}{\partial t} \underline{x}_s(\underline{X}_s, t), \quad \underline{x}_s \in S_t, \quad (2.11)$$

where  $\underline{X}_s$  represents the position of a mid-surface point in the reference state located at position  $\underline{x}_s$  at time  $t$ .

(5) The external load  $\underline{q}_s$  (force per unit area) on the mid-surface equals to the viscous traction jump across the interface:

$$(\underline{\sigma}^{(1)} - \underline{\sigma}^{(2)}) \cdot \underline{n} = \underline{q}_s, \quad \underline{x}_s \in S_t, \quad (2.12)$$

where  $\underline{n}$  is the unit normal vector of boundaries, and it points inwards to the suspending fluid, as indicated in Fig. 2.1.

### 2.2.2 Boundary integral formulation

In the Stokes flow regime and the assumption of  $\lambda = 1$ , Pozrikidis (2005) gave the expression of the velocity of any point  $\underline{x}$  in the channel fluid domain shown in Fig. 2.1 by a boundary integral form, relating to the tractions on the membrane, the disturbance wall friction, and the disturbance pressure difference.

$$\underline{v}(\underline{x}) = \underline{v}^\infty(\underline{x}) - \frac{1}{8\pi\mu} \left[ \int_{S_t} \underline{J}(\underline{r}) \cdot \underline{q}_s dS(\underline{y}) + \int_W \underline{J}(\underline{r}) \cdot \underline{f} dS(\underline{y}) - \Delta P \int_{S_{out}} \underline{J}(\underline{r}) \cdot \underline{n} dS(\underline{y}) \right]. \quad (2.13)$$

It indicates that the confined capsule flow consists of two parts: the undisturbed flow in the absence of capsule ( $\underline{v}^\infty$ ), and the disturbing flow due to capsule presence (integral terms). In the laboratory reference frame  $\mathcal{F}(O, \underline{e}_x, \underline{e}_y, \underline{e}_z)$  with  $O$  the capsule center of mass,  $\underline{v}^\infty$  has the parabolic profile of the Poiseuille flow

$$\underline{v}^\infty = 2V \left[ 1 - (x^2 + y^2)/l^2 \right] \underline{e}_z. \quad (2.14)$$

The Green kernel  $\underline{J}$  is defined by

$$\underline{J}(\underline{r}) = \frac{1}{r} \mathbb{I} + \frac{\underline{r} \otimes \underline{r}}{r^3} \quad (2.15)$$

with  $\underline{r} = \underline{x} - \underline{y}$  and  $r = \|\underline{r}\|$ .  $\mathbb{I}$  is the identity tensor.

$\underline{f}$  is the disturbance wall friction due to capsule presence. To derive the expression for  $\underline{f}$ , the reciprocal theorem is first applied to the flow without capsule ( $\underline{v}^\infty, \underline{\sigma}^\infty$ ) and to the





In the laboratory reference frame  $\mathcal{F}(O, \underline{e}_x, \underline{e}_y, \underline{e}_z)$ , the capsule membrane is considered as a thin shell defined by the mid-surface  $S_t$  and wall thickness  $\eta$ . We introduce the curvilinear coordinates  $(\xi^1, \xi^2, \xi^3)$  in the 3D mathematical space  $\mathbb{R}^3$  to describe the shell. The one-to-one mapping from a domain of  $\mathbb{R}^3$  into  $\mathcal{F}$  is called a 3D chart  $\underline{\Phi}$ . Correspondingly, the mid-surface of a given shell is defined by a collection of 2D charts  $\underline{\phi}$ , i.e., the mappings from domains of  $\mathbb{R}^2$  with coordinates  $(\xi^1, \xi^2)$  into  $\mathcal{F}$  (Chapelle & Bathe, 2010). Therefore, all quantities of interest can be evaluated on the mid-surface with convenience.

As seen in Fig. 2.2, the position of any point  $M$  in the reference configuration in the mid-surface could be uniquely defined by a 2D chart  $\underline{\phi}(\xi^1, \xi^2)$  in the reference configuration, such that

$$\underline{OM} = \underline{X}_s = \underline{\phi}(\xi^1, \xi^2). \quad (2.20)$$

The local covariant base  $(\underline{A}_1, \underline{A}_2, \underline{A}_3)$ , in which the first two vectors are tangent to the coordinate curves passing through  $M$ , and the third is the unit normal vector orthogonal to the first two, is defined as

$$\underline{A}_\alpha = \frac{d\underline{\phi}(\xi^1, \xi^2)}{d\xi^\alpha} = \underline{\phi}_{,\alpha} \quad \text{and} \quad \underline{A}_3 = \frac{\underline{A}_1 \times \underline{A}_2}{\|\underline{A}_1 \times \underline{A}_2\|}. \quad (2.21)$$

The contravariant base  $(\underline{A}^1, \underline{A}^2, \underline{A}^3)$  is deduced from the relations

$$\underline{A}^\alpha \cdot \underline{A}_\beta = \delta^\alpha_\beta \quad \text{and} \quad \underline{A}^3 = \underline{A}_3, \quad (2.22)$$

where  $\delta$  denotes the Kronecker symbol, which is 1 at  $\alpha = \beta$  and 0 otherwise.

In the reference configuration, the 3D position of mid-surface point  $M$  in the medium of the shell is defined by

$$\underline{X} = \underline{\Phi}(\xi^1, \xi^2, \xi^3) = \underline{\phi}(\xi^1, \xi^2) + \xi^3 \underline{A}_3 \quad (2.23)$$

with  $|\xi^3| < \eta(\xi^1, \xi^2)/2$ .  $\eta(\xi^1, \xi^2)$  represents the thickness of the shell at position  $(\xi^1, \xi^2)$ . Then the 3D covariant base  $(\underline{G}_1, \underline{G}_2, \underline{G}_3)$  has the form

$$\underline{G}_\alpha = \underline{X}_{,\alpha} = \underline{A}_\alpha + \xi^3 \underline{A}_{3,\alpha} \quad \text{and} \quad \underline{G}_3 = \underline{A}_3. \quad (2.24)$$

The contravariant base  $(\underline{G}^1, \underline{G}^2, \underline{G}^3)$  is deduced from the same relation as Eq. (2.22).

Hereafter, capital letters are used to denote vectors in the reference configuration, such as  $(\underline{A}_1, \underline{A}_2, \underline{A}_3)$  and  $(\underline{G}_1, \underline{G}_2, \underline{G}_3)$ . The corresponding ones in the deformed configuration are denoted by lowercase letters, such as  $(\underline{a}_1, \underline{a}_2, \underline{a}_3)$  and  $(\underline{g}_1, \underline{g}_2, \underline{g}_3)$ . Besides, the components of vectors and surface tensors have Greek indices varying in  $\{1, 2\}$ , and Latin indices varying in  $\{1, 2, 3\}$  denote the components of 3D tensors that appear in the sequel.

### 2.3.2 Differential geometry on mid-surface and shell

The covariant and contravariant bases are first-order surface tensors, i.e., vectors. An important symmetric second-order tensor in the tangent plane for measuring the length in the mid-surface is the surface metric tensor  $\underline{\underline{a}}$ , also called the *first fundamental form* of the surface, defined in the deformed configuration with a covariant form by

$$\underline{\underline{a}} = a_{\alpha\beta} \underline{a}^\alpha \otimes \underline{a}^\beta \quad (2.25)$$

with

$$a_{\alpha\beta} = \underline{a}_\alpha \cdot \underline{a}_\beta. \quad (2.26)$$

The contravariant form is written as  $\underline{\underline{a}} = a^{\alpha\beta} \underline{a}_\alpha \otimes \underline{a}_\beta$  with  $a^{\alpha\beta} = \underline{a}^\alpha \cdot \underline{a}^\beta$ .

Another important second-order tensor is the curvature tensor  $\underline{\underline{\kappa}}$ , also called the *second fundamental form* of the surface, which contains all the information on the surface curvature, defined by

$$\underline{\underline{\kappa}} = \kappa_{\alpha\beta} \underline{a}^\alpha \otimes \underline{a}^\beta \quad (2.27)$$

with

$$\kappa_{\alpha\beta} = \frac{1}{2} (\underline{a}_\alpha \cdot \underline{a}_{3,\beta} + \underline{a}_\beta \cdot \underline{a}_{3,\alpha}). \quad (2.28)$$

The mean and Gaussian curvatures of the surface can be deduced by

$$K_M = \frac{1}{2} (K_1 + K_2) = \frac{1}{2} (\kappa_1^1 + \kappa_2^2) = \frac{1}{2} \text{tr } \underline{\underline{\kappa}} \quad (2.29)$$

$$K_G = K_1 K_2 = \kappa_1^1 \kappa_2^2 - \kappa_2^1 \kappa_1^2 = \det \underline{\underline{\kappa}} \quad (2.30)$$

with

$$\kappa_\beta^\alpha = a^{\alpha\lambda} \kappa_{\lambda\beta}, \quad (2.31)$$

where  $K_1$  and  $K_2$  are principal curvatures, and the Einstein summation convention is adopted on repeated indices.

We introduce the bending deformation tensor  $\underline{\underline{\psi}}$ , which is a surface tensor given by the increment of the curvature tensor and defined in the reference state, expressed as

$$\underline{\underline{\psi}} = \psi_{\alpha\beta} \underline{A}^\alpha \otimes \underline{A}^\beta \quad (2.32)$$

with

$$\psi_{\alpha\beta} = \kappa_{\alpha\beta} - K_{\alpha\beta} = \frac{1}{2} [(\underline{a}_\alpha \cdot \underline{a}_{3,\beta} + \underline{a}_\beta \cdot \underline{a}_{3,\alpha}) - (\underline{A}_\alpha \cdot \underline{A}_{3,\beta} + \underline{A}_\beta \cdot \underline{A}_{3,\alpha})]. \quad (2.33)$$

The mean and Gaussian values of bending deformation can be deduced by

$$\Psi_M = \frac{1}{2}(\Psi_1 + \Psi_2) = \frac{1}{2}(\psi_1^1 + \psi_2^2) = \frac{1}{2}\text{tr } \underline{\underline{\psi}} \quad (2.34)$$

$$\Psi_G = \Psi_1\Psi_2 = \psi_1^1\psi_2^2 - \psi_2^1\psi_1^2 = \det \underline{\underline{\psi}} \quad (2.35)$$

with

$$\psi_\beta^\alpha = A^{\alpha\lambda}\psi_{\lambda\beta}, \quad (2.36)$$

where  $\Psi_1$  and  $\Psi_2$  are principal bending deformations.

In the medium of the shell, the distance between any two points is measured by the 3D (or volume) metric tensor

$$\underline{\underline{g}} = g_{ij} \underline{g}^i \otimes \underline{g}^j \quad (2.37)$$

with

$$\begin{cases} g_{\alpha\beta} = \underline{g}_\alpha \cdot \underline{g}_\beta \\ g_{\alpha 3} = \underline{g}_\alpha \cdot \underline{g}_3 = 0 \\ g_{33} = \underline{g}_3 \cdot \underline{g}_3 = 1. \end{cases} \quad (2.38)$$

The contravariant form can be easily inferred as  $g^{\alpha\beta} = \underline{g}^\alpha \cdot \underline{g}^\beta$ ,  $g^{\alpha 3} = 0$ ,  $g^{33} = 1$ .

### 2.3.3 Shell kinematics

For a given material point in the shell, the new position  $\underline{x}$  and the original position  $\underline{X}$  is linked by the displacement  $\underline{u}$  through

$$\underline{x}(\underline{X}, t) = \underline{X} + \underline{u}(\underline{X}, t), \quad (2.39)$$

where the vector  $\underline{u}$  represents the displacement between the reference and deformed configurations. We assume a material line across the shell that is initially orthogonal to the mid-surface at the coordinates  $(\xi^1, \xi^2)$  will remain straight and unstretched during the deformations. The displacement  $\underline{u}$  of points located on this line can be expressed by

$$\underline{u}(\xi^1, \xi^2, \xi^3, t) = \underline{u}_s(\xi^1, \xi^2, t) + \xi^3 \theta_\lambda(\xi^1, \xi^2, t) \underline{a}^\lambda(\xi^1, \xi^2). \quad (2.40)$$

The displacement  $\underline{u}_s$  represents the mid-surface displacement at coordinates  $(\xi^1, \xi^2)$ . The displacement  $\xi^3 \theta_\lambda \underline{a}^\lambda$  is linked with the rotation angles  $\theta_1$  and  $\theta_2$  around an axis defined by vectors  $\underline{a}^2$  and  $\underline{a}^1$ . The rotation of the material line leads to the fact that the line initially orthogonal to the mid-surface is no longer orthogonal in the deformed configuration, known as the *Reissner-Mindlin kinematical assumption* (Chapelle & Bathe, 2010). It also can be seen that a vector normal to that line, expressed by  $\underline{\theta} = \theta_\lambda \underline{a}^\lambda$ , can uniquely define

the rotations without a component on  $\underline{a}^3$ . Thus Eq. (2.40) is written as

$$\underline{u}(\xi^1, \xi^2, \xi^3, t) = \underline{u}_s(\xi^1, \xi^2, t) + \xi^3 \underline{\theta}(\xi^1, \xi^2, t), \quad (2.41)$$

where the mid-surface displacement  $\underline{u}_s$  is deduced by integrating velocity over time through Eq. (2.11). The vector  $\underline{\theta}$  is unknown and must be determined (in section 2.4.2).

The gradient of the transformation  $\underline{\underline{F}}$  maps the 3D position in the reference state to the deformed state by

$$d\underline{x} = \underline{\underline{F}} \cdot d\underline{X}. \quad (2.42)$$

Considering  $d\underline{x} = \underline{g}_\alpha \xi^\alpha$  and  $d\underline{X} = \underline{G}_\alpha \xi^\alpha$ ,  $\underline{\underline{F}}$  can be written as

$$\underline{\underline{F}} = \underline{g}_\alpha \otimes \underline{G}^\alpha. \quad (2.43)$$

In the curvilinear coordinates, the Green-Lagrange strain tensor defined in the reference state is given by half of the increment of the 3D metric tensor, expressed as

$$\begin{aligned} \underline{\underline{e}} &= \frac{1}{2} (\underline{\underline{F}}^T \cdot \underline{\underline{F}} - \mathbb{I}) \\ &= e_{ij} \underline{G}^i \otimes \underline{G}^j \end{aligned} \quad (2.44)$$

with

$$\begin{aligned} e_{ij} &= \frac{1}{2} (g_{ij} - G_{ij}) \\ &= \frac{1}{2} (\underline{u}_{,i} \cdot \underline{G}_j + \underline{u}_{,j} \cdot \underline{G}_i + \underline{u}_{,i} \cdot \underline{u}_{,j}) \end{aligned} \quad (2.45)$$

Substituting (2.24) and (2.41) into (2.45), truncating the in-plane strain  $e_{\alpha\beta}$  to lowest-order terms for  $\xi^3$ , and neglecting the transverse term with  $\xi^3$  in the shear strain  $e_{\alpha 3}$ , the non-linear Green-Lagrange strain tensor can be rewritten as

$$\begin{cases} e_{\alpha\beta} = \gamma_{\alpha\beta}(\underline{u}_s) + \xi^3 \chi_{\alpha\beta}(\underline{u}_s, \underline{\theta}), \\ e_{\alpha 3} = \zeta_\alpha(\underline{u}_s, \underline{\theta}), \\ e_{33} = 0, \end{cases} \quad (2.46)$$

where

$$\begin{cases} \gamma_{\alpha\beta} = \frac{1}{2} [\underline{A}_\alpha \cdot \underline{u}_{s,\beta} + \underline{A}_\beta \cdot \underline{u}_{s,\alpha} + \underline{u}_{s,\alpha} \cdot \underline{u}_{s,\beta}], \\ \chi_{\alpha\beta} = \frac{1}{2} [\underline{A}_\alpha \cdot \underline{\theta}_{,\beta} + \underline{A}_{3,\alpha} \cdot \underline{u}_{s,\beta} + \underline{A}_\beta \cdot \underline{\theta}_{,\alpha} + \underline{A}_{3,\beta} \cdot \underline{u}_{s,\alpha} + \underline{u}_{s,\beta} \cdot \underline{\theta}_{,\alpha} + \underline{u}_{s,\alpha} \cdot \underline{\theta}_{,\beta}], \\ \zeta_\alpha = \frac{1}{2} [\underline{A}_\alpha \cdot \underline{\theta} + \underline{A}_3 \cdot \underline{u}_{s,\alpha} + \underline{\theta} \cdot \underline{u}_{s,\alpha}]. \end{cases} \quad (2.47)$$

In the framework of the Reissner-Mindlin assumption, the transverse strain  $e_{33} = 0$  is inferred due to the assumption of straight and unstretched material line. The tensors  $\underline{\underline{\gamma}}$ ,  $\underline{\underline{\chi}}$  and  $\underline{\underline{\zeta}}$  are called as the membrane strain, bending strain, and shear strain tensors.

### 2.3.4 Constitutive law

The in-plane deformation can be measured by a rotation-independent symmetric tensor, the right Cauchy-Green deformation tensor  $\underline{\underline{C}}_s$ , which is defined in the reference state by,

$$\underline{\underline{C}}_s = \underline{\underline{F}}_s^T \cdot \underline{\underline{F}}_s = a_{\alpha\beta} \underline{\underline{A}}^\alpha \otimes \underline{\underline{A}}^\beta, \quad (2.48)$$

where  $\underline{\underline{F}}_s$  represents the 2D transformation gradient that links the mid-surface position between the reference and the deformed states, defined by  $\underline{\underline{F}}_s = \partial \underline{\underline{x}}_s / \partial \underline{\underline{X}}_s$ . The two square roots of eigenvalues of  $\underline{\underline{C}}_s$  are called principal dilatation ratios  $\lambda_{s1}$  and  $\lambda_{s2}$ . The two invariants of the transformation  $I_{s1}$  and  $I_{s2}$  can be defined as follows

$$\begin{aligned} I_{s1} &= \text{tr} \underline{\underline{C}}_s - 2 = \lambda_{s1}^2 + \lambda_{s2}^2 - 2, \\ I_{s2} &= \det \underline{\underline{C}}_s - 1 = \lambda_{s1}^2 \lambda_{s2}^2 - 1. \end{aligned} \quad (2.49)$$

When the mid-surface is isotropic, the 2D second Piola-Kirchhoff tension tensor  $\underline{\underline{\Sigma}}_s$  (force per unit arclength in the reference state) is derived from a strain energy function  $w_s$  (energy per unit undeformed surface area):

$$\underline{\underline{\Sigma}}_s = \frac{\partial w_s}{\partial \underline{\underline{e}}_s}, \quad (2.50)$$

where  $\underline{\underline{e}}_s$  represents the 2D Green-Lagrange strain tensor defined by  $\underline{\underline{e}}_s = \frac{1}{2}(\underline{\underline{F}}_s^T \cdot \underline{\underline{F}}_s - \mathbb{I})$ .

#### • Generalized Hooke's law

The Generalized Hooke's law provides a linear dependence of the tension on the strain, which reads

$$\underline{\underline{\Sigma}}_s = \underline{\underline{\underline{\underline{H}}}}_s : \underline{\underline{e}}_s. \quad (2.51)$$

where  $\underline{\underline{\underline{\underline{H}}}}_s$  denotes the fourth-order 2D elasticity tensor that does not depend on  $\underline{\underline{e}}_s$ . Thus, the strain energy  $w_s = \frac{1}{2} \underline{\underline{\underline{\underline{H}}}}_s : \underline{\underline{e}}_s^2$  is a quadratic function of the strain depending only on the invariants of  $\underline{\underline{e}}_s$ . For a two-dimensional material, the GH law is given by

$$w_s^{\text{GH}} = \frac{G_s}{4} \left( 2I_{s1} - 2I_{s2} + \frac{1}{1 - \nu_s} I_{s1}^2 \right) \quad (2.52)$$

where  $\nu_s \in ] -1, 1[$  is a surface Poisson ratio. The area dilatation modulus is then  $K_s =$

$G_s \frac{1 + \nu_s}{1 - \nu_s}$ , which implies that  $\nu_s \rightarrow 1$  corresponds to an area incompressible membrane.

- **Neo-Hookean law**

A classical three-dimensional law, Neo-Hookean (NH) law, describes volume-incompressible rubber-like materials. The two-dimensional form is given by (Lac *et al.*, 2004)

$$w_s^{\text{NH}} = \frac{G_s}{2} \left( I_{s1} - 1 + \frac{1}{I_{s2} + 1} \right). \quad (2.53)$$

Because of the hypothesis of volume incompressibility, area dilation is balanced by membrane thinning so that  $K_s = 3G_s$

- **Skalak law**

For describing anisotropic biological bi-layers (such as the RBC membrane), Skalak *et al.* (1973) proposed a law (SK) with independent surface shear and area dilation modulus

$$w_s^{\text{SK}} = \frac{G_s}{4} \left[ (I_{s1}^2 + 2I_{s1} - 2I_{s2}) + CI_{s2}^2 \right]. \quad (2.54)$$

The area dilatation modulus is  $K_s = (1 + 2C)G_s$ , in which the dimensionless parameter  $C$  regulates the resistance to area dilatation.

For  $\nu_s = 0.5$  and  $C = 1$ , corresponding to  $K_s = 3G_s$ , the three laws GH, NH, SK have the same small-deformation behavior, but predict different material responses for large strains (Barthès-Biesel *et al.*, 2002; Lac *et al.*, 2004): under a uniaxial stretching, the GH law and SK law are strain-hardening, whereas the NH law is strain-softening.

### 2.3.5 Shell equilibrium

The balance of the shell between viscous forces and elastic forces is governed by a classical equilibrium equation, written in a strong form by

$$\underline{\nabla} \cdot \underline{T} + \underline{q} = \underline{0}, \quad (2.55)$$

where  $\underline{\nabla}$  is the divergence operator in the deformed state,  $\underline{q}$  is the 3D external load (force per unit volume) exerted by the fluids on the shell, and  $\underline{T}$  is the 3D Cauchy stress tensor (force per unit area). Let  $\mathcal{V}$  be the Sobolev space  $H^1(S_t, \mathbb{R}^3)$ . The variational formulation (weak form) of Eq. (2.55) based on the principle of virtual work is written as

$$\forall \hat{\underline{u}} \in \mathcal{V}, \quad \int_V \hat{\underline{u}} \cdot \underline{q} dV = \int_V \hat{\underline{\varepsilon}}(\hat{\underline{u}}) : \underline{T} dV, \quad (2.56)$$

where  $\hat{\underline{\underline{\epsilon}}}(\hat{\underline{u}}) = \frac{1}{2}(\nabla \hat{\underline{u}} + \nabla \hat{\underline{u}}^T)$  denotes the virtual strain tensor.  $V$  represents the shell volume in the deformed state.  $\hat{\underline{u}}$  denotes an arbitrary 3D virtual displacement that satisfies the Reissner-Mindlin assumption, written by

$$\hat{\underline{u}}(\xi^1, \xi^2, t) = \hat{\underline{u}}_s(\xi^1, \xi^2, t) + \xi^3 \hat{\underline{\theta}}(\xi^1, \xi^2, t) \quad (2.57)$$

with  $|\xi^3| = \eta(\xi^1, \xi^2)/2$ . The tensors  $\hat{\underline{u}}_s$  and  $\hat{\underline{\theta}}$  represent the virtual displacement and virtual rotation defined on the mid-surface.

Since the deformation is usually measured according to the reference configuration, the shell elastic stress can be quantified by the 3D second Piola-Kirchhoff stress tensor  $\underline{\underline{\Sigma}}$  corresponding to force per unit area of undeformed material. It associates with the Cauchy stress tensor  $\underline{T}$  by

$$\underline{\underline{\Sigma}} = J \underline{F}^{-1} \cdot \underline{T} \cdot \underline{F}^T, \quad (2.58)$$

where  $J = \det \underline{F}$  is the Jacobian. Therefore, the form defined in the reference configuration of Eq. (2.56) is written as

$$\forall \hat{\underline{u}} \in \mathcal{V}, \quad \int_V \hat{\underline{u}} \cdot \underline{q} dV = \int_{V_0} \hat{\underline{\epsilon}}(\hat{\underline{u}}) : \underline{\underline{\Sigma}} dV, \quad (2.59)$$

or

$$\forall \hat{\underline{u}}_s, \hat{\underline{\theta}} \in \mathcal{V}, \quad \int_{S_t} \hat{\underline{u}}_s \cdot \underline{q}_s dS = \int_{V_0} \hat{\underline{\epsilon}}(\hat{\underline{u}}_s, \hat{\underline{\theta}}) : \underline{\underline{\Sigma}} dV \quad (2.60)$$

by assuming the loading is constant through the thickness, i.e.,  $\underline{q}_s = \underline{q}\eta$ .  $V_0$  is the shell volume in the initial state.

### 2.3.6 Shell mathematical model

A linear relationship between the Green-Lagrange strain tensor  $\underline{\underline{e}}$  and the second Piola-Kirchhoff stress tensor  $\underline{\underline{\Sigma}}$  follows the generalized Hooke's law. Assuming plane stress  $\Sigma^{33} = 0$ , Eq. (2.60) becomes

$$\forall \hat{\underline{u}}_s, \hat{\underline{\theta}} \in \mathcal{V}, \quad \int_{S_t} \hat{\underline{u}}_s \cdot \underline{q}_s dS = \int_{V_0} \left( C^{\alpha\beta\lambda\mu} e_{\alpha\beta} \hat{e}_{\lambda\mu} + D^{\alpha\lambda} e_{\alpha 3} \hat{e}_{\lambda 3} \right) dV. \quad (2.61)$$

with

$$\begin{aligned} C^{\alpha\beta\lambda\mu} &= G \left( A^{\alpha\lambda} A^{\beta\mu} + A^{\alpha\mu} A^{\beta\lambda} + \frac{2\nu}{1-\nu} A^{\alpha\beta} A^{\lambda\mu} \right), \\ D^{\alpha\lambda} &= 4G A^{\alpha\lambda}. \end{aligned} \quad (2.62)$$

The assumption  $\Sigma^{33} = 0$  implying  $e_{33} \neq 0$  apparently contradicts the Reissner-Mindlin assumption ( $e_{33} = 0$ ). Since  $e_{33}$  does not occur in (2.61), this problem thus has no actual



impact. The variational formulation (2.61) is called the *basic shell model*. See the book Chapelle & Bathe (2010) for the detailed derivation process.

For the sake of governing the deformation of the shell mid-plane by following different constitutive laws, a *shear-membrane-bending shell model* (abbreviated SMB) is further introduced to separately evaluate the work done by the shear, membrane, and bending effects. Substituting  $\gamma_{\alpha\beta} + \xi^3 \chi_{\alpha\beta}$  for  $e_{\alpha\beta}$  and specializing the integration over the mid-surface  $S_t$ , the weak form (2.61) becomes

$$\begin{aligned} \forall \underline{\hat{u}}_s, \underline{\hat{\theta}} \in \mathcal{V}, \quad \int_{S_t} \underline{\hat{u}}_s \cdot \underline{\hat{q}}_s dS &= \int_{S_0} C^{\alpha\beta\lambda\mu} \left( \eta \gamma_{\alpha\beta} \hat{\gamma}_{\lambda\mu} + \frac{\eta^3}{12} \chi_{\alpha\beta} \hat{\chi}_{\lambda\mu} \right) dS \\ &+ \int_{S_0} \eta D^{\alpha\lambda} \zeta_\alpha \hat{\zeta}_\alpha dS \end{aligned} \quad (2.63)$$

where  $S_0$  represents the initial mid-surface area, and the coupling term of membrane and bending work is neglected. Because of  $\mathcal{H}_s^{\alpha\beta\lambda\mu} = \eta \mathcal{H}^{\alpha\beta\lambda\mu} = \frac{\partial^2 w_s}{\partial \underline{\underline{\gamma}}^2}$ , (2.63) becomes

$$\begin{aligned} \forall \underline{\hat{u}}_s, \underline{\hat{\theta}} \in \mathcal{V}, \quad \int_{S_t} \underline{\hat{u}}_s \cdot \underline{\hat{q}}_s dS &= \int_{S_0} \frac{\partial^2 w_s}{\partial \underline{\underline{\gamma}}^2} \gamma_{\alpha\beta} \hat{\gamma}_{\lambda\mu} dS \\ &+ \int_{S_0} \frac{\eta^3}{12} C^{\alpha\beta\lambda\mu} \chi_{\alpha\beta} \hat{\chi}_{\lambda\mu} dS \\ &+ \int_{S_0} \eta D^{\alpha\lambda} \zeta_\alpha \hat{\zeta}_\alpha dS \end{aligned} \quad (2.64)$$

In SMB shell model, the membrane effects can be modeled by either strain-hardening or strain-softening constitutive laws defined by  $w_s$  in section 2.3.4. The bending and shear effects are modeled by the original generalized Hooke's law ( $C^{\alpha\beta\lambda\mu}$  and  $D^{\alpha\lambda}$ ). More details of the derivation of SMB model are available in the book Chapelle & Bathe (2010) or in the thesis Dupont (2014).

## 2.4 Numerical implementation

The fluid-structure interaction problem can be tackled by a coupling method initially proposed by Walter *et al.* (2010), who couples a Boundary Integral Method (BIM) solving for capsule flow with a Finite Element Method (FEM) solving for the wall deformation. In order to account for the membrane thickness and bending resistance, Dupont *et al.* (2015) developed another coupled code where a Shelddon Library designed by Inria and based on Shell Finite Element Method (Shell FEM) couples with BIM through a Parallel Virtual Machine protocol. The library embeds both the basic shell model and SMB model

for selection. However, Dupont's implementation was limited to unbounded flows.

In this section, we follow the coupling approach of Dupont *et al.* (2015) but consider a confined flow situation that is similar to the one of Hu *et al.* (2012): Poiseuille flow in a straight cylindrical channel. We first present the mesh discretization for all flow boundaries. Then we summarize the formulation of Shell FEM for shell equilibrium and the formulation of BIM for capsule flow, followed by introducing the coupling procedure between fluid and solid problems.

### 2.4.1 Mesh discretization for capsule and channel

As the capsule membrane is assumed to be a thin shell with a finite thickness, the mesh type of the capsule thus differs from those of the channel. We discretize all surfaces by flat triangular elements with isoparametric interpolation, in which MITC3 shell elements are used for capsule mid-surface while P1 elements are used for channel surfaces. All unknowns  $(\underline{x}, \underline{u}, \underline{v}, \underline{q})$  are linearly interpolated with the same shape functions. As shown in Figure 2.3, the two elements are plane triangles with 3 nodes. However, MITC3 element is able to interpolate physical quantities associated with thickness by incorporating in-plane and out-of-plane components, such as the position, displacement, and strain. More details about the element property of MITC are available in Lee & Bathe (2004).

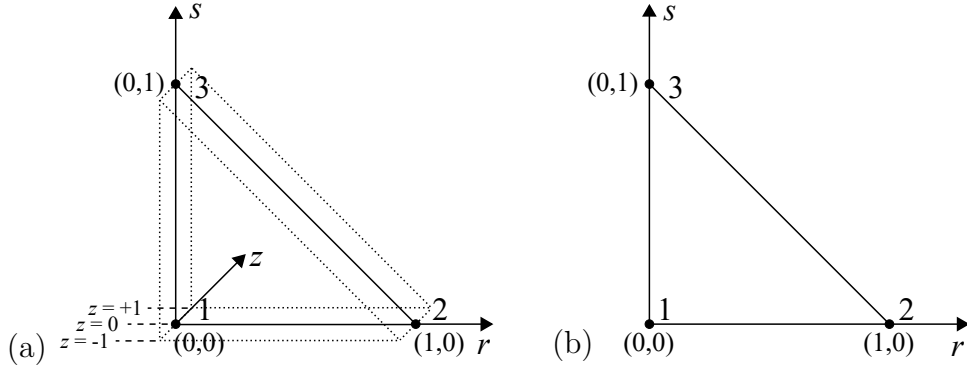


Figure 2.3 – Triangular elements in natural coordinates: (a) MITC3 element; (b) P1 element.

The point position within a given element is located by the natural coordinates of  $(r, s, z)$  for MITC3 and  $(r, s)$  for P1.  $(r, s)$  describes the coordinate in the plane element guaranteed by that  $r, s$ , and  $1 - r - s \in [0, 1]$ . The coordinate  $z$  along  $\underline{a}_3$  ranges from  $-1$  to  $1$ , describing the position through the thickness. We use vector  $\underline{f}$  to denote an arbitrary field quantity, and  $f_{X_j}^{(p)}$  is defined as the  $j^{th}$  Cartesian component of  $\underline{f}$  at node  $p$ , where  $p \in \{1, 2, 3\}$  representing the number of 3 nodes of an element. Thus any interpolated

vector  $\underline{f}$  in this element can be calculated from the nodal values  $\underline{f}^{(p)}$  by

$$\underline{f}(r, s) = \sum_{p=1}^3 \lambda^{(p)}(r, s) \underline{f}^{(p)}, \quad (2.65)$$

where  $\lambda^{(p)}(r, s)$  is the linear shape functions used for MITC3 and P1 elements, defined by

$$\lambda^{(1)}(r, s) = 1 - r - s, \quad \lambda^{(2)}(r, s) = r, \quad \lambda^{(3)}(r, s) = s. \quad (2.66)$$

As an illustration, the interpolated formulation for position  $\underline{v}$  and virtual displacement  $\hat{\underline{u}}$  inside a MITC3 element are expressed as

$$\underline{x}(r, s) = \sum_{p=1}^3 \lambda^{(p)}(r, s) \left( \underline{x}_s^{(p)} + z \frac{\eta}{2} \underline{a}_3^{(p)} \right), \quad (2.67)$$

$$\hat{\underline{u}}(r, s) = \sum_{p=1}^3 \lambda^{(p)}(r, s) \left( \hat{\underline{u}}_s^{(p)} + z \frac{\eta}{2} \hat{\underline{\theta}}^{(p)} \right). \quad (2.68)$$

The interpolated formulation for load  $\underline{q}_s$  inside a P1 element is expressed as

$$\underline{q}_s(r, s) = \sum_{p=1}^3 \lambda^{(p)}(r, s) \underline{q}_s^{(p)}. \quad (2.69)$$

The capsule mesh is obtained as follows: (i) The spherical mid-surface  $S_t$  at the reference state is inscribed with an icosahedron (regular polyhedron with 20 triangular faces) or an octahedron (regular polyhedron with 8 triangular faces); (ii) Placing a new node at the middle of each edge can divide the previous triangular faces into 4 triangular sub-elements, whose nodes are subsequently projected onto the sphere. (iii) Repeating the procedure until attaining the desired number of elements.

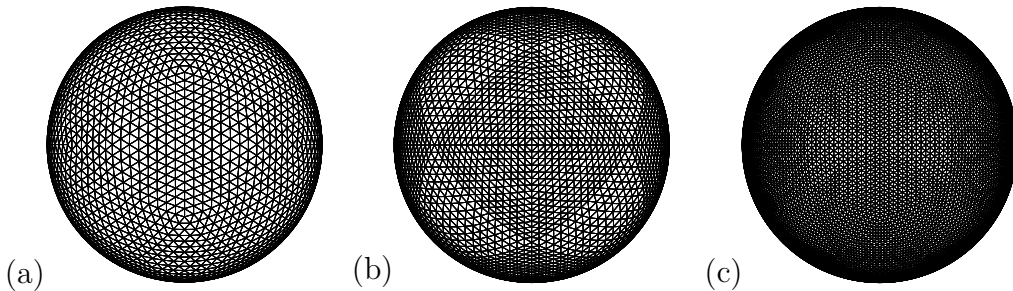


Figure 2.4 – Typical capsule mesh with flat triangles: (a)  $N_E = 5120$ ,  $N_N = 2562$ , from icosahedron; (b)  $N_E = 8192$ ,  $N_N = 4098$ , from octahedron; (c)  $N_E = 20480$ ,  $N_N = 10242$ , from icosahedron.

Capsule meshes generated by following the above method are shown in Figure 2.4, which shows that the mesh generated from an icosahedron is more symmetrical and ho-

mogeneous than the one obtained from an octahedron. We denote  $N_E$  and  $N_N$  as the total number of elements and nodes. Table 2.1 summarizes the information of different capsule meshes about the number of elements and nodes and the characteristic length  $\Delta x$  of a single triangle mesh. Validation of the mesh precision is presented in section 2.5.

Capsule mesh	$N_E$	$N_N$	$\Delta x/a$
1	1280	642	0.15
2	2048	1026	0.12
3	5120	2562	0.075
4	8192	4098	0.06
5	20480	10242	0.038

Table 2.1 – Information of different capsule meshes: number of elements  $N_E$ , number of nodes  $N_N$ , and mesh size  $\Delta x/a$ . Capsule mesh 2 and 4 are obtained from an octahedron.

The channel surfaces required mesh discretizations are the channel wall  $W$  and the outlet  $S_{out}$ . We use the Shelddon Library designed by Inria to generate the channel mesh based on P1 elements. The procedure is implemented as follows: (i) Using unstructured triangular element with the desired mesh size to discretize a circular geometry of the tube cross-section; (ii) Extruding the circular cross-section for a given length to generate the volume mesh of the cylindrical channel, in which the central section has a more refined mesh than the inlet and outlet sections. (iii) The final mesh prepared for the simulation is extracted from the surface mesh on the wall  $W$  and the outlet  $S_{out}$ .

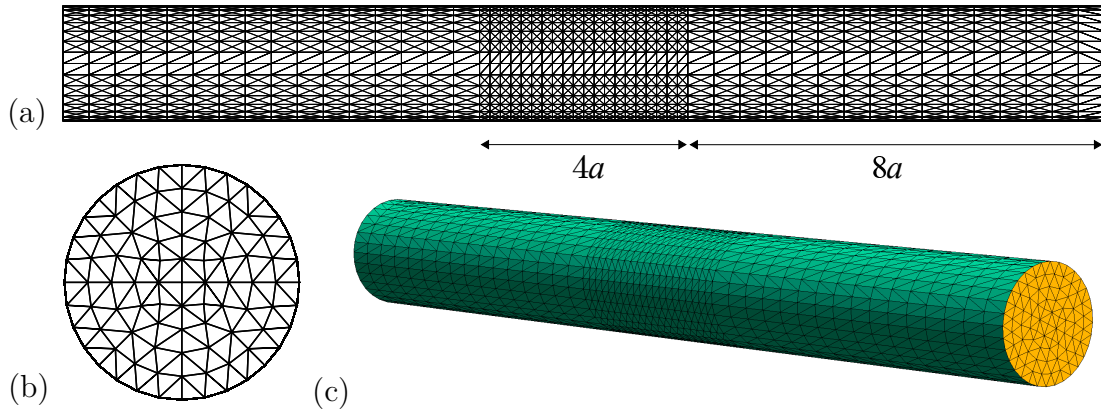


Figure 2.5 – Meshes of the cylindrical channel: (a) Meshes in  $W$ ; (b) Meshes in  $S_{out}$ ; (c) Side view of the channel mesh.

We set the length scale as the capsule initial radius  $a$ . The channel radius thus depends on the selected size ratio  $a/l$ . For a cylindrical channel with a given  $a/l = 0.9$ , the total length of the channel is  $20a$  in order to avoid the inlet and outlet effects, in which the regular and refined sections have lengths  $8a$  and  $4a$ , with a characteristic mesh size of

$\Delta x' = 0.2a$  and  $0.15a$ , respectively. The channel mesh and the corresponding information are presented in Figure 2.5 and Table 2.2.

Channel mesh		$\Delta x'/a$	$N'_E$	$N'_N$
$W$	regular ( $8a$ )	0.2	3480	1757
	refined ( $4a$ )	0.15		
$S_{out}$		0.15		

Table 2.2 – Information of the channel mesh: number of elements  $N'_E$ , number of nodes  $N'_N$ , and mesh size  $\Delta x'/a$ .

It is worth mentioning that the channel meshing scheme in Fig. 2.5 follows the study of Hu (2013), who has demonstrated that this mesh precision can ensure the accuracy of steady-state results. As the boundary integral algorithm for the fluid problem is the same as Hu (2013), we employ the same scheme for channel meshing in this dissertation.

## 2.4.2 Finite element formulation for shell equilibrium

Rather than rewriting the shell mathematical model introduced in section 2.3.6, we use the Shelddon Library designed by Inria, which has embedded both the basic shell model and SMB model. A Parallel Virtual Machine protocol is employed to couple the Shelddon Library with a fluid solver developed in the Biomechanics and Bioengineering Laboratory and adapted for confined flow (Hu *et al.*, 2012; Hu, 2013).

For a given deformed capsule shape, the unknown viscous load  $\underline{q}$  exerted by the fluids on the shell is determined from the weak form of shell equilibrium equation (2.60). In order to express Eq. (2.60) as linear algebraic equation sets at the mid-surface nodes, the integral over the shell volume on the left-hand side is firstly decomposed into a sum over all individual elements on the mid-surface, expressed as

$$\begin{aligned}
 \int_{S_t} \hat{\underline{u}}_s \cdot \underline{q}_s dS &= \sum_{el} \hat{u}_{X_j}^{(p)} \left( \int_0^1 \int_0^{1-s} \lambda^{(p)} \lambda^{(q)} \sqrt{|a_{\alpha\beta}|} dr ds \right) q_{X_j}^{(q)}, \\
 &= \sum_{el} \{\hat{u}_{el}\}^T [M_{el}] \{q_{el}\},
 \end{aligned} \tag{2.70}$$

where  $el$  represents the element number.  $\sqrt{|a_{\alpha\beta}|} dr ds$  is the local differential surface element that requires recalculation at each time step. The vectors  $\{q_{el}\}$  and  $\{\hat{u}_{el}\}$  represent the Cartesian components of the discrete load and virtual displacement of the 3 nodes

within an element:

$$\begin{aligned}\{q_{el}\} &= \left\{ q_1^{(1)}, q_2^{(1)}, q_3^{(1)}, \quad q_1^{(2)}, q_2^{(2)}, q_3^{(2)}, \quad q_1^{(3)}, q_2^{(3)}, q_3^{(3)} \right\}, \\ \{\hat{u}_{el}\} &= \left\{ \hat{u}_1^{(1)}, \hat{u}_2^{(1)}, \hat{u}_3^{(1)}, \quad \hat{u}_1^{(2)}, \hat{u}_2^{(2)}, \hat{u}_3^{(2)}, \quad \hat{u}_1^{(3)}, \hat{u}_2^{(3)}, \hat{u}_3^{(3)} \right\}.\end{aligned}\quad (2.71)$$

Since there are  $N_N$  nodes discretized on the mid-surface, we then assemble the vectors  $\{q_{el}\}$  and  $\{\hat{u}_{el}\}$  into their global counterparts  $\{q_s\}$  and  $\{\hat{u}_s\}$  of size  $3N_N$ , and assemble the matrix  $[M_{el}]$  into  $[M]_s$  of size  $3N_N \times 3N_N$ . The left-hand side of Eq. (2.60) becomes

$$\int_{S_t} \hat{u}_s \cdot \underline{q}_s dS = \{\hat{u}_s\}^T [M]_s \{q_s\}. \quad (2.72)$$

The right-hand side of the shell equilibrium equation (2.60) can also be discretized element-wise as

$$\int_{V_0} \hat{\underline{\underline{e}}}(\hat{\underline{u}}) : \underline{\underline{\Sigma}} dV = \sum_{el} \int_0^1 \int_0^{1-s} \int_{-1}^1 \hat{e}_{ij} \Sigma^{ij} \sqrt{|A_{\alpha\beta}|} \sqrt{|G_{33}|} dr ds dz. \quad (2.73)$$

The Green-Lagrange strain tensor and the second Piola-Kirchhoff stress tensor are needed to be discretized according to the nodal displacements. Eq. (2.60) becomes

$$\{\hat{u}_s\}^T [M]_s \{q_s\} = \{\hat{u}_s\} \{R\} (\{u_s\}, \{\theta\}), \quad (2.74)$$

where the vector  $\{R\}$  of size  $5N_N$  (freedom degree of 3 for the displacement and of 2 for the rotation) contains the elasticity coefficients of the shell material. See more details on the discretization in Batoz & Dhatt (1992) (p. 324 - 325).

Since any virtual displacements are satisfied, Eq. (2.74) is then simplified as

$$[M]_s \{q_s\} = \{R\} (\{u_s\}, \{\theta\}), \quad (2.75)$$

or simplified into a form by separating the freedom degree of the in-plane from the out-plane:

$$\begin{cases} \{R\}_s (\{u_s\}, \{\theta\}) - [M]_s \{q_s\} = \{0\}_s, & (2.76a) \\ \{R\}_\theta (\{u_s\}, \{\theta\}) = \{0\}_\theta, & (2.76b) \end{cases}$$

where the freedom degrees of the mid-surface displacement  $\{u_s\}$  are known from the fluid problem by time integration of Eq. (2.11), while the viscous loads  $\{q_s\}$  and the rotations  $\{\theta\}$  are unknowns. To solve this system, Newton's method is first applied to solve Eq. (2.76b) for  $\{\theta\}$ , which are next used in (2.76a) to solve for  $\{q_s\}$ . More details on the computing process can be found in Dupont (2014).

### 2.4.3 Boundary integral formulation for capsule flow

Once the viscous loads  $\{q_s\}$  are obtained from solving Eq. (2.75), the additional pressure drop defined in (2.18) can be discretized into a linear system of algebraic equations as

$$\begin{aligned}\Delta P &= \sum_{el} \frac{1}{Q} \{v_{el}^\infty\} [M_{el}] \{q_{el}\}, \\ &= \frac{1}{Q} \{v^\infty\} [M]_s \{q_s\},\end{aligned}\tag{2.77}$$

where the undisturbed velocity  $\underline{v}^\infty$  is given by Eq. (2.14). Since the boundary integral is performed on the mid-surface  $S_t$ , the Cartesian components of undisturbed velocity of the 3 nodes within an element, denoted by  $\{v_{el}^\infty\}$ , can also be assembled into its global counterpart of size  $3N_N$ , denoted by  $\{v^\infty\}$ .

With knowing the values of  $\Delta P$  and  $q_s$ , Eq. (2.19) for determining the wall friction  $\underline{f}$  are then discretized into a set of algebraic equations as

$$0 = [J]_s^W [M]_s \{q_s\} + [J]_W^W [M]_W \{f\} - \Delta P [J]_{out}^W [M]_{out} \{n_{out}\},\tag{2.78}$$

where  $[J]_s^W$ ,  $[J]_W^W$ , and  $[J]_{out}^W$  represent the matrices of Green's functions integrating on the surfaces  $S_t$ ,  $W$ , and  $S_{out}$ . We denote the total number of nodes on the channel wall  $W$  and the outlet  $S_{out}$  by  $N_N^W$  and  $N_N^{out}$ . Thus  $[J]_s^W$ ,  $[J]_W^W$ , and  $[J]_{out}^W$  have the size of  $3N_N^W \times 3N_N$ ,  $3N_N^W \times 3N_N^W$ , and  $3N_N^W \times 3N_N^{out}$ , respectively. The normal vector  $\{n_{out}\}$  on the outlet has the size of  $3N_N^{out}$ . The matrices  $[M]_W$  and  $[M]_{out}$  are built in the same way as  $[M]_s$ , which are the integrals of the shape functions to the surfaces  $W$  and  $S_{out}$ . It is worth noting that  $[M]_W$  and  $[M]_{out}$  are only calculated once at the beginning of the procedure due that the channel boundary surfaces are fixed. However,  $[M]_s$  on the mid-surface needs to be recalculated at each time step since the capsule geometry evolves with time.

Finally, the velocity of the nodes on the mid-surface  $\underline{v}(\underline{x}_s)$  defined in Eq. (2.13) is assembled by

$$\{v\} = \{v^\infty\} - \frac{1}{8\pi\mu} [J]_s [M]_s \{q_s\} - \frac{1}{8\pi\mu} [J]_W^s [M]_W \{f\} + \frac{\Delta P}{8\pi\mu} [J]_{out}^s [M]_{out} \{n_{out}\},\tag{2.79}$$

where the matrices of Green's functions  $[J]_s$ ,  $[J]_W^s$ , and  $[J]_{out}^s$  have the size of  $3N_N \times 3N_N$ ,  $3N_N \times 3N_N^W$ , and  $3N_N \times 3N_N^{out}$ , respectively.

Since the viscous load  $\{q_s\}$ , the pressure drop  $\Delta P$ , and the channel wall friction  $\{f\}$  are already determined by equations (2.75), (2.77), and (2.78), thus solving the linear equation (2.79) can obtain the mid-surface velocity vector  $\{v\}$ .

## 2.4.4 Coupling Shell FEM + BIM procedure

A Shell FEM+BIM code has been proposed by Dupont et al. for unbounded capsule flow (Dupont, 2014; Dupont *et al.*, 2015), while a FEM+BIM code has been proposed by Hu et al. for bounded capsule flow (Hu *et al.*, 2012; Hu, 2013). Following their work, we construct a new coupled Shell FEM+BIM code that is adapted for the capsule in confined flow as follows:

### 1. Initialization

An initially spherical capsule and a channel corresponding to a certain size ratio are discretized with desired mesh sizes, as indicated in section 2.4.1. All nodes on mid-surface at reference configuration are identified and recorded in a reference position vector  $\underline{X}_s$ . The capsule mass center at the reference state is also computed and stored in another position vector  $\underline{X}_{sO}$ .

### 2. Viscous load $\underline{q}_s$

The positions of the mid-surface nodes at any time  $t$  are denoted by  $\underline{x}_s(\underline{X}_s, t)$ . Then solving Eq. (2.60) to obtain the mid-surface viscous load  $\underline{q}_s$ .

### 3. Mid-surface velocity $\underline{v}$

Knowing the viscous load  $\underline{q}_s$  on the mid-surface, the additional pressure drop  $\Delta P$  and disturbance wall friction  $\underline{f}$  are solved by equations (2.18) and (2.19), respectively. Incorporating  $\underline{q}_s$ ,  $\Delta P$ , and  $\underline{f}$  into Eq. (2.13), we obtain the velocity  $\underline{v}$  of each node on the mid-surface.

### 4. Mid-surface displacement $\underline{u}_s$

The displacement  $\underline{u}_s$  of each node is calculated by time-integrating over Eq. (2.11) using an explicit Euler method, which causes that the numerical method is conditionally stable if the time step  $\Delta t$  satisfies a stability criterion

$$\Delta t \frac{V}{a} < \mathcal{O} \left( \frac{\Delta x}{a} C a_s \right) \quad (2.80)$$

### 5. New position of mid-surface

The new position  $\underline{x}$  of mid-surface nodes at time  $t + \Delta t$  is computed by

$$\underline{x}_s(\underline{X}_s, t + \Delta t) = \underline{X}_s + \underline{u}_s(\underline{X}_s, t + \Delta t). \quad (2.81)$$



It is worth noting that the new mass center  $x_{sO}$  is recomputed at each time step, and the positions of mid-surface nodes are then moved by  $-z_O \underline{e}_z$  to the central section of the channel.

## 6. Steady-state results

The numerical procedure repeats steps 2 to 6 until reaching a steady-state capsule shape, at which the mid-surface area varies by less than  $5 \times 10^{-4} \times (4\pi a^2)$  over a non-dimensional time  $tV/a = 1$ .

## 2.5 Validation

The validity and applicability of the Shell FEM+BIM model are verified in this section. We first check the spatial and time convergence in section 2.5.1 to provide an appropriate mesh size and time step to the problem. In section 2.5.2, we compare the shell solution with  $\alpha = 0.01$  (very weak bending rigidity of the material) with the results generated by a membrane model constructed by Hu et al. (Hu *et al.*, 2012; Hu, 2013), where the membrane is assumed as an infinitely thin surface without thickness and bending resistance. Finally, an application condition is provided in section 4.1 to ensure the numerical predictions are within the feasibility of the model.

### 2.5.1 Convergence study

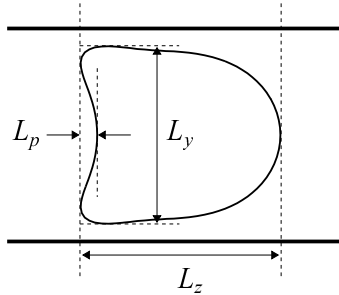


Figure 2.6 – Typical lengths characterizing the capsule deformation measured in the longitudinal plane along the center of mass.  $L_z$ , the axial length;  $L_y$ , the width;  $L_p$ , the parachute depth.

The numerical stability of the coupled code can be verified by investigating the effect of mesh sizes and time steps on the steady-state typical lengths shown in Fig. 2.7:  $L_z$ ,  $L_y$ , and  $L_p$ , which respectively denote the axial length, the width, and the parachute depth measured in the longitudinal plane along the center of mass. Since there is no theoretical solution to this nonlinear solid-structure interaction problem, we choose the results of

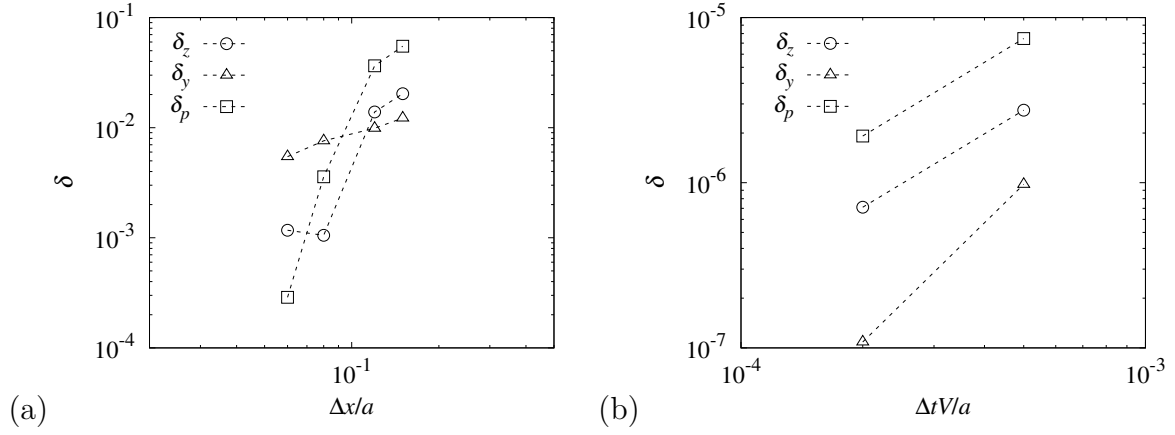


Figure 2.7 – Relative error  $\delta$  based on the typical lengths  $L_z$ ,  $L_y$ , and  $L_p$  for the case of  $a/l = 0.9$ ,  $\alpha = 0.01$ , and  $Ca_s = 0.05$ . NH law governs the membrane behaviors. (a) Spatial convergence (reference corresponding to  $N_E = 20480$ , time step is fixed with  $\Delta tV/a = 1 \times 10^{-4}$ ); (b) Time convergence (reference corresponding to  $\Delta tV/a = 1 \times 10^{-4}$ , capsule mesh is fixed with  $N_E = 8192$ ).

those lengths obtained with the most refined mesh ( $N_E = 20480$ ) and the very small time step ( $\Delta tV/a = 1 \times 10^{-4}$ ) as references for the spatial and temporal convergence studies. The relative numerical error  $\delta$  is defined by

$$\delta = \frac{|L - L^{ref}|}{L^{ref}}. \quad (2.82)$$

We consider an initially spherical capsule with  $a/l = 0.9$  and  $\alpha = 0.01$  subjected to a confined Poiseuille flow with  $Ca_s = 0.05$ . Neo-Hookean (NH) law is used to govern the membrane behaviors. Fig. 2.7 (a) shows the results of  $\delta_z$ ,  $\delta_y$ , and  $\delta_p$  as a function of the mesh size  $\Delta x/a$ , in which the reference case uses  $N_E = 20480$  and  $\Delta tV/a = 1 \times 10^{-4}$  is fixed for all simulations. We note that  $\delta_z$  is almost the same for  $\Delta x/a \leq 8 \times 10^{-2}$ , which implies that  $N_E = 5120$  might be enough to predict the longitudinal deformation. However, considering  $\delta_y$  and  $\delta_p$  decreasing with refining the mesh, using 8192 elements can ensure accuracy and without loss of efficiency.

The influence of the time step on the temporal convergence is presented in Fig. 2.7 (b) using  $\Delta tV/a = 1 \times 10^{-4}$  for the reference and  $N_E = 8192$  for all cases. We find that  $\delta_z$ ,  $\delta_y$ , and  $\delta_p$  decrease by reducing the time step  $\Delta tV/a$ . It should be noted that the larger time step of  $\Delta tV/a = 5 \times 10^{-4}$  can yield errors smaller than  $1 \times 10^{-5}$  and it also satisfies the stability criterion of Eq. (2.80). In view of the above convergence results, the following simulations are based on  $N_E = 8192$  and  $\Delta tV/a = 5 \times 10^{-4}$  (unless otherwise specified).

### 2.5.2 Comparison with membrane model

As the bending resistance of a very thin membrane can be neglected, it is possible to compare the shell solution with  $\alpha = 0.01$  to the results obtained by a membrane model (Hu *et al.*, 2012; Hu, 2013) where no bending resistance is included, i.e.,  $\alpha = 0$ . The confinement ratio is  $a/l = 0.9$  and the flow strength is  $Ca_s = 0.05$ . The membrane behaviors are governed by the NH law. We obtain capsule profiles in the longitudinal plane and the cross-section plane, both cutting along the center of mass, as shown in Fig. 2.8.

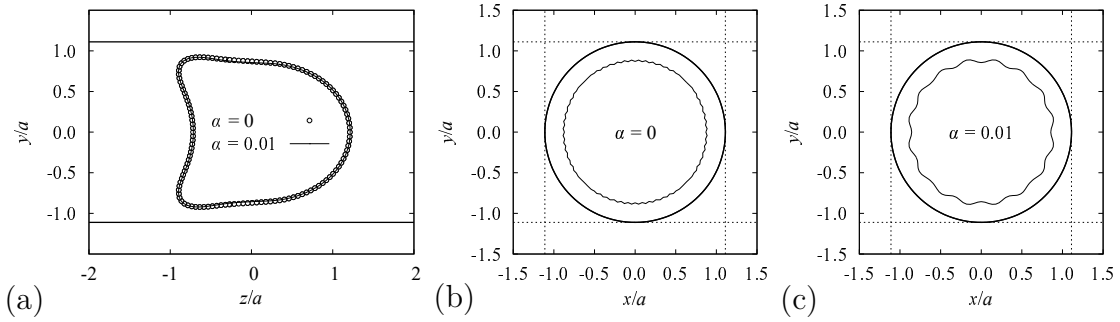


Figure 2.8 – Comparison of capsule profiles predicted by membrane ( $\alpha = 0$ ) and shell ( $\alpha = 0.01$ ) models.  $a/l = 0.9$  and  $Ca_s = 0.05$ . NH law governs the membrane behaviors. (a) Capsule profiles in longitudinal plane; (b) and (c) Capsule profiles in the cross-section plane. All profiles are cut along the center of mass.

Fig. 2.8 (a) shows the comparison of longitudinal profiles obtained from the membrane and the shell solutions. Since  $\alpha = 0.01$  corresponds to a very weak bending rigidity of the material, the two profiles of shell and membrane solutions are superimposed very well, implying that the membrane surface stretching dominates the capsule global deformation.

Hu *et al.* (2012) has reported that wrinkles or folds predicted by the membrane model are formed on the side of the deformed capsule where the membrane is under compression. However, since their model neglects the bending resistance, wrinkles are actually numerical by-products in the form of oscillations, as seen in Fig. 2.8 (b). By contrast, although accounting for a weak bending resistance with  $\alpha = 0.01$ , the shell model is capable of predicting regular waveforms with periodic peaks and troughs shown in Fig. 2.8 (c). It indicates that the shell model must be employed if one wants to numerically predict the physical wrinkles that are composite products of bending and stretching deformations.



# Capsule in unbounded parabolic flow

In this chapter, we use the Shell FEM+BIM model to investigate the motion and deformation of an initially spherical liquid-filled capsule flowing in an unbounded parabolic flow, as shown in Fig. 3.1 (a). The capsule membrane is modeled as a thin shell characterized by a mid-surface and a finite thickness, which have been depicted in section 2.3. The undisturbed external flow is assumed as an unbounded parabolic flow. It has the same velocity profile as the Poiseuille flow defined by Eq. (2.14), in which the velocity is equal to 0 as  $y = \pm l$ . Since there is no external boundary in this flow configuration, the velocity vector in the flow domain is simplified from Eq. (2.13) as follows

$$\underline{v}(\underline{x}) = \underline{v}^\infty(\underline{x}) - \frac{1}{8\pi\mu} \int_{S_t} \underline{J}(\underline{r}) \cdot \underline{q}_s dS(\underline{y}). \quad (3.1)$$

We first verify the accuracy of the result predicted by the shell model in the unconfined parabolic flow. Then we investigate the effects of flow strength and shell thickness on capsule dynamic responses. Finally, the relationship between the bending energy and membrane curvature is discussed and revealed. Neo-Hookean (NH) constitutive law is used in this chapter to govern the elastic behavior of the mid-surface.

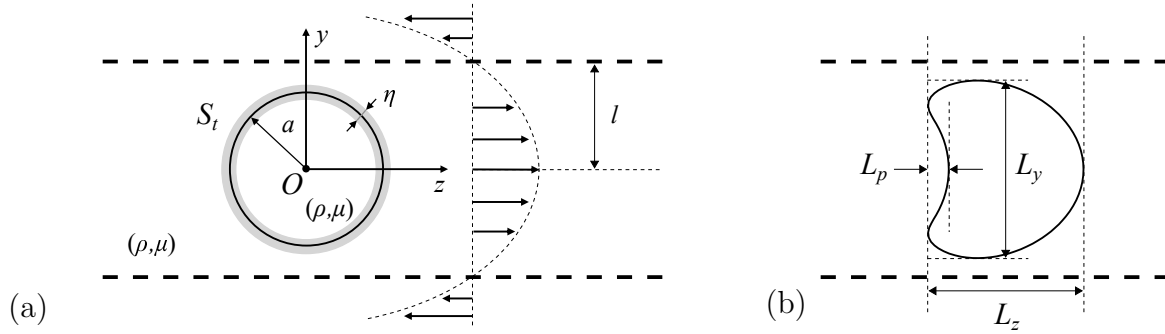


Figure 3.1 – (a) Schematic illustration of an initially spherical capsule with radius  $a$  and finite thickness  $\eta$  subjected to parabolic flow with characteristic length  $l$ ; (b) Typical lengths characterizing the capsule deformation.

### 3.1 Validation

As the parabolic flow has no external boundaries and confinements, the capsule membrane is not squeezed as the bounded flow case and thus the wrinkle cannot form. This has two benefits: (i) The computation speed of the code is faster than the bounded flow case. (ii) The numerical calculation is more stable because it is not affected by the structural instability caused by the generation of wrinkles. As a result, we can employ capsule mesh with  $N_E = 5120$  ( $\Delta x/a = 0.075$ ) and time step of  $\Delta t V/a = 5 \times 10^{-4}$  for simulations in the following (unless otherwise specified).

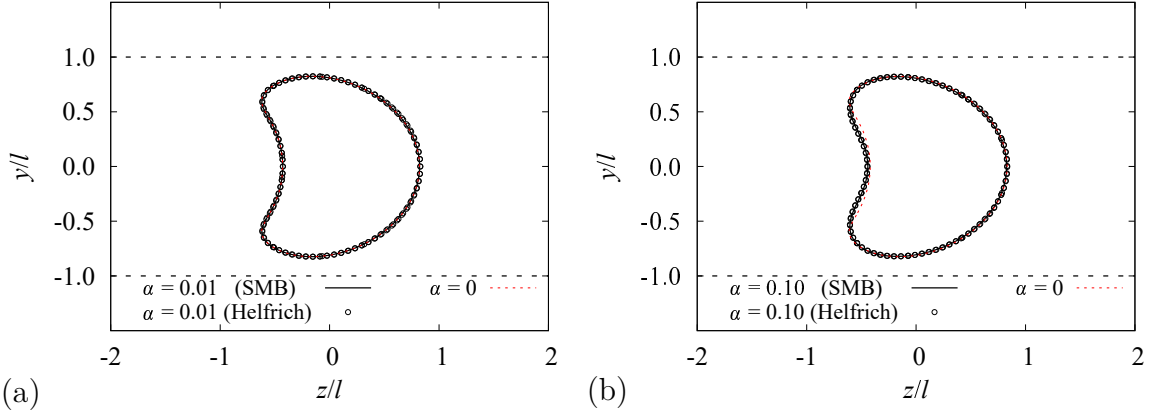


Figure 3.2 – Comparison of capsule profiles obtained by SMB model and Helfrich model. Size ratio  $a/l = 0.8$  and surface capillary number  $Ca_s = 0.05$ . Wall thickness ratio  $\alpha = 0.01$  (a), and  $\alpha = 0.10$  (b). The red dotted line represents the results obtained from a membrane model with  $\alpha = 0$ .

We have performed a comparison between the results obtained from the present SMB shell model, and the results obtained by Prof. Stephan Gekle and his team (Bayreuth University, Germany), who use a finite element membrane model along with the Helfrich law to account for a capsule with membrane bending resistance, in which the total energy is summed up by the Helfrich bending energy with membrane elastic energy. We call this model as Helfrich model hereinafter. Theory and algorithms are available in reference (Guckenberger & Gekle, 2017).

As shown in Fig. 3.2, the comparison considers the same conditions: an initially spherical capsule with a size ratio  $a/l = 0.8$  and thickness ratios  $\alpha = 0.01$  and  $0.10$  subject to an unconfined Poiseuille flow with surface capillary number  $Ca_s = 0.05$ . The membrane elastic behavior follows the neo-Hookean (NH) law. We also plot the profile obtained by the membrane model ( $\alpha = 0$ ) for the same size ratio and flow intensity, denoted by the red dotted line. The results show that the capsule longitudinal profiles predicted by SMB and Helfrich models can be superimposed very well both when  $\alpha = 0.01$  and  $0.10$ . In addition, the solutions of two bending models with  $\alpha = 0.01$  also converge to the membrane

solution, which implies that membrane stretching is dominant in the capsule deformation due to the small bending resistance. When  $\alpha$  increases to 0.10, the profiles of SMB and Helfrich model deform less in the rear concave than the one generated by the membrane model. It indicates that the increased wall bending rigidity can restrict the deformation. Since the thickness ratio  $\alpha = 0.10$  is the conventional limit of the thin shell hypothesis (Rachik *et al.*, 2006), we will employ  $\alpha \leq 0.10$  in the following studies.

## 3.2 Capsule axial deformation

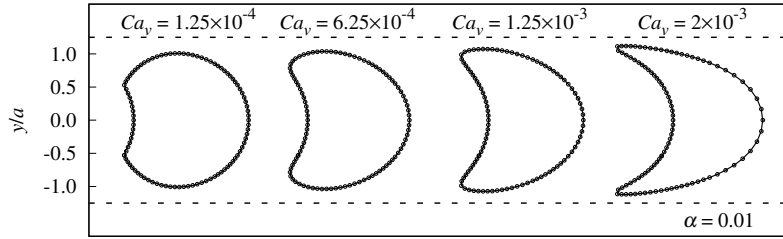


Figure 3.3 – Effect of the bulk capillary number  $Ca_v$  on capsule deformation. Size ratio  $a/l = 0.8$  and wall thickness ratio  $\alpha = 0.01$ .  $Ca_v$  varies from  $1.25 \times 10^{-4}$  to  $2 \times 10^{-3}$ . Circle dots represents the membrane solution with  $\alpha = 0$  and surface capillary number  $Ca_s = 0.0125, 0.0625, 0.125$ , and  $0.2$ , respectively.

We begin with investigating the effect of bulk capillary number on the capsule deformation in an unbounded Poiseuille flow, as shown in Fig. 3.3 for an initially spherical capsule with  $a/l = 0.8$ . The steady-state profiles in the longitudinal plane correspond to the initially spherical capsule with  $\alpha = 0.01$ . The bulk capillary number  $Ca_v$  increases from  $1.25 \times 10^{-4}$  to  $2 \times 10^{-3}$ . We find that the capsule exhibits a parachute shape with curvature inversion in the rear, at which the membrane has a sharp edge with large curvatures at high flow intensities. It illustrates that the capsule deformation increases with  $Ca_v$ . Since the bending resistance of a shell with  $\alpha = 0.01$  is very small, those results are equivalent to the ones obtained by a membrane model with  $\alpha = 0$ , as seen in the circle dots, in which a surface capillary number defined in Eq. (2.6) is employed for a membrane neglecting the thickness. It is worth mentioning that there exist stability limits of  $Ca_s$  for capsules with a neo-Hookean membrane. Once  $Ca_s$  exceeds this critical value, the capsule will elongate continuously with no steady shape (Hu *et al.*, 2013).

Fig. 3.4 shows the steady-state profiles of an initially spherical capsule with  $a/l = 0.8$  and different wall thickness ratios.  $Ca_v = 1.25 \times 10^{-3}$ , and  $\alpha$  varies from 0.01 to 0.10. When  $\alpha = 0.01$ , the capsule predicts a fairly large deformation due to the fact that the shell bending resistance is very small and can be neglected. Increasing  $\alpha$  to 0.02 and 0.05, the deformation of the capsule gradually decreases with an increasing bending resistance.

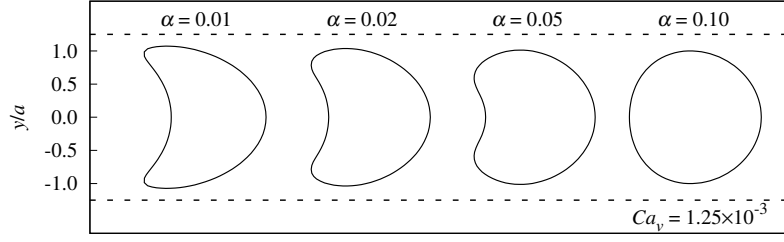


Figure 3.4 – Effect of wall thickness ratio  $\alpha$  on capsule deformation. Size ratio  $a/l = 0.8$  and bulk capillary number  $Ca_v = 1.25 \times 10^{-3}$ .  $\alpha$  varies from 0.01 to 0.10.

When the membrane is relatively thick ( $\alpha = 0.10$ ), the bending rigidity greatly restricts the capsule deformation so that the parachute shape cannot form in the back. The results show that in addition to the flow strength, the membrane thickness is also a significant parameter that affects and regulates the deformation of the capsule.

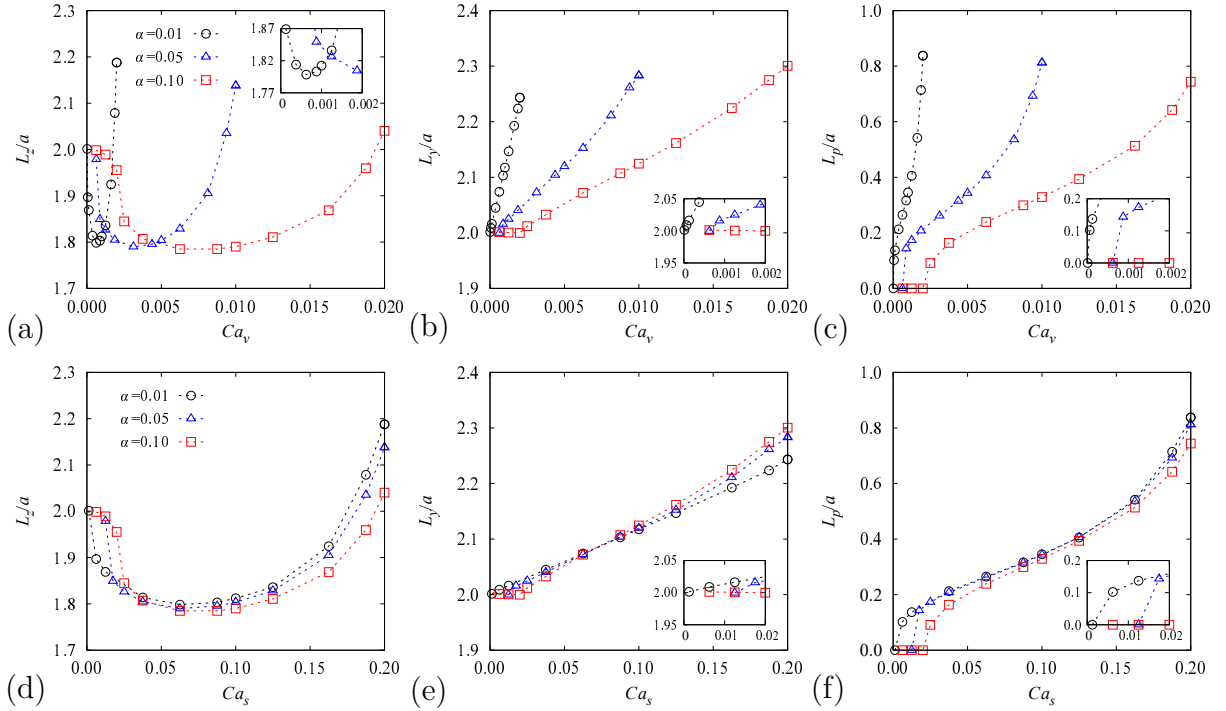


Figure 3.5 – Plots of the capsule typical dimensions as a function of  $Ca_v$  (a, b, c) and  $Ca_s$  (d, e, f).  $a/l = 0.8$ , and  $\alpha = 0.01, 0.05$ , and  $0.10$ . The typical dimensions are axial length  $L_z$ , width  $L_y$ , and parachute depth  $L_p$ .

As shown in Fig. 3.1 (b), we use three typical dimensions, axial length  $L_z$ , width  $L_y$ , and parachute depth  $L_p$ , to measure the capsule deformation. The plots in Fig. 3.5 (a, b, c) give the evolution of the three lengths with the shell thickness ratio  $\alpha$  and the bulk capillary number  $Ca_v$ . The first impression is that the shell thickness greatly influences the deformed capsule shapes. For the same  $L_z$ , a larger thickness corresponds to a higher flow strength  $Ca_v$ . When reducing  $\alpha$ , the applicable  $Ca_v$  is also limited to a small range.



This illustrates that the thicker shell with a larger bending rigidity can effectively resist the viscous force imposed by external fluids. For a given  $\alpha$ ,  $L_z$  firstly decreases and then increases due to the parachute formation. A critical  $Ca_v^c$  is thus obtained at which  $L_p$  starts to be non-zero. It is apparent that  $Ca_v^c$  increases with  $\alpha$ , which also reflects the effect of bending resistance on capsule dynamics. Besides,  $L_y$  increases with  $Ca_v$  because there is no external boundary to impose a squeezing effect on the capsule.

If one plots the deformation as a function of the surface capillary number  $Ca_s$ , as shown in Fig. 3.5 (d, e, f), the curves are almost overlapping for a flow strength range of  $0.03 \leq Ca_s \leq 0.12$ , at which the values of typical lengths for different  $\alpha$  is difficult to be discriminated. It indicates that the capsule deformation in this flow section depends only on the surface capillary number and the bending resistance has a negligible effect on the overall deformed profile. This result is similar to the one from Dupont *et al.* (2015), who have concluded that the stretching of the mid-surface is the prevailing phenomenon based on the study of the effect of bending resistance on capsule deformation in simple shear flow. When  $Ca_s$  is smaller than 0.03 and larger than 0.12, capsule typical lengths have apparent differences for different  $\alpha$ . However, the results of Dupont *et al.* (2015) indicate that  $\alpha$  always has a negligible effect whatever the value of  $Ca_s$ .

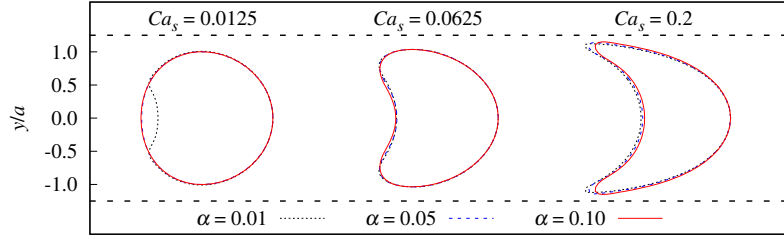


Figure 3.6 – Effect of wall thickness ratio  $\alpha$  on the longitudinal capsule profile at steady-state under a given surface capillary number  $Ca_s$ . Size ratio  $a/l = 0.8$ .

For the sake of illustrating the above phenomenon, we plot the longitudinal profiles of different  $\alpha$  under a given  $Ca_s$ , as shown in Fig. 3.6. For a moderate flow strength with  $Ca_s = 0.0625$ , the profiles of different  $\alpha$  almost superimpose indeed. Under a small flow strength with  $Ca_s = 0.0125$ , the profile of  $\alpha = 0.05$  and  $0.10$  are still very near and no curvature inversion on the shape, while  $\alpha = 0.01$  generates a small concave in the rear due to its negligible bending resistance. When the flow strength is extremely high, e.g.,  $Ca_s = 0.2$ ,  $\alpha = 0.01$  predicts a contour with unrealistic pointed-ends, and the model is almost reaches the stability limit. However, this issue does not occur for  $\alpha = 0.05$  and  $0.10$  because of an increased thickness and bending resistance.

For a given capsule size, if we use  $Ca_s$  instead of  $Ca_v$  to represent the flow strength, increasing the thickness will implicitly decrease the bulk shear modulus  $G$  (inferred from Eq. 2.6) to obtain the same value of  $Ca_s$ . This means that a larger  $\alpha$  leads to a softer

material, which is probably the reason why we observe almost no effect of thickness on typical lengths under a moderate flow strength of  $0.03 \leq Ca_s \leq 0.12$ , shown in Fig. 3.5 (d, e, f). When the flow strength is low, capsules with a very thin wall will produce a small parachute shape with curvature inversions. For an extreme flow strength, capsules with a thick wall will prevent the formation of pointed-ends in the rear of the membrane. Under the above two flow conditions, the capsule deformation will be significantly different with the change of the membrane thickness. This indicates that if one wants to fully understand the influence of wall bending resistance on capsule dynamics, it is necessary to employ a flow environment where the capsule exhibits a curvature reversal shape.

### 3.3 Bending energy-curvature relationship

The dynamics of a capsule subjected to an infinite Poiseuille flow is interesting from a mechanical point of view because (i) the capsule reaches a steady parachute shape that exhibits drastic curvature changes (in value and sign) from the capsule tip to its rear, (ii) membrane wrinkles do not exist since no channel confinements, and (iii) the membrane and bending energies can be directly computed at each point. These features provide convenience for studying the relationship between bending energy and curvature in the deformed membrane.

#### 3.3.1 Physical model accounts for bending

- **Helfrich model**

Helfrich model is the most prevalent model to account for the bending resistance of a capsule membrane. The Helfrich bending law is usually expressed as (Helfrich, 1973)

$$W_b^H = 2M_b(K_M - K_0)^2 + M_G K_G, \quad (3.2)$$

where  $W_b^H$  is bending energy density per unit undeformed area.  $K_M$  and  $K_G$  are the mean and Gaussian curvatures, defined in Eq. (2.29) and (2.30).  $K_0$  is the curvature in the initial state.  $M_b$  is the bending modulus, and  $M_G$  is the Gaussian modulus. According to the Gauss-Bonnet theorem, the Gaussian term can be ignored due to the unchanged topology shapes (Pozrikidis, 2003).

- **SMB model**

The energy density per unit undeformed area for the membrane and bending effects are computed by

$$W_m = \frac{\sum_{n=1}^{N_{el}} E_m}{\sum_{n=1}^{N_{el}} S_0}, \quad (3.3)$$

$$W_b = \frac{\sum_{n=1}^{N_{el}} E_b}{\sum_{n=1}^{N_{el}} S_0}, \quad (3.4)$$

with

$$E_m = \int_{S_0} w_s dS, \quad (3.5)$$

$$E_b = \int_{S_0} \frac{1}{2} \left( \frac{\eta^3}{12} C^{\alpha\beta\lambda\mu} \chi_{\alpha\beta} \chi_{\lambda\mu} \right) dS, \quad (3.6)$$

are energies of membrane and bending in the deformed state.  $N_{el}$  represents the surrounding elements to a given node on the mid-surface. The strain energy function  $w_s$  is given in section 2.3.4. The bending elasticity tensor  $C^{\alpha\beta\lambda\mu}$  is given in Eq. (2.62). The bending strain tensor  $\chi_{\alpha\beta}$  is given in Eq. (2.47). Mathematically, the bending energy density of the present SMB model has the form

$$W_b^{\text{SMB}} = \frac{1}{2} \left( \frac{\eta^3}{12} C^{\alpha\beta\lambda\mu} \chi_{\alpha\beta} \chi_{\lambda\mu} \right). \quad (3.7)$$

The computation of the bending strain  $\chi_{\alpha\beta}$  is usually challenging in practical application since it is associated with the rotation angles to the normal based on the Reissner-Mindlin assumption. If the normal vector is always orthogonal to the mid-surface in the course of deformation and no shearing effect, i.e., following the Kirchhoff-Love assumption,  $\chi_{\alpha\beta}$  can be simplified to the bending deformation tensor  $\psi_{\alpha\beta}$  defined in Eq. (2.33). Eq. (3.7) then becomes

$$W_b^\Psi = \frac{1}{2} \left( \frac{\eta^3}{12} C^{\alpha\beta\lambda\mu} \psi_{\alpha\beta} \psi_{\lambda\mu} \right). \quad (3.8)$$

Substituting the expressions of  $M_b$  (defined in Eq. 2.2) and  $C^{\alpha\beta\lambda\mu}$  into Eq. (3.8), and assuming an incompressible material with Poisson ratio  $\nu = 0.5$ , Eq. (3.8) is rewritten as (A detailed derivation process is available in Appendix A.)

$$W_b^\Psi = 2M_b\Psi_M^2 - 0.5M_b\Psi_G. \quad (3.9)$$

Comparing Eq. (3.2) with (3.9), the two formulas have similar forms. However,  $(K_M - K_0)$  and  $\Psi_M$  are different measurements accounting for bending (likewise for  $K_G$  and  $\Psi_G$ ), and the difference between the two variables has not been studied yet. For the sake of accuracy and without loss of generality, we employ the initial spherical capsule with a size ratio of  $a/l = 1.0$ , and the mid-surface is discretized with 20480 triangular elements ( $\Delta x/a = 0.038$ ).

### 3.3.2 Comparison of bending measurement

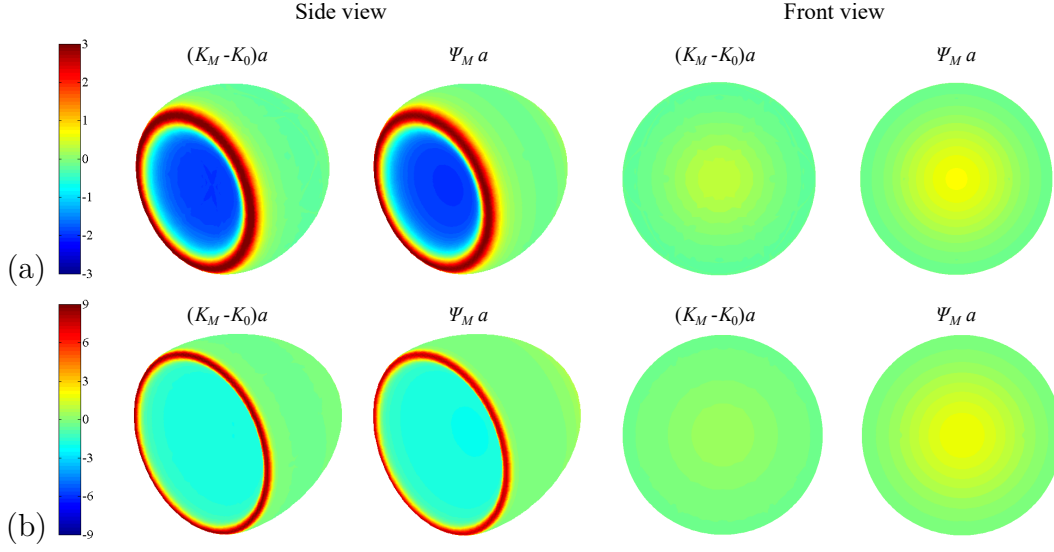


Figure 3.7 – The steady-state shape of an initially spherical capsule with  $a/l = 1.0$  and  $\alpha = 0.01$  subjected to an infinite parabolic flow: (a)  $Ca_s = 0.05$ ; (b)  $Ca_s = 0.10$ . The color code represents the value of mean curvature change  $(K_M - K_0)a$  and mean bending deformation  $\Psi_M$ .

Fig. 3.7 shows the value of mean curvature change  $(K_M - K_0)a$  and mean bending deformation  $\Psi_M a$  on a steady-state capsule mid-surface. The initial size ratio  $a/l = 1.0$  with wall thickness ratio  $\alpha = 0.01$ . The flow strength  $Ca_s = 0.05$  (a) and  $0.10$  (b). We find that under small and large capillary numbers, the two types of results have similar patterns: the convex has positive values while the values are negative in concave. The rear bending membrane exhibits a ring-shaped area with relatively large  $(K_M - K_0)a$  and  $\Psi_M a$ . One apparent difference between the two patterns is that the magnitude of  $(K_M - K_0)a$  in the capsule's tip is smaller than the magnitude of  $\Psi_M a$  in the same region.

For convenience, we divide the deformed mid-surface into five regions distinguished by colors, as shown in Fig. 3.8 (a). The convex with positive curvatures is divided into three regions marked by purple, gray, and green. In concave, blue marks the area with negative curvatures, and the narrow red area represents the curvature transition between positive and negative. In Fig. 3.8 (b), we plot the invariant  $I_{s1}$  (Eq. 2.49) as a function of the mean curvature change  $(K_M - K_0)a$ . We find that the capsule front (green) has a very high value of  $I_{s1}$  but near-zero  $(K_M - K_0)a$ , demonstrating that this area suffers a huge in-plane stretching and a low bending effect. A drastic change in curvature happens in the area from purple to red, in which the membrane undergoes a significant bending behavior. It is interesting to see that the blue area with negative curvatures is mainly subjected to bending effects with large curvature changes while there is almost no membrane stretching because of small values of  $I_{s1}$ .

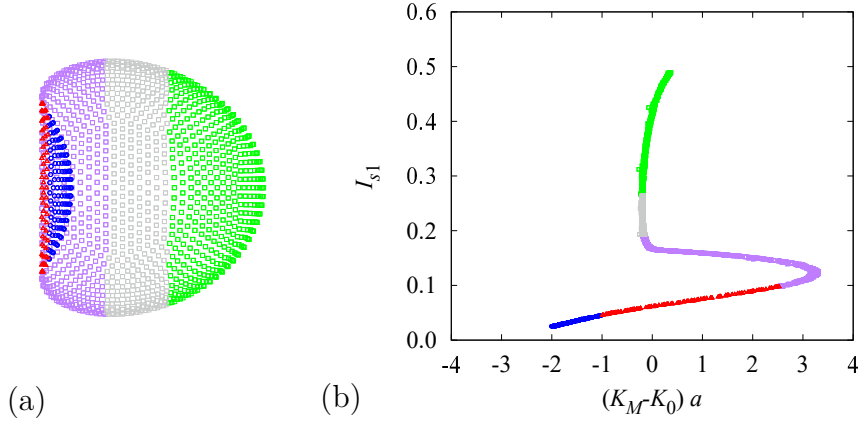


Figure 3.8 – (a) The mid-surface is divided into five regions marked by different colors; (b) The plot of the invariant  $I_{s1}$  as a function of the mean curvature change  $(K_M - K_0)a$  for a case of  $a/l = 1.0$ ,  $\alpha = 0.01$ , and  $Ca_s = 0.05$ .

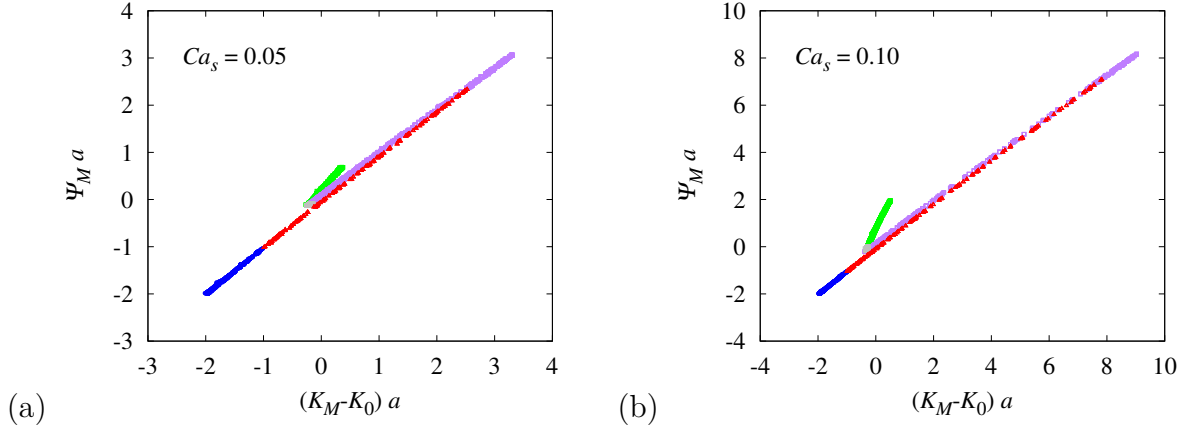


Figure 3.9 – The mean bending deformation  $\Psi_M a$  is plotted as a function of the mean curvature change  $(K_M - K_0)a$ . The cases considered are  $a/l = 1.0$ ,  $\alpha = 0.01$ ,  $Ca_s = 0.05$  (a), and  $Ca_s = 0.10$  (b).

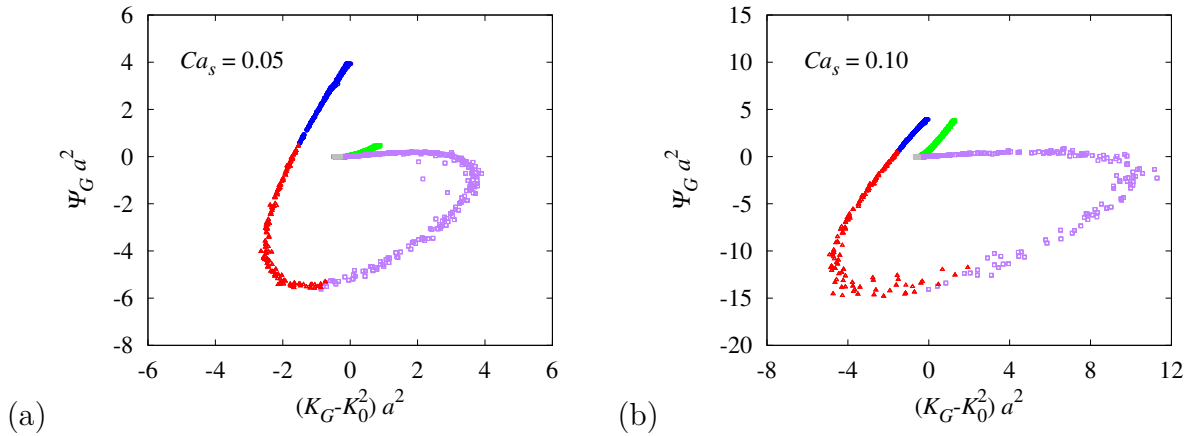


Figure 3.10 – The Gaussian bending deformation  $\Psi_G a^2$  is plotted as a function of the Gaussian curvature change  $(K_G - K_0^2)a^2$ . The cases considered are  $a/l = 1.0$ ,  $\alpha = 0.01$ ,  $Ca_s = 0.05$  (a), and  $Ca_s = 0.10$  (b).

In order to quantify the difference between  $\Psi_M a$  and  $(K_M - K_0)a$ , we plot  $\Psi_M a$  as a function of  $(K_M - K_0)a$ , as shown in Fig. 3.9. It is visible that the two variables are almost identical for most nodes, except for the nodes in front of the capsule. We make a subtraction between the two variables in math, and then we find an expression

$$\Psi_M - (K_M - K_0) = \frac{1}{2} \left( \kappa_{11} \left( \frac{\lambda_1^2 - 1}{\lambda_1^2} \right) + \kappa_{22} \left( \frac{\lambda_2^2 - 1}{\lambda_2^2} \right) \right) \quad (3.10)$$

by assuming that there exists an orthogonal unit basis  $(\underline{A}_1, \underline{A}_2)$  along principal directions of the Cauchy-Green deformation tensor  $\underline{C}_s$  (Eq. 2.48).  $\lambda_{s1}$  and  $\lambda_{s2}$  are corresponding principal dilatation ratios. The expression indicates that a small in-plane deformation with  $\lambda_{s1} \approx 1$  and  $\lambda_{s2} \approx 1$  (or  $I_{s1} \approx 0$ ) leads to  $\Psi_M \approx (K_M - K_0)$ . However,  $\Psi_M > (K_M - K_0)$  is obtained for the area suffering a relatively large membrane stretching, i.e.,  $\lambda_{s1} \gg 1$  and  $\lambda_{s2} \gg 1$  (or  $I_{s1} \gg 0$ ). This can explain why green nodes have a large difference between  $\Psi_M a$  and  $(K_M - K_0)a$ .

Likewise, the Gaussian bending deformation  $\Psi_G a$  is plotted as a function of the Gaussian curvature change  $(K_G - K_0^2)a^2$ , as shown in Fig. 3.10. It is apparent that the values of  $\Psi_G a$  and  $(K_G - K_0^2)a^2$  are quite different for each node. We also mathematically compute the difference between the two variables by following the same assumption used in Eq. (3.10), then we have an expression

$$\Psi_G - (K_G - K_0^2) = \kappa_{11}\kappa_{22} \left( \frac{\lambda_1^2\lambda_2^2 - 1}{\lambda_1^2\lambda_2^2} \right) - 2K_0(K_M - K_0) \approx -2K_0(K_M - K_0). \quad (3.11)$$

We notice that the difference between  $\Psi_G$  and  $(K_G - K_0^2)$  is a function of the mean curvature change  $(K_M - K_0)$  approximately. Generally speaking,  $\Psi_G > (K_G - K_0^2)$  when  $(K_M - K_0) < 0$ , and  $\Psi_G < (K_G - K_0^2)$  when  $(K_M - K_0) > 0$ . The detailed derivation processes of Eq. (3.10) and (3.11) are available in Appendix A.

### 3.3.3 Comparison of bending energy density

As indicated by Eq. (3.2) or (3.9), the bending energy density is linearly correlated to  $2(K_M - K_0)^2$  or  $(2\Psi_M^2 - 0.5\Psi_G)a^2$  by a factor of bending modulus  $M_b$ . For a linear incompressible material, the non-dimensional bending modulus  $M_b/G_s a^2$  is a function of thickness ratio  $\alpha$  inferred from Eq.(2.2), which reads

$$M_b/G_s a^2 = \frac{\alpha^2}{3}. \quad (3.12)$$

Then we have

$$\begin{aligned}
\alpha = 0.01, & \rightarrow M_b/G_s a^2 = 3.33 \times 10^{-5} \\
\alpha = 0.05, & \rightarrow M_b/G_s a^2 = 8.33 \times 10^{-4} \\
\alpha = 0.10, & \rightarrow M_b/G_s a^2 = 3.33 \times 10^{-3}
\end{aligned} \tag{3.13}$$

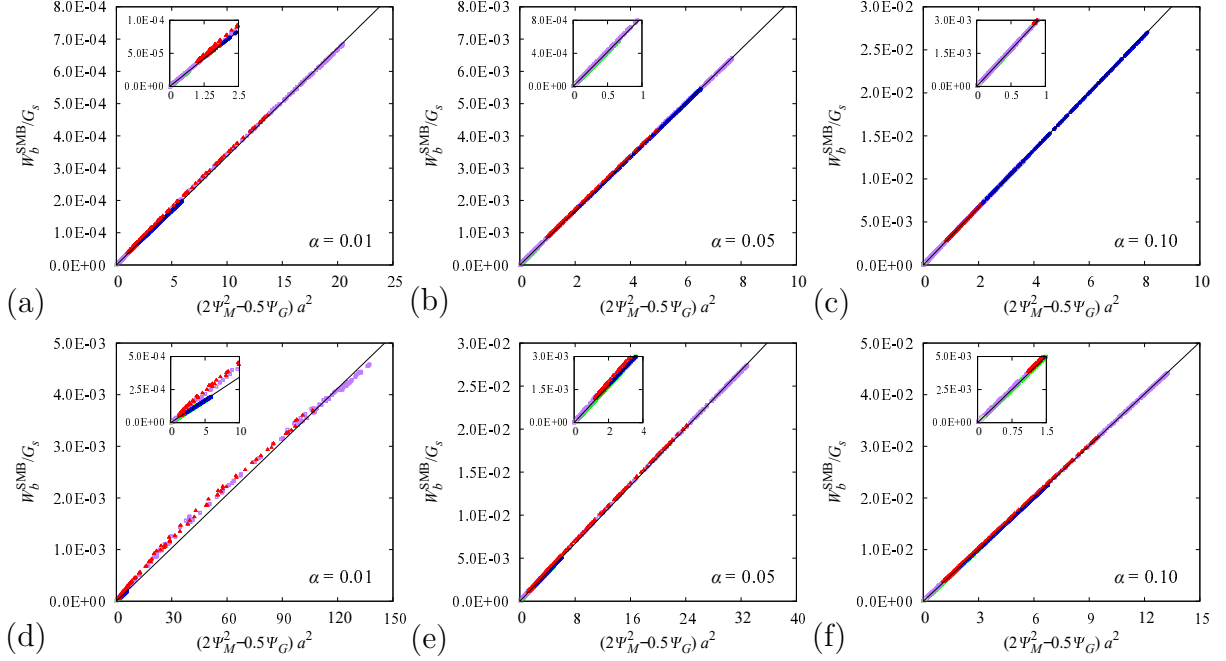


Figure 3.11 – Plots of the bending energy density  $W_b^{\text{SMB}}/G_s$  as a function of  $(2\Psi_M^2 - 0.5\Psi_G)a^2$ . Size ratio  $a/l = 1.0$ . Thickness ratio  $\alpha = 0.01$ ,  $\alpha = 0.05$ , and  $\alpha = 0.10$ . Surface capillary number  $Ca_s = 0.05$  (a,b,c) and  $0.10$  (d,e,f). The straight line represents the equation obtained by linear fitting for all nodes.

$Ca_s = 0.05$	$M_b^{fit}/G_s a^2$	error ( $\pm$ )	$R^2$
$\alpha = 0.01$	$3.36 \times 10^{-5}$	$3.84 \times 10^{-9}$	0.999
$\alpha = 0.05$	$8.36 \times 10^{-4}$	$3.91 \times 10^{-8}$	0.999
$\alpha = 0.10$	$3.34 \times 10^{-3}$	$1.07 \times 10^{-7}$	0.999
$Ca_s = 0.10$	$M_b^{fit}/G_s a^2$	error ( $\pm$ )	$R^2$
$\alpha = 0.01$	$3.44 \times 10^{-5}$	$1.56 \times 10^{-8}$	0.998
$\alpha = 0.05$	$8.39 \times 10^{-4}$	$9.06 \times 10^{-8}$	0.999
$\alpha = 0.10$	$3.53 \times 10^{-3}$	$1.83 \times 10^{-7}$	0.999

Table 3.1 – Results of linear fitting for the correlation between  $W_b^{\text{SMB}}/G_s$  and  $(2\Psi_M^2 - 0.5\Psi_G)a^2$ .  $M_b^{fit}/G_s a^2$  represents the coefficient of the linear equation.

We plot the bending energy density  $W_b^{\text{SMB}}/G_s$  computed by the SMB model as a function of  $(2\Psi_M^2 - 0.5\Psi_G)a^2$ , as shown in Fig. 3.11. (a,b,c) denotes the results of small flow intensity  $Ca_s = 0.05$  and (d,e,f) denotes the results of large flow intensity  $Ca_s = 0.10$ . Three thickness ratios are considered, which are  $\alpha = 0.01$ ,  $0.05$ , and  $0.10$ . It is obvious that  $W_b^{\text{SMB}}/G_s$  is almost a linear function of  $(2\Psi_M^2 - 0.5\Psi_G)a^2$  whatever the flow strength and wall thickness. We use a linear function to correlate the two variables, carried out by Gnuplot using a nonlinear least-squares (NLLS) Marquardt-Levenberg algorithm. The fitting results are shown in Table 3.1. For a given  $\alpha$ , the value of fitting coefficients  $M_b^{\text{fit}}/G_s a^2$  are quite close to the one given in (3.13). It implies that  $(2\Psi_M^2 - 0.5\Psi_G)$  can be used to account for capsule bending behaviors for a given  $M_b$ , and thus Eq. (3.9) is feasible.

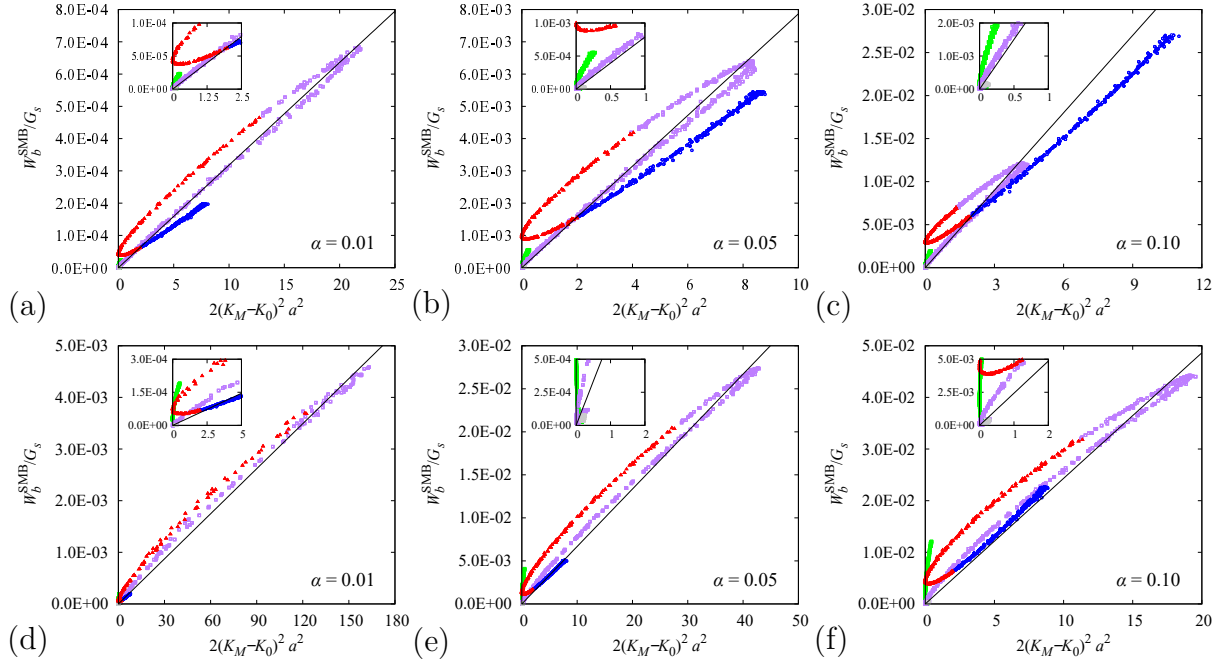


Figure 3.12 – Plots of the bending energy density  $W_b^{\text{SMB}}/G_s$  as a function of  $2(K_M - K_0)^2 a^2$ . Size ratio  $a/l = 1.0$ . Thickness ratio  $\alpha = 0.01$ ,  $\alpha = 0.05$ , and  $\alpha = 0.10$ . Surface capillary number  $Ca_s = 0.05$  (a,b,c) and  $0.10$  (d,e,f). The straight line represents the equation obtained by linear fitting for all nodes.

We also plot  $W_b^{\text{SMB}}/G_s$  as a function of  $2(K_M - K_0)^2 a^2$  for different  $Ca_s$  and  $\alpha$ , as shown in Fig. 3.12. The results of the linear fitting to all nodes are listed in Table 3.2. We can find that  $W_b^{\text{SMB}}/G_s$  and  $2(K_M - K_0)^2 a^2$  do not have a unified linear correlation for all nodes. Only a part of the purple nodes can follow the fitting equation. The blue and green nodes, which occupy most of the capsule nodes, have different bending energy-curvature relationships. It indicates that the Helfrich law defined in Eq. (3.2) is not appropriate to account for the bending resistance of capsules with finite thicknesses.



$Ca_s = 0.05$	$M_b^{fit}/G_s a^2$	error ( $\pm$ )	$R^2$
$\alpha = 0.01$	$3.18 \times 10^{-5}$	$1.67 \times 10^{-8}$	0.998
$\alpha = 0.05$	$7.87 \times 10^{-4}$	$7.33 \times 10^{-7}$	0.992
$\alpha = 0.10$	$3.00 \times 10^{-3}$	$4.17 \times 10^{-6}$	0.980
$Ca_s = 0.10$	$M_b^{fit}/G_s a^2$	error ( $\pm$ )	$R^2$
$\alpha = 0.01$	$2.91 \times 10^{-5}$	$1.99 \times 10^{-8}$	0.996
$\alpha = 0.05$	$6.68 \times 10^{-4}$	$7.83 \times 10^{-7}$	0.989
$\alpha = 0.10$	$2.43 \times 10^{-3}$	$4.46 \times 10^{-6}$	0.970

Table 3.2 – Results of linear fitting for the correlation between  $W_b^{\text{SMB}}/G_s$  and  $2(K_M - K_0)^2 a^2$ .  $M_b^{fit}/G_s a^2$  represents the coefficient of the linear equation.

### 3.4 Discussion

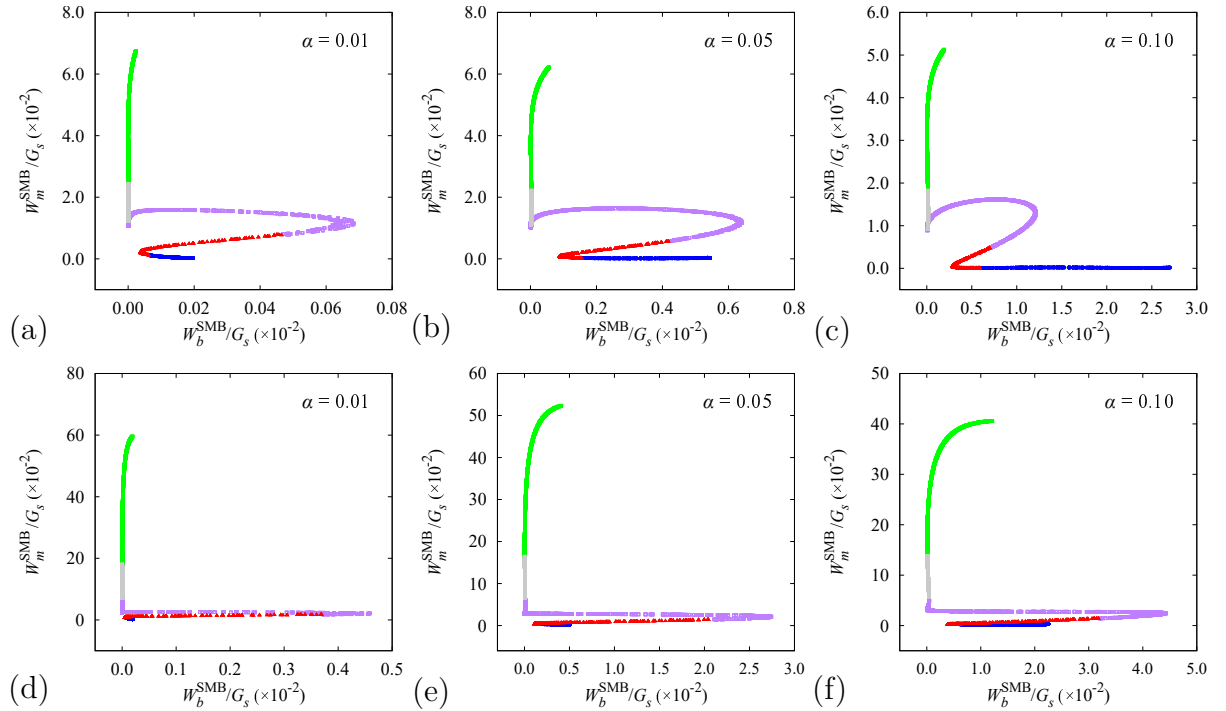


Figure 3.13 – Plots of the membrane energy density  $W_m^{\text{SMB}}/G_s$  as a function of bending energy density  $W_b^{\text{SMB}}/G_s$ . Size ratio  $a/l = 1.0$ . Thickness ratio  $\alpha = 0.01$ ,  $\alpha = 0.05$ , and  $\alpha = 0.10$ . Surface capillary number  $Ca_s = 0.05$  (a,b,c) and  $0.10$  (d,e,f).

We compute the membrane energy density of the SMB model by Eq. (3.3), denoted as  $W_m^{\text{SMB}}$ , and plot  $W_m^{\text{SMB}}/G_s$  as a function of  $W_b^{\text{SMB}}/G_s$  with varying  $Ca_s$  and  $\alpha$ , as shown in Fig. 3.13. For all cases, it shows that the capsule front (green nodes) has a relatively large  $W_m^{\text{SMB}}$ , while  $W_b^{\text{SMB}}$  of those regions are very small. In the concave area,  $W_m^{\text{SMB}}$  always

remains small and near zero, while  $W_b^{\text{SMB}}$  increases with  $\alpha$ . Those phenomena coincide with the fact that the capsule front suffers a small change in curvature and the membrane stretching is dominant; In contrast, the membrane stretching of the capsule concave is small, but the curvature changes in sign in this region. The global bending energy always remains small or even negligible compared to global membrane energy. It implies that the general shape of the deformed capsule is mainly affected by the membrane stretching since the bending effects are small. This might explain why the Helfrich model can predict almost the same capsule overall deformation as the SMB model shown in section 3.1.

### 3.5 Conclusion

In this chapter, we investigate the dynamic behavior of an initially spherical capsule with a finite thickness shell flowing in an infinite parabolic flow. The bulk capillary number  $Ca_v$  and wall thickness ratio  $\alpha$  exert a great influence on the steady-state capsule shape. When capsule typical lengths are plotted as function of a surface capillary number  $Ca_s$ , increasing  $\alpha$  will soften the material, and thus the capsule shape hardly changes with  $\alpha$ . We have also compared the difference between different bending measurements. The bending energy density is a function of the bending deformation  $\Psi$ . However, the correlation between bending energy density and mean curvature change  $K_M - K_0$  cannot satisfy a unified linear function, which indicates that the Helfrich law, although usable in practice, is not appropriate in accounting for the bending resistance of capsules with finite thicknesses.

# Capsule in bounded Poiseuille flow

In this chapter, we use the Shell FEM+BIM model to investigate the motion and deformation of an initially spherical liquid-filled capsule flowing in a straight channel with a circular cross-section, as shown in Fig. 4.1. The undisturbed external flow is assumed as a fully developed Poiseuille flow defined by equation (2.14). The capsule membrane is modeled as a thin shell characterized by a mid-surface and a finite thickness, which have been depicted in section 2.3. We will discuss the effects of flow strength and shell thickness on dynamics of capsules flowing in a confined environment, including the capsule overall deformation and membrane wrinkle formation. Neo-Hookean (NH) constitutive law is used to govern the elastic behavior of the mid-surface. A capsule mesh of 8192 elements ( $\Delta x/a = 0.06$ ) is used unless otherwise specified.

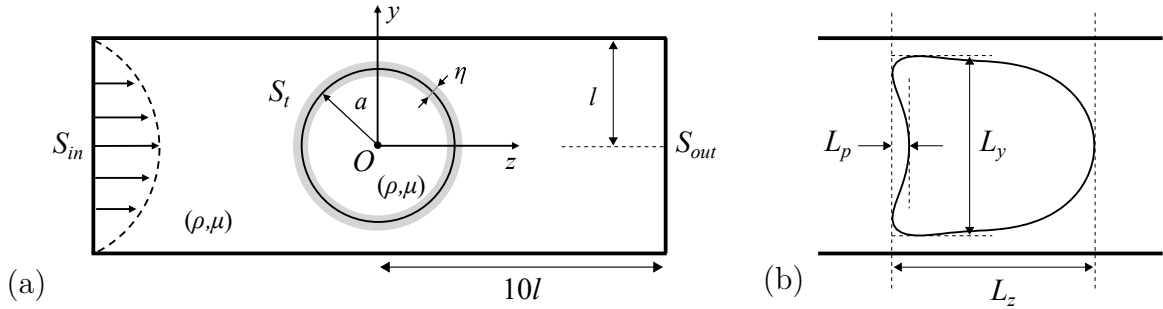


Figure 4.1 – (a) Schematic illustration of an initially spherical capsule with radius  $a$  and finite thickness  $\eta$  subjected to Poiseuille flow in a cylindrical channel with radius  $l$ ; (b) Typical lengths characterizing the capsule deformation.

## 4.1 Application condition

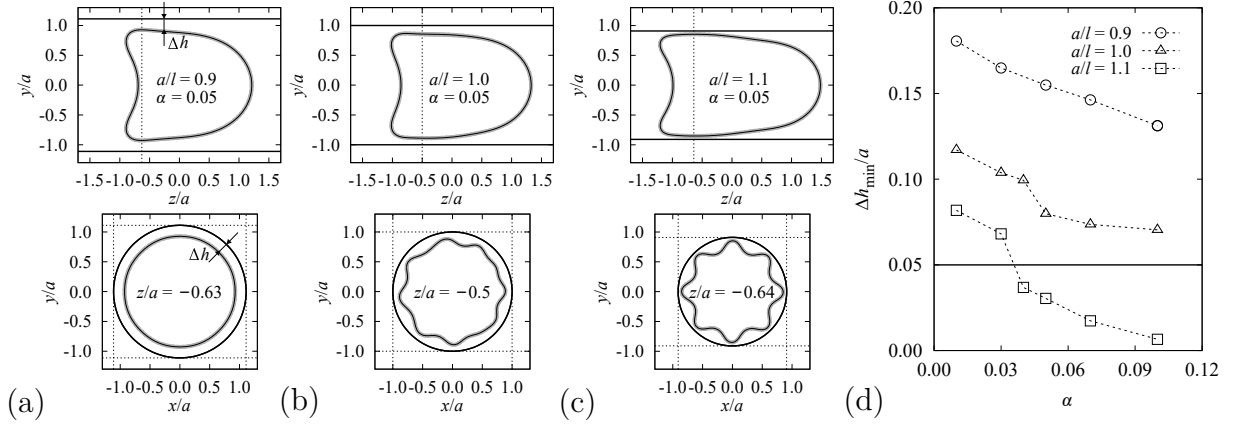


Figure 4.2 – The longitudinal and cross-section profiles for three typical cases with surface capillary number  $Ca_s = 0.05$  and wall thickness ratio  $\alpha = 0.05$ . Size ratios: (a)  $a/l = 0.9$ , (b)  $a/l = 1.0$ , and (c)  $a/l = 1.1$ ; (d) The criterion to determine the validity of the results corresponds to  $\Delta h_{min}/a \geq 0.05$ .

Although the shell FEM assumes the membrane as a 3D material with a finite thickness, the BIM in the fluid part still regards the capsule boundary as a 2D surface. It raises the question whether the shell model is still valid when the thickness of the shell and that of the fluid film between the capsule and the channel are comparable. We consider three typical cases in order to explore this question: initially spherical capsules of  $a/l = 0.9$ , 1.0, and 1.1 (which is fairly large to the channel dimension) are subjected to the external flow with  $Ca_s = 0.05$ . The capsule is pre-deformed into an ellipsoid if  $a/l > 0.9$ . The shell thickness ratio is  $\alpha = 0.05$  and the membrane behavior follows NH law.

Fig. 4.2 (a), (b), and (c) show the longitudinal and cross-section profiles for  $a/l = 0.9$ , 1.0, and 1.1, respectively. Based on the Reissner-Mindlin kinematical assumption, we plot a shell with a constant thickness  $0.05a$  across the mid-surface, represented by a shaded outline. The location of the cross-section profile is cut at the  $z$ -coordinate, where the capsule has a minimum gap  $\Delta h_{min}$  between the outer membrane and the channel. It can be seen that wrinkles are formed in case of full confinement, i.e.,  $a/l \geq 1.0$ . However, we notice that the membrane of  $a/l = 1.1$  is getting too close to the channel wall. Consequently, there is not enough room for the lubricating film, which actually plays an essential role in regulating capsule dynamics. Although the simulation is numerically stable, this case exceeds the feasibility range of the shell model due to the production of results with unclear physical meanings.

In order to avoid having less meaningful results, we plot  $\Delta h_{min}$  as a function of  $\alpha$ , as shown in Fig. 4.2 (d). We set  $\Delta h_{min}/a \geq 0.05$  as a criterion to determine the maximum shell thickness. It is clear that a confinement ratio  $a/l = 1.1$  can only be modeled for

$\alpha \leq 0.03$ , while for  $a/l = 0.9$  and  $1.0$ , all values of  $\alpha$  up to 10% can be modeled. We have noticed that the confinement effects are still considerable for  $a/l = 1.0$ , in which the membrane is highly compressed and exhibits non-symmetric wrinkling shapes. For the sake of accuracy and without losing generality,  $a/l = 0.9$  is employed in the following wrinkle analysis of section 4.5.

## 4.2 Capsule axial deformation

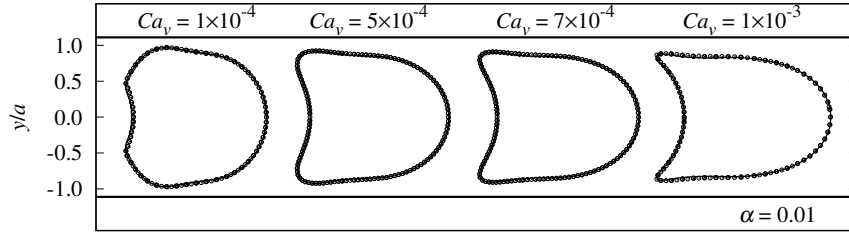


Figure 4.3 – Effect of the bulk capillary number  $Ca_v$  on capsule deformation. Size ratio  $a/l = 0.9$  and wall thickness ratio  $\alpha = 0.01$ .  $Ca_v$  varies from  $1 \times 10^{-4}$  to  $1 \times 10^{-3}$ . Circle dots represents the membrane solution with  $\alpha = 0$  and surface capillary number  $Ca_s = 0.01, 0.05, 0.07$ , and  $0.10$ , respectively. The solid straight line represents the channel wall (same hereinafter).

We begin with investigating the effect of bulk capillary number on capsule deformation in a bounded Poiseuille flow, as shown in Fig. 4.3 for a typical case where  $a/l = 0.9$ . The steady-state profiles in the longitudinal plane are obtained for an initially spherical capsule with  $\alpha = 0.01$ . The bulk capillary number  $Ca_v$  increases from  $1 \times 10^{-4}$  to  $1 \times 10^{-3}$ . It is obvious that capsules exhibit parachute shapes with curvature inversions. Increasing flow intensities, the membrane in the rear is more curved and even has a sharp edge with large curvatures. It illustrates that the capsule deformation increases with  $Ca_v$ . Since the bending resistance of a shell with  $\alpha = 0.01$  is very small, those results are equivalent to ones obtained by a membrane model with  $\alpha = 0$ , as seen in the circle dots, in which a surface capillary number  $Ca_s$  (Eq. 2.6) is employed for a membrane neglecting the thickness. It is worth mentioning that the capsule with a neo-Hookean membrane has stability limits of  $Ca_s$ , beyond which the capsule elongates continuously and has no steady shape (Hu *et al.*, 2013).

Fig. 4.4 shows the steady-state profiles of an initially spherical capsule with  $a/l = 0.9$  and different wall thickness ratios.  $Ca_v = 1 \times 10^{-3}$ , and  $\alpha$  varies from  $0.01$  to  $0.10$ . When  $\alpha = 0.01$ , the capsule presents a fairly large deformation due to the fact that the shell bending resistance is very small and can be neglected. Increasing  $\alpha$  to  $0.02$  and  $0.05$ , the deformation of the capsule gradually decreases with an increasing bending resistance.

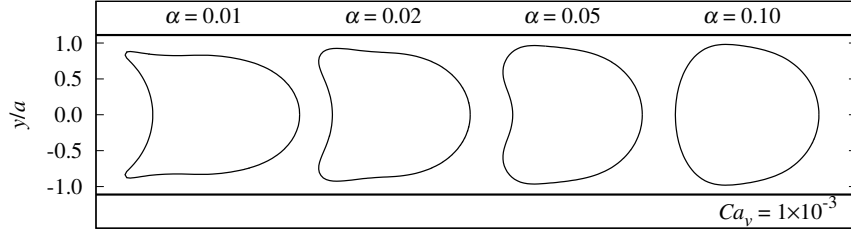


Figure 4.4 – Effect of wall thickness ratio  $\alpha$  on capsule deformation. Size ratio  $a/l = 0.9$  and bulk capillary number  $Ca_v = 1 \times 10^{-3}$ .  $\alpha$  varies from 0.01 to 0.10.

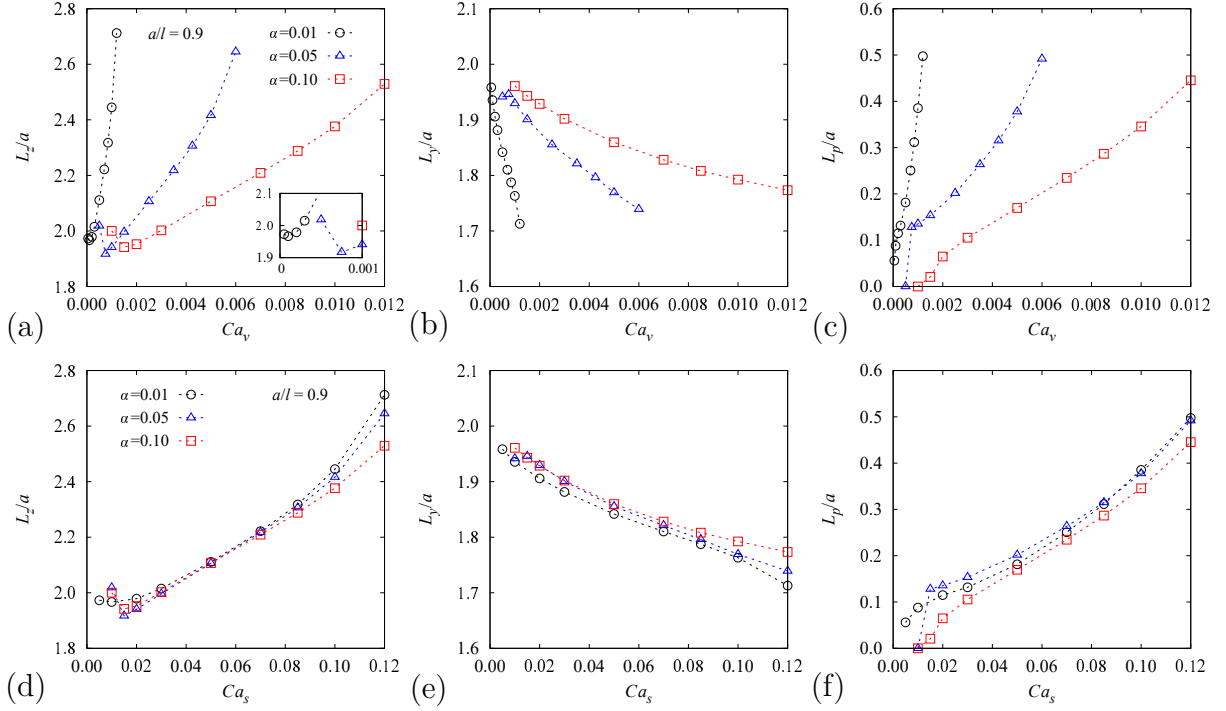


Figure 4.5 – Plots of the capsule typical dimensions as a function of  $Ca_v$  (a, b, c) and  $Ca_s$  (d, e, f).  $a/l = 0.9$ , and  $\alpha = 0.01, 0.05$ , and  $0.10$ . The typical dimensions are axial length  $L_z$ , width  $L_y$ , and parachute depth  $L_p$ .

When the membrane is relatively thick ( $\alpha = 0.10$ ), the bending rigidity greatly restricts the capsule deformation so that the parachute shape cannot form in the back. The results show that in addition to the flow strength, the membrane thickness is also a significant parameter that affects and regulates the deformation of the capsule.

As shown in Fig. 4.1 (b), we use three typical dimensions, axial length  $L_z$ , width  $L_y$ , and parachute depth  $L_p$ , to measure the capsule deformation. The plots in Fig. 4.5 (a, b, c) give the evolution of the three lengths with the shell thickness ratio  $\alpha$  and the bulk capillary number  $Ca_v$ . The first impression is that the shell thickness greatly influences the deformed capsule shapes. For the same  $L_z$ , a larger thickness corresponds to a higher flow strength. When reducing  $\alpha$ , the applicable  $Ca_v$  is also limited to a small range, which illustrates that the bending rigidity can effectively resist the viscous force imposed by

external fluids. For a given  $\alpha$ ,  $L_z$  firstly decreases and then increases due to the parachute formation. A critical value  $Ca_v^c$  is thus obtained at which  $L_p$  starts to be non-zero. It is apparent that  $Ca_v^c$  increases with  $\alpha$ , which also reflects the effect of bending resistance. Besides,  $L_y$  decreases with  $Ca_v$  because of the channel confinement.

If one plots the deformation as a function of the surface capillary number  $Ca_s$ , as shown in Fig. 4.5 (d, e, f), the curves are almost overlapping for a flow strength range of  $0.03 \leq Ca_s \leq 0.09$ , at which the value of typical length for different  $\alpha$  is difficult to be discriminated. It indicates that the capsule deformation in this flow section depends only on the surface capillary number and the bending resistance has a negligible effect on the overall deformed profile. This result is similar to the one from Dupont *et al.* (2015), who have concluded that the stretching of the mid-surface is the prevailing phenomenon based on the study of the effect of bending resistance on capsule deformation in simple shear flow. When  $Ca_s$  is smaller than 0.03 and larger than 0.09, capsule typical lengths have apparent differences for different  $\alpha$ . However, the results of Dupont *et al.* (2015) indicate that  $\alpha$  always has a negligible effect whatever the value of  $Ca_s$ .

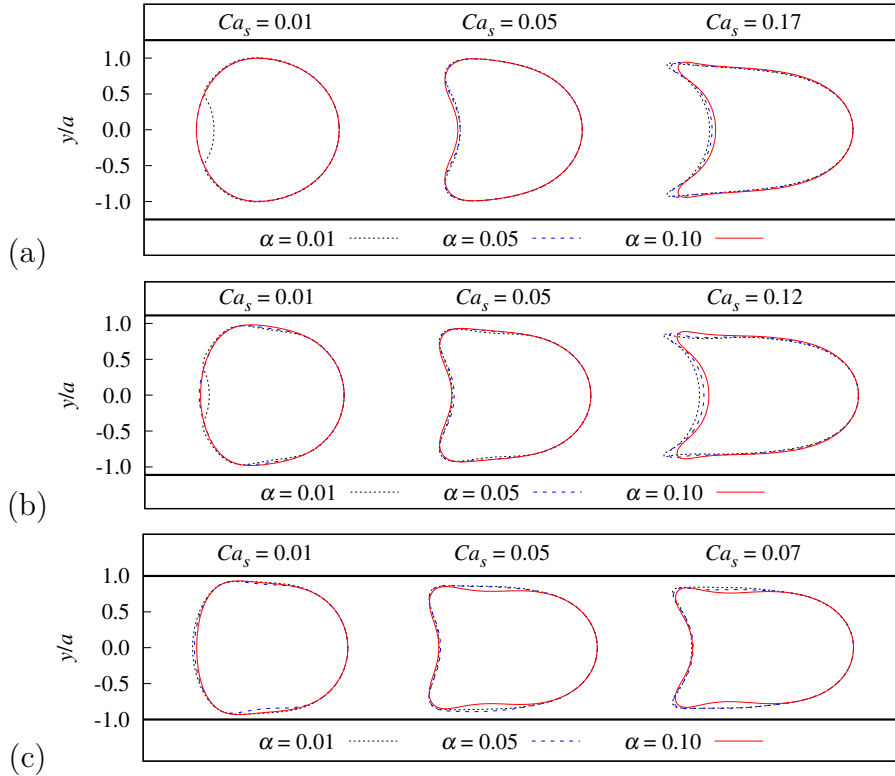


Figure 4.6 – Effect of wall thickness ratio  $\alpha$  and surface capillary number  $Ca_s$  on the longitudinal capsule profile. (a)  $a/l = 0.8$ ; (b)  $a/l = 0.9$ ; (c)  $a/l = 1.0$ .

For the sake of illustrating the above phenomenon, we plot the longitudinal profiles of different  $\alpha$  under a given  $Ca_s$ , as shown in Fig. 4.6 (b). For a moderate flow strength with  $Ca_s = 0.05$ , the profiles of different  $\alpha$  almost superimpose indeed. Under a small

flow strength with  $Ca_s = 0.01$ , the profile of  $\alpha = 0.05$  and  $0.10$  are still very near and no curvature inversion on the shape, while  $\alpha = 0.01$  generates a small concave in the rear due to its negligible bending resistance. When the flow strength is extremely high, e.g.,  $Ca_s = 0.12$ ,  $\alpha = 0.01$  predicts a contour with unrealistic pointed-ends, and the model is almost reaches the stability limit. However, this issue does not occur for  $\alpha = 0.05$  and  $0.10$  because of an increased wall thickness and bending resistance.

For a given capsule size, if we use  $Ca_s$  instead of  $Ca_v$  to represent the flow strength, increasing the thickness will implicitly decrease the bulk shear modulus  $G$  (inferred from Eq. 2.6) to obtain the same value of  $Ca_s$ . This means that a larger  $\alpha$  leads to a softer material, which is probably the reason why we observe almost no effect of thickness on typical lengths under a moderate flow strength of  $0.03 \leq Ca_s \leq 0.09$ , shown in Fig. 4.5 (d, e, f). When the flow strength is low, capsules with a very thin wall will produce a small parachute shape with curvature inversions. For an extreme flow strength, capsules with a thick wall will prevent the formation of pointed-ends in the rear of the membrane. Under the above two flow conditions, the capsule deformation will be significantly different with the change of the membrane thickness. This indicates that if one wants to fully understand the influence of wall bending resistance on capsule dynamics, it is necessary to employ a Poiseuille flow where the capsule exhibits a curvature reversal shape.

### 4.3 Effect of capsule size

The steady-state longitudinal capsule contours for size ratios  $a/l = 0.8$  and  $1.0$  under different  $\alpha$  and  $Ca_s$  are shown in Fig. 4.6 (a) and (c). We again observe that capsule profiles for different  $\alpha$  are very near under a moderate flow strength of  $Ca_s = 0.05$ . For  $Ca_s = 0.01$  and  $a/l = 0.8$ , the capsule with  $\alpha = 0.01$  has a small concave, while the profiles of  $\alpha = 0.05$  and  $0.10$  are almost the same, and both ends are convex. For  $Ca_s = 0.01$  and  $a/l = 1.0$ , the capsule profiles are very near and no curvature reversal shapes for different  $\alpha$ . For an extreme flow strength, i.e.,  $Ca_s = 0.17$  for  $a/l = 0.8$  and  $Ca_s = 0.07$  for  $a/l = 1.0$ , unrealistic pointed-ends in the rear are predicted in the contour of  $\alpha = 0.01$ , while it does not occur when  $\alpha = 0.05$  and  $0.10$  due to an increased wall thickness and bending resistance.

We plot the capsule typical dimensions,  $L_z$ ,  $L_y$ , and  $L_p$ , as a function of  $Ca_s$  when  $a/l = 0.8$  and  $1.0$ , as shown in Fig. 4.7. For  $a/l = 0.8$  (a, b, c), the deformation characteristics are similar to that of  $a/l = 0.9$ , i.e., the capsule deformations of different  $\alpha$  are distinguishable for high flow strengths of  $Ca_s \geq 0.12$ . For  $a/l = 1.0$  (d, e, f), the extreme flow strength is limited to  $Ca_s = 0.07$  due to full channel confinement, under which the capsule deformations of different  $\alpha$  are always very close. When  $Ca_s = 0.03$ ,  $L_y$



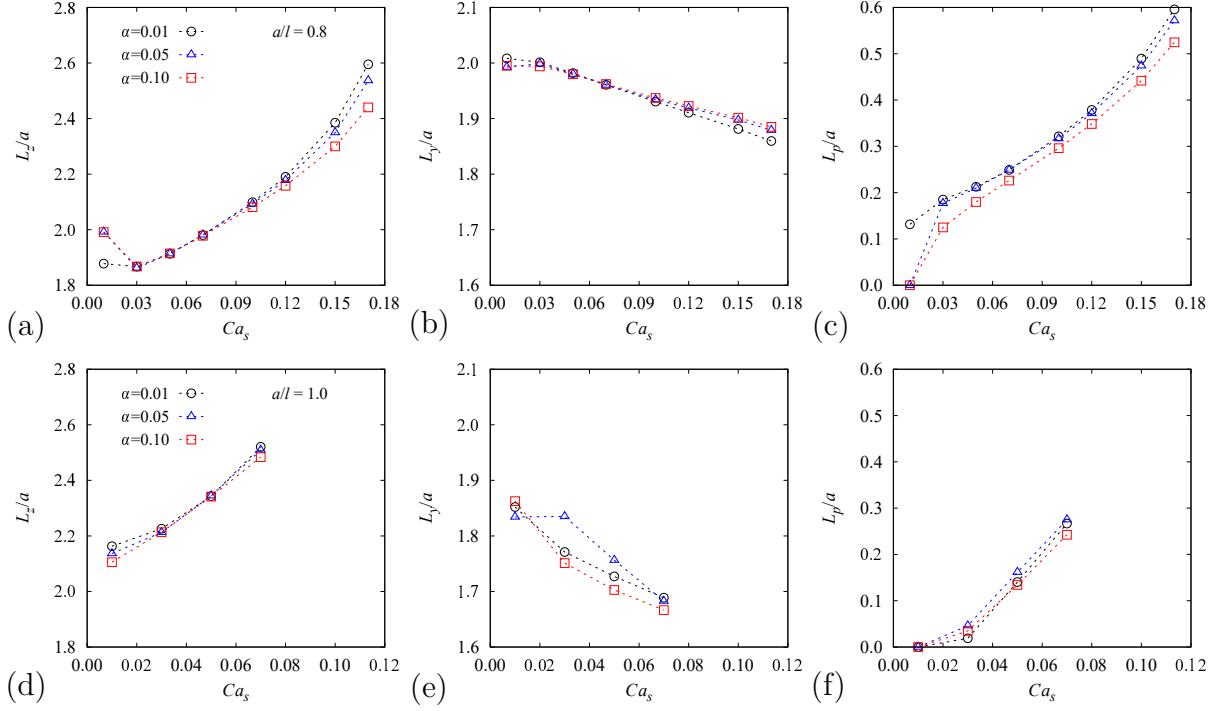


Figure 4.7 – Plots of the capsule typical dimensions  $L_z$ ,  $L_y$ , and  $L_p$  as a function of  $Ca_s$ .  $\alpha = 0.01, 0.05$ , and  $0.10$ . (a, b, c):  $a/l = 0.8$ ; (d, e, f):  $a/l = 1.0$ .

of  $\alpha = 0.05$  is apparently higher than that of  $\alpha = 0.01$  and  $0.10$ . The difference is caused by the fact that the cross-plane may go through wrinkles' peak or valley for different  $\alpha$ . It should be aware that the limiting  $Ca_s$  decreases with size ratios, which coincides with the study of Hu *et al.* (2013).

## 4.4 Capsule typical curvature

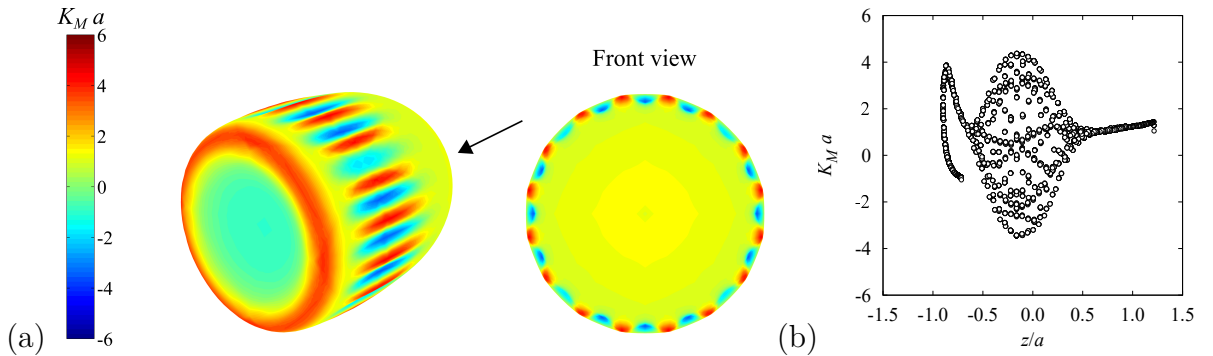


Figure 4.8 – The mean curvature  $K_M$  of each node of a steady-state deformed capsule: (a) on the mid-surface; (b) along the flow direction  $z$ . The case considered is  $a/l = 0.9$ ,  $\alpha = 0.01$ , and  $Ca_s = 0.05$ .

The distribution of the mean curvature  $K_M$  (defined by Eq. 2.29) on the steady-state

capsule surface is shown in Fig. 4.8 (a), where  $a/l = 0.9$ ,  $\alpha = 0.01$ , and  $Ca_s = 0.05$ . We firstly notice that the alternating positive and negative curvature appears on the capsule side, due to the formation of wrinkles with crests and troughs. Besides, the capsule forms a concave parachute shape under the viscous force, which leads to the curvature inversion in the rear and a ring-shaped area with relatively high curvatures. Fig. 4.8 (b) shows the plot of  $K_M$  as a function of coordinates  $z$ . It clearly shows that the rear bending area undergoes a significant curvature change. The high curvature in the rear also implies that the capsule membrane has a great risk of rupture (Chang & Olbricht, 1993b; Joung *et al.*, 2020).

Noting that  $K_M^r$  is the mean curvature of 3D capsule shapes, while from the experimental point of view, it is more appropriate to compute the meridional curvature of the capsule profile in longitudinal plane. The meridional curvature  $K_\varphi$  is given by

$$K_\varphi = \frac{|\sigma''|}{(1 + \sigma'^2)^{3/2}}, \quad (4.1)$$

where  $\sigma$  denotes the distance from the flow axis.  $\sigma' = d\sigma/ds$ , and  $s$  represents the arc length measured along the contour of the membrane in the meridional plane.

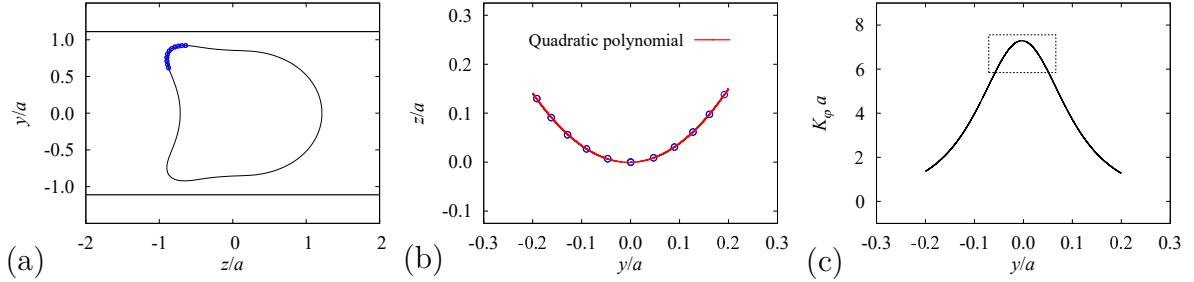


Figure 4.9 – Measurements of meridional curvatures. The case considered is  $a/l = 0.9$ ,  $\alpha = 0.01$ , and  $Ca_s = 0.05$ . (a) Extracting nodes from longitudinal profile; (b) Quadratic polynomial fitting for the extracted nodes; (c) Meridional curvatures  $K_\varphi a$  of the parabola.

For the longitudinal profile of  $a/l = 0.9$ ,  $\alpha = 0.01$ , and  $Ca_s = 0.05$  shown in Fig. 4.9 (a), we extract the nodes (9 ~ 11 for all cases hereinafter) that cover one of the rear ends. We move and rotate those discrete points to make them symmetric with respect to the  $z$ -axis, and perform a quadratic polynomial fitting with function  $z = a_1 y^2 + a_2 y + a_3$  for those points. A parabola shown in Fig. 4.9 (b) is fitted by adjusting the rotating angle to obtain the highest correlation coefficient  $R^2$ . The meridional curvature  $K_\varphi a$  of the parabola is then computed by Eq. (4.1) and plotted in Fig. 4.9 (c), where the maximum curvature is denoted as  $K_\varphi^{max} a$ , and the adjacent curvatures larger than  $0.8K_\varphi^{max} a$  (as shown in the box in Fig. 4.9 c) are extracted and averaged. We denote  $K_\varphi^r a$ , the typical curvature in the rear bending area of capsule contour in the meridional plane. Finally,

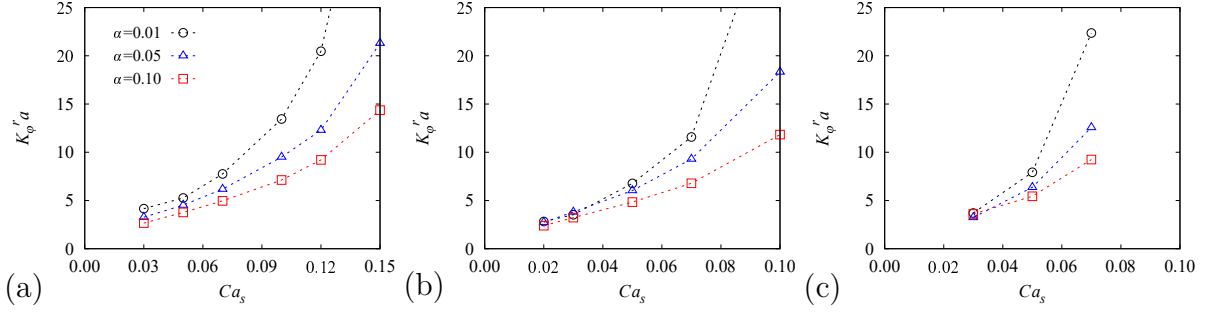


Figure 4.10 – Typical meridional curvature  $K_\varphi^r a$  is plotted as a function of  $Ca_s$ .  $\alpha = 0.01$ , 0.05, and 0.10. (a)  $a/l = 0.8$ ; (b)  $a/l = 0.9$ ; (c)  $a/l = 1.0$

$K_\varphi^r a$  is computed under different  $Ca_s$  and  $\alpha$  for  $a/l = 0.8, 0.9$ , and  $1.0$ , as shown in Fig. 4.10. For all cases,  $R^2 > 0.99$  and  $K_\varphi^r / K_\varphi^{max} \approx 92.8\%$ .

For each capsule size,  $K_\varphi^r a$  increase with  $Ca_s$  under a given wall thickness ratio. When the flow intensity is small, e.g.,  $Ca_s = 0.03$ , there are small differences of  $K_\varphi^r a$  for different  $\alpha$ . For high flow intensities,  $K_\varphi^r a$  increases with decreasing  $\alpha$ , which indicates that the rear bending area is more buckled for a small membrane bending resistance. It is obvious that large values of  $Ca_s$  lead to a meaningful effect of thickness on the distinguishing of  $K_\varphi^r a$ . When  $Ca_s = 0.15$  for  $a/l = 0.8$  and  $Ca_s = 0.12$  for  $a/l = 0.9$ , the high flow intensity causes a pointed-ends as shown in profiles of Fig. 4.6, and thus  $K_\varphi^r a$  is extremely large and difficult to be measured.

In section 4.2, measuring typical lengths to fulfill the purpose of discriminating  $\alpha$  of a given capsule size is difficult since the capsule axial deformation of different  $\alpha$  is only distinguishable for extremely high  $Ca_s$ . However, Fig. 4.10 indicates that the typical curvature  $K_\varphi^r a$  easily exhibits apparent differences for different  $\alpha$  under a wide range of  $Ca_s$ . This feature can help to deduce the realistic membrane thickness by measuring the typical rear curvature in practice.

## 4.5 Membrane wrinkle

Fig. 4.8 (a) has shown regular wrinkles formed on the capsule side. In order to measure the capsule geometric shape effectively, we take a cross-section at the middle of the wrinkling area, as shown in Fig. 4.11 (a). (The cross-section plane is always taken at the middle of the wrinkling area hereinafter.)  $R_m$  denotes the mean radius of all intersections. We adopt the measuring strategy of Dupont *et al.* (2015): In terms of polar coordinates  $(\rho, \theta)$ , we compute the arc length  $s$  along  $R_m$  starting at  $\theta = 0$  for each intersection. The corresponding radius difference  $\Delta\rho$  between mid-surface and  $R_m$  is plotted as a function of  $s$  shown in Fig. 4.11 (b). It should be aware that the wavelength and amplitude in Fig. 4.11 (b) may depend on mesh size. For the mesh of 8192 elements with  $\Delta x/a = 0.06$ , each

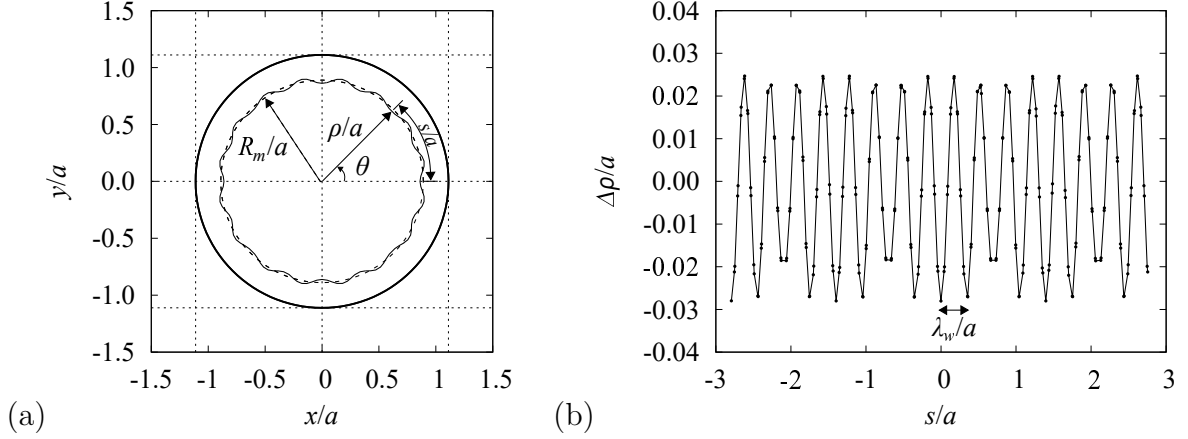


Figure 4.11 – Measurements of the wrinkles of a steady-state deformed capsule. The case considered is  $a/l = 0.9$ ,  $\alpha = 0.01$ , and  $Ca_s = 0.05$ . (a) Capsule mid-surface profile in the  $xy$ -plane.  $\rho$  is the radius of each intersection.  $R_m$  is the mean radius of all intersections; (b) The radius difference  $\Delta\rho$  between the mid-surface and mean radius is plotted as a function of the arc length  $s$  measured in a polar coordinate system  $(\rho, \theta)$ . The dots represent intersections between the cross-plane and the grids.

wave is governed by more than 14 intersections, which is enough to determine a wavelength indicated by Dupont *et al.* (2015). We compute the mean value for all wavelengths and amplitudes, denoted by  $\lambda_w$  and  $A$ , respectively. The standard deviation of the discrete value relative to the mean value is also given. For the cross-profile shown in Fig. 4.11 (a),  $\lambda_w/a = 0.35 \pm 0.02$  and  $A/a = 0.048 \pm 0.005$ .

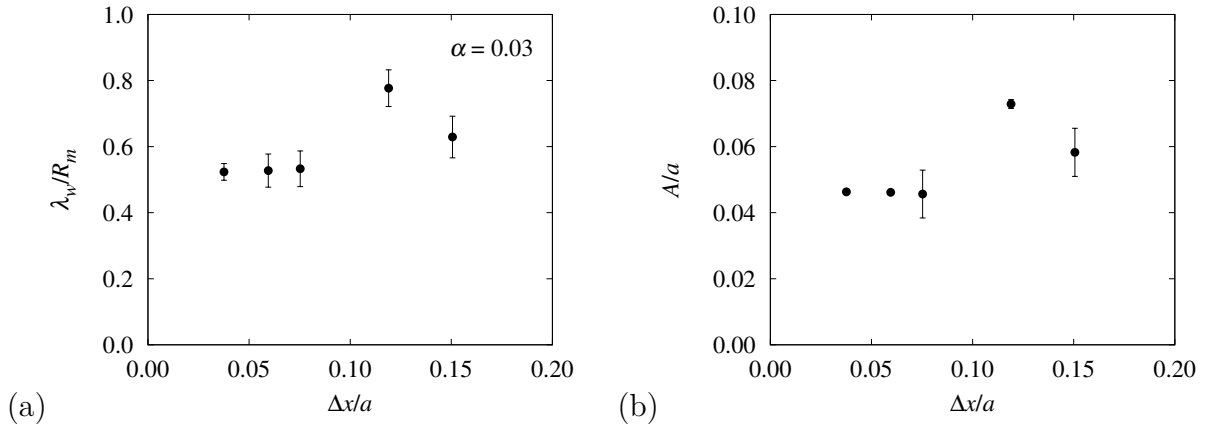


Figure 4.12 – Influence of the mesh size  $\Delta x$  on (a) the wrinkle wavelength  $\lambda_w/R_m$  and on (b) the wrinkle amplitude  $A/a$ .  $\alpha = 0.03$  for a capsule with  $a/l = 0.9$ , and  $Ca_s = 0.05$ .

In order to verify the influence of mesh size on the wrinkle geometry, we perform a convergence study on the results of wavelength and amplitude under various capsule meshes, as shown in Fig. 4.12, where  $\alpha = 0.03$  and  $Ca_s = 0.05$ . The error bar represents the standard deviation. Information on the mesh size can be found in Table 2.1.  $\lambda_w$  is

non-dimensionalized by  $R_m$ , denoted by  $\lambda_w/R_m$ , because we have found that this parameter keeps constant for different locations of the cross-section plane. For a coarse mesh with  $\Delta x/a \geq 0.12$ , the values of  $\lambda_w/R_m$  and  $A/a$  have a large oscillation with varying  $\Delta x$ . However, when  $\Delta x/a \leq 0.08$ ,  $\lambda_w/R_m$  and  $A/a$  tend towards constant values, and the standard deviation also decreases with refining the mesh size. We notice that the differences between 8192 and 20480 elements are less than  $4.0 \times 10^{-3}$  for  $\lambda_w/R_m$  and less than  $1.5 \times 10^{-4}$  for  $A/a$ . Both of them are smaller than the corresponding errors.

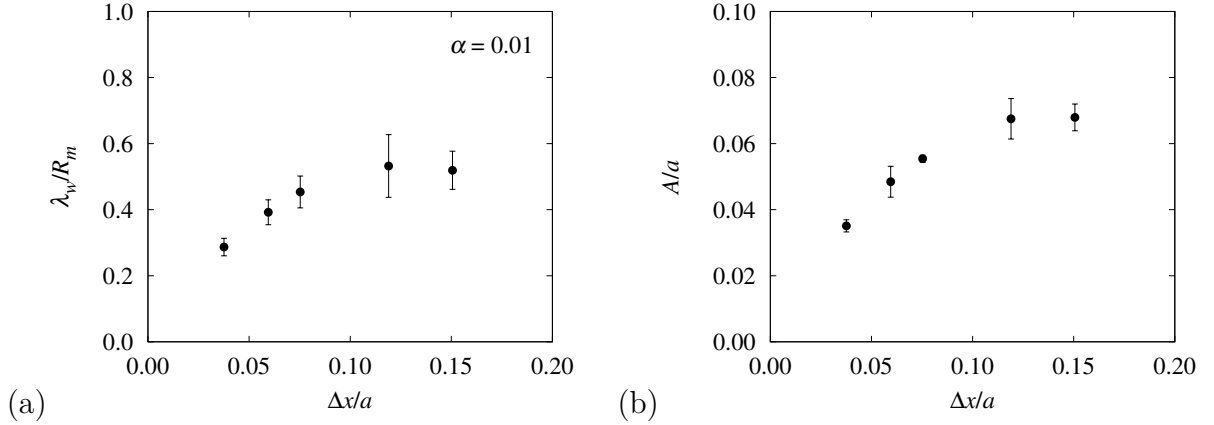


Figure 4.13 – Influence of the mesh size  $\Delta x$  on (a) the wrinkle wavelength  $\lambda_w/R_m$  and on (b) the wrinkle amplitude  $A/a$ .  $\alpha = 0.01$  for a capsule with  $a/l = 0.9$ , and  $Ca_s = 0.05$ .

We consider another capsule with a very thin shell of  $\alpha = 0.01$  subjected to the same flow with  $Ca_s = 0.05$ . The corresponding  $\lambda_w/R_m$  and  $A/a$  under different mesh sizes are shown in Fig. 4.13. It shows that both  $\lambda_w/R_m$  and  $A/a$  decrease with  $\Delta x/a$ , implying no convergence of the solution with regard to the mesh. As we know, the wrinkling phenomenon is essentially a manifestation of structural instability due to negative tensions (Hu *et al.*, 2012). The membrane of  $\alpha = 0.01$  has a negligible bending rigidity that contributes a little to resist the production of negative tensions. Consequently, the physical buckling wavelength is probably influenced by mesh size for a very small  $\alpha$ .

The above results imply that a very refined mesh ( $N_E = 20480$ ) should be employed for  $\alpha = 0.01$  due to small bending resistance. However, for a thicker shell with  $\alpha > 0.01$ , wrinkles can be predicted adequately by a mesh of  $N_E = 8192$ . In order to eliminate the impact of potential numerical influences, the results in the following are obtained by considering a capsule mesh with 20480 elements ( $\Delta x/a = 0.038$ ) in all cases.

The influence of  $\alpha$  on  $\lambda_w/R_m$  and  $A/a$  is shown in Fig. 4.14, where  $\alpha$  varies from 0.01 to 0.07 and  $Ca_s$  varies from 0.05 to 0.12. For shells with  $\alpha > 0.04$ , only a high flow strength can lead to wrinkle formations. Since the shell with  $\alpha = 0.10$  is too thick, no wrinkle is generated even with a very high flow strength. For a given  $Ca_s$  and increasing  $\alpha$ ,  $\lambda_w/R_m$  continually increases, while  $A/a$  firstly increases and then decreases. However,

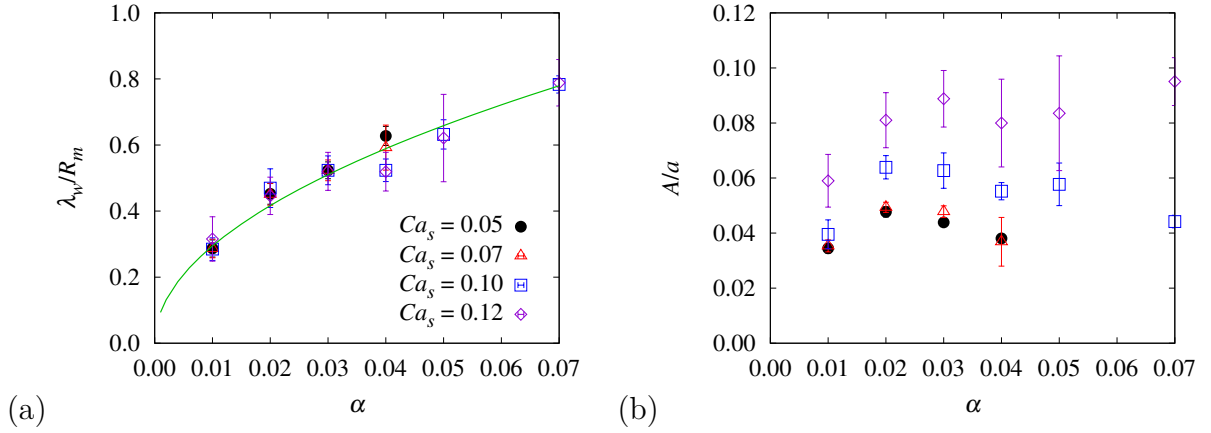


Figure 4.14 – Influence of the shell thickness ratio  $\alpha$  on (a) the wrinkle wavelength  $\lambda_w/R_m$  and (b) the wrinkle amplitude  $A/a$  for different values of  $Ca_s$ . The considered capsule size  $a/l = 0.9$ . The green curve represents the numerical fitting curve to all points.

for a given  $\alpha$  and increasing  $Ca_s$ ,  $A/a$  increases accordingly, while  $\lambda_w/R_m$  hardly changes with  $Ca_s$ . It indicates that the wrinkle wavelength is independent of the external viscous forces, while it depends only on the bending resistance or shell thickness. This feature of  $\alpha$ -dependent wrinkle formation is consistent with the research of Dupont *et al.* (2015), who have investigated the effect of capsule bending resistance in simple shear flow.

The correlation between wavelength and wall thickness for a given material has been studied experimentally and numerically. Cerda & Mahadevan (2003) stretched a thin homogeneous membrane between two clamped ends. They found that the non-dimensional wavelength of wrinkles forming on the sheet is a function of the thickness ratio, written by  $2.9\sqrt{\alpha}$ . Dupont *et al.* (2015) numerically investigated the wrinkle formation for a spherical capsule with neo-Hookean membrane in simple shear flow. The fitting result shows that the dimensionless wavelength can be represented by  $2.5\sqrt{\alpha}$ . However, the deformed capsule in shear flow exhibits non-uniform wrinkles distributed on the entire circumference, which leads to potential errors in wavelength measuring.

As for the numerical predictions in Fig. 4.14, we correlate the wavelength to the wall thickness ratio by a power function with a 0.5 exponent, which is carried out by Gnuplot using a nonlinear least-squares (NLLS) Marquardt-Levenberg algorithm, as follows,

$$\lambda_w/R_m = 2.95\sqrt{\alpha}, \quad (4.2)$$

with a correlation coefficient  $R^2 = 0.95$  and a fitting error  $\pm 0.04$ , as seen the green curve in Fig. 4.14. It is encouraging that the fitting law coincides very well with the one obtained by Cerda & Mahadevan (2003), which implies that the wrinkling mechanism is probably universal whatever the boundary conditions. This result is essential since it can help to determine the realistic membrane thickness.

## 4.6 Experimental observation

Microcapsules are fabricated by Adlan Merlo based on the method of interfacial polymerization with cross-linking reactions (Edwards-Lévy *et al.*, 1993). In brief, 1 ml aqueous solution of 10% (w/v) ovalbumin (Sigma) with a phosphate buffer (pH 7.4, Sigma) is prepared, which is then dispersed in 10 ml vegetable oil (ISIO 4, Lesieur) at a stirring speed of 2400 rpm to form the droplets. Next, 10 ml vegetable oil with 2.5% (w/v) terephthaloyl chloride (TC, Sigma) is added to the emulsion, and the membrane is thus formed by cross-linking reactions at the interface of the droplets. The reaction is stopped by dilution of the reaction medium. After stirring 15 min, microcapsules are separated, washed and finally resuspended in an aqueous glycerin solution.

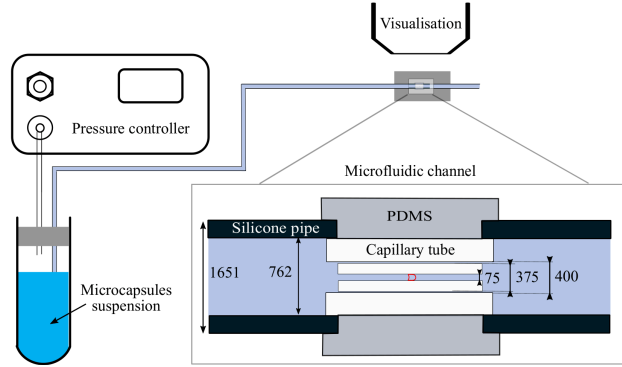


Figure 4.15 – Microfluidic set-up. All lengths are in  $\mu\text{m}$ .

Fig. 4.15 shows the schematic of the microfluidic flow system used by Adlan Merlo to perform all the experiments. A straight 28-mm-long cylindrical capillary tube with a diameter of  $2l = 75\mu\text{m}$  is embedded in another tube, immersed in polydimethylsiloxane (PDMS Sylgard 184, Dow Corning) to remove optical distortions (Lefebvre *et al.*, 2008). The system is mounted on a DMI8 microscope (Leica), and the observation field is far enough away from the entrance to ensure that the deformed capsule has reached its steady-state. With a viscosity of  $\mu = 0.92 \text{ Pa s}$  at  $20^\circ\text{C}$ , the capsule suspension is injected into the microchannel through a pressure controller (EZ-Flow, Fluigent) with values ranging from 800 mbar to 1500 mbar, leading to capsule velocities from 0.8 to 6 mm/s. Images are recorded by a high-speed camera (Fastcam MINI AX50, Photron) with a calibration scale of  $0.694 \mu\text{m}/\text{pixel}$ .

Fig. 4.16 shows four deformed capsule images where prominent wrinkles can be observed on the membrane surface. In order to infer the radius of the initial sphere, the capsule contours are manually extracted from the experimental images using ImageJ (NIH, USA). The middle of the dark contour line is considered as the borderline for capsule mid-surface and channel wall. Assuming that the deformed capsule has a quasi-axisymmetric

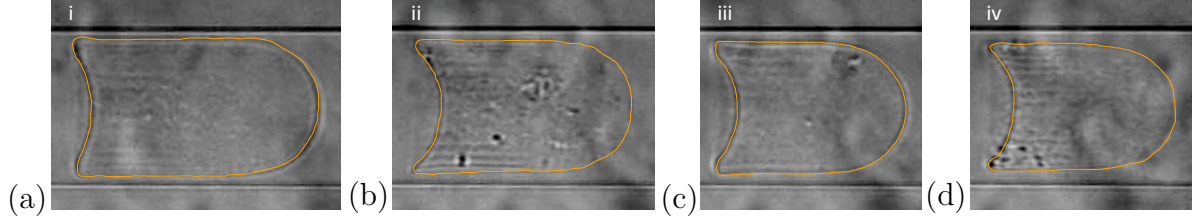


Figure 4.16 – Experimental image of the capsule in a cylindrical channel with extracted contour (full line). The error of approximate initial radius  $a^{exp}/l$  is of order  $\pm 2\%$  corresponding to  $\pm 1$ -pixel uncertainty during contour extraction. (a)  $a^{exp}/l = 1.14$ ; (b)  $a^{exp}/l = 1.08$ ; (c)  $a^{exp}/l = 1.01$ ; (d)  $a^{exp}/l = 0.98$ .

shape with volume  $V^{exp}$  when it flows along the center of the cylindrical tube, the approximate initial radius  $a^{exp}$  is computed by  $a^{exp} = (3V^{exp}/4\pi)^{1/3}$ . We consider the uncertainty of  $\pm 1$ -pixel during contour extractions, which can give rise to an error of order  $\pm 2\%$  on the approximate size ratio  $a^{exp}/l$ .

## 4.7 Identification of membrane thickness

A classical way for measuring capsule membrane thickness employs electronic microscopy after a dehydration step of the capsule (Brown *et al.*, 2003), which often affects the membrane dimensions compared to the wet state. Thus indirect measurements for determining membrane thickness in real suspension become a necessity.

### 4.7.1 Wrinkle measurement

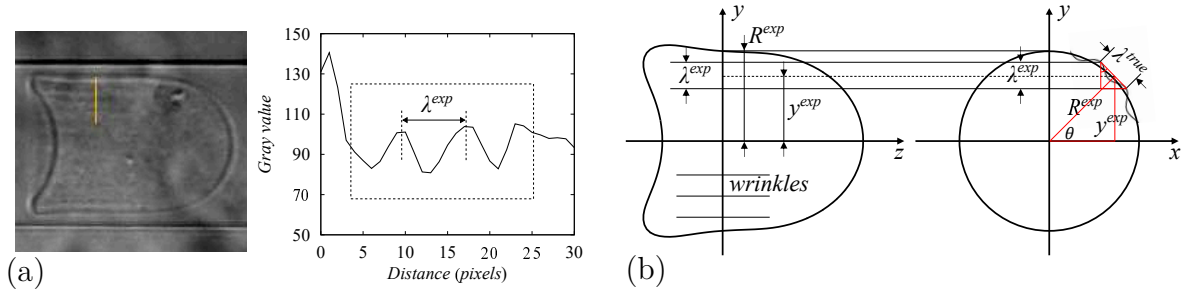


Figure 4.17 – Measurement of wrinkle wavelength from the experimental image.

The peaks and valleys of the capsule wrinkles are presented as light and dark stripes shown in the experimental image. Therefore, we can measure the wavelength of the capsule wrinkles according to the gray value of the image by ImageJ. Fig. 4.17 (a) shows the variation in the gray value along a given straight line segment. The distance of the adjacent crests or troughs shown in the box is regarded as the wrinkle wavelength, denoted by  $\lambda^{exp}$ . However, considering that the natural capsule membrane is a curved surface, the



stripes observed in the image are the projections of the curved wrinkles onto the plane of view. As a result,  $\lambda^{exp}$  must also be regarded as one component of the spatial wrinkle wavelength. Fig. 4.17 (b) illustrates the geometrical relationship between  $\lambda^{exp}$  and the spatial wavelength  $\lambda^{true}$ . In order to non-dimensionalize  $\lambda^{true}$  by the local radius  $R^{exp}$ , we also measure the length  $y^{exp}$  that in between the axis and middle of  $\lambda^{exp}$ . Then  $\lambda^{true}/R^{exp}$  is defined by

$$\lambda^{true}/R^{exp} = \frac{\lambda^{exp}}{\sqrt{R^{exp2} - y^{exp2}}} \quad (4.3)$$

For each capsule shown in Fig. 4.16, we seek all evident and distinguishable  $\lambda^{exp}$  from the area with distinct light and dark stripes, as shown in the box in Fig. 4.17 (a). The corresponding non-dimensional wavelengths  $\lambda^{true}/R^{exp}$  are then computed and averaged. Table 4.1 lists the values of  $\lambda^{true}/R^{exp}$  and initial radius  $a$  for each capsule.

	Capsule i	Capsule ii	Capsule iii	Capsule iv
$\lambda^{true}/R^{exp}$	0.187	0.186	0.223	0.165
$a^{exp}$ ( $\mu\text{m}$ )	42.65	40.33	37.76	36.64

Table 4.1 – Value of non-dimensional wrinkle wavelength  $\lambda^{true}/R^{exp}$  and initial radius  $a$  for ovalbumin capsules i-iv.

Knowing capsules' initial radius  $a^{exp}$  and wrinkle wavelength  $\lambda^{true}/R^{exp}$  listed in Table 4.1, the thickness ratio  $\alpha$  and membrane thickness  $\eta$  for experimental capsules i-iv can be estimated from Eq. (4.2) and (2.3). All determined values are listed in Table 4.2.

	Capsule i	Capsule ii	Capsule iii	Capsule iv
$\alpha$	0.4%	0.4%	0.6%	0.3%
$\eta^{exp}$ ( $\mu\text{m}$ )	0.17	0.16	0.22	0.11

Table 4.2 – Value of wall thickness ratio  $\alpha$  and membrane thickness  $\eta$  for ovalbumin capsules i-iv.

For ovalbumin capsules i-iv shown in Fig. 4.16, we find a value of wall thickness ratio equal to  $\alpha \sim 0.3 - 0.6\%$ , and a wall thickness  $\eta \sim (0.11 - 0.22)\mu\text{m}$ . This result is very encouraging because the membrane thicknesses are in good agreement with those from Dupont *et al.* (2015), who have found a value of  $\eta \sim (0.11 - 0.16)\mu\text{m}$  by measuring capsule wrinkles generated in shear flow. The present study shows that the wrinkle analysis can act as an indirect technique for measuring the membrane thickness of micron-sized capsules. Concerning the experimental method for producing membrane wrinkles, the

microfluidic technique is more flexible and easier to manipulate than the microrheometer. In addition, since the shell model with  $\alpha = 0.01$  predicts the same overall deformations as the membrane model with  $\alpha = 0$ , it may indicate that the membrane model is competent for investigating the overall deformation of microcapsules with very thin membranes.

Although the wrinkle analysis is proved to be feasible in determining membrane thickness, its application is limited to a very thin capsule membrane, on which wrinkles can be generated under external viscous flow. In other words, this technique cannot work for a capsule with a relatively thick shell where no wrinkle is produced.

### 4.7.2 Curvature measurement

Gubspun *et al.* (2016) have performed experimental studies of flowing human serum albumin (HSA) capsules in a cylindrical channel, in which a steady-state profile of a 20% HSA capsule (denoted as capsule v) is shown in Fig. 4.18 (a). They demonstrated that the mechanical property of HSA capsules follows a correlation between capsule thickness and size inferred by capsule deformations in an elongation flow and AFM probe (de Loubens *et al.*, 2014). For capsule v with  $a^{exp} = 75\mu m$ , it is easy to find its membrane thickness and thickness ratio as  $\eta \approx 3\mu m$  and  $\alpha \approx 4\%$ . We also apply curvature measurement introduced in Fig. 4.9 to this experimental result, as shown in Fig. 4.19. Since the experimental profile cannot be strictly axisymmetric like numerical one, the typical curvature  $K_\phi^r a$  of capsule v is averaged of  $K_\phi^r a$  in the two rear ends. Results are listed in Table 4.3. By means of the correlation between  $K_\phi^r a$  and  $Ca_s$  in Fig. 4.10, we find a value of wall thickness ratio for capsule v roughly equals to 5%. It is encouraging that the wall thickness ratio of capsule v obtained by curvature measurements ( $\approx 5\%$ ) is very close to that inferred by an independent method of de Loubens *et al.* (2014) ( $\approx 4\%$ ). The curvature measurement is proved to be a feasible indirect technique for determining the wall thickness of artificial capsule with a membrane thickness ranging from 1% to 10%.

## 4.8 Identification of bending modulus

Assuming a linear incompressible material of capsule membrane, the bending modulus defined in Eq. (2.2) can be simplified as  $M_b = G_s \eta^2 / 3$ . In order to further characterize the shell bending modulus of ovalbumin capsules i-iv, their surface shear modulus  $G_s$  should be determined. We employ the data-driven automatic procedure of Quesada *et al.* (2020) to deduce  $G_s$  from experimental images. The procedure is based on a database containing predicted steady-state values  $L_z$  and  $L_p$  as functions of  $Ca_s$  and  $a/l$  for membranes governed by neo-Hookean law. More details on how to determine  $G_s$  are available in Chapter 5. For ovalbumin capsules i-iv, we find a value of bending modulus  $M_b \approx 1.7 - 6.0 \times 10^{-16} \text{ N m}$ .

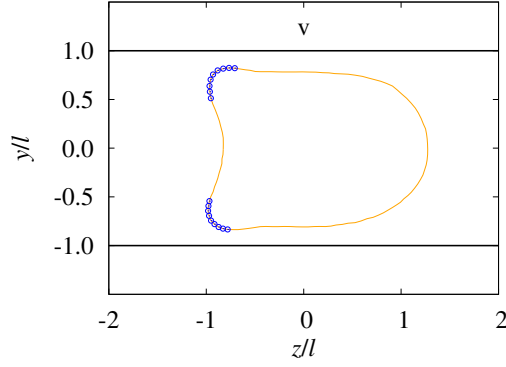


Figure 4.18 – Longitudinal profile of a 20% human serum albumin (HSA) capsule flowing in a cylindrical channel.  $a^{exp} = 75\mu\text{m}$ ,  $a^{exp}/l = 0.98$ , and  $Ca_s = 0.05$ . Results reproduced from Gubspun *et al.* (2016).

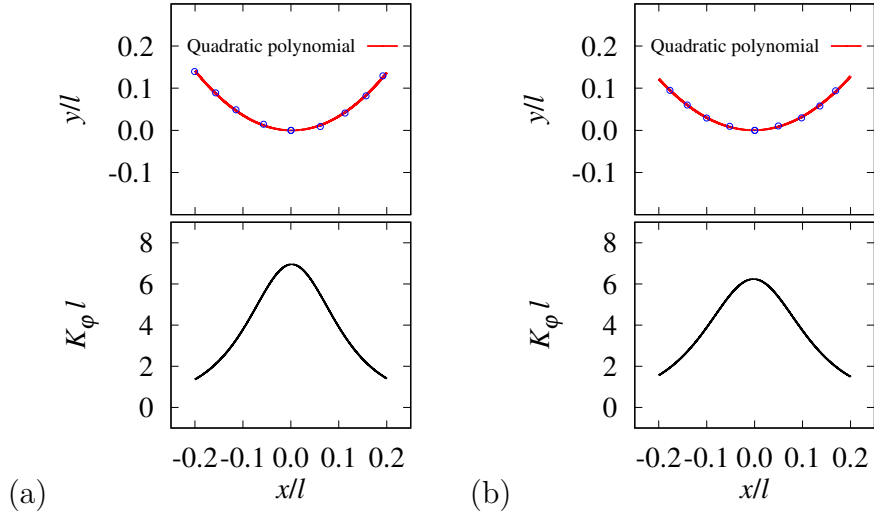


Figure 4.19 – Quadratic polynomial fitting for nodes in the rear bending membrane and curvatures of the fitting curve. The measurements are made on experimental capsule v.

For 20% HSA capsule v, the surface shear modulus can be inferred from the study of de Loubens *et al.* (2014), and the bending modulus is found to be  $M_b \approx 1.0 \times 10^{-12}\text{N m}$ . Since the thickness of capsule v is an order of magnitude larger than that of capsules i-iv, the  $G_s$  and  $M_b$  of capsule v are unsurprisingly higher than that of capsule i-iv. All determined values of  $G_s$  and  $M_b$  for capsules i-v are listed in Table 4.4.

## 4.9 Conclusion

In this chapter, we investigate the dynamic behavior of an initially spherical capsule with a finite thickness shell flowing in a cylindrical channel. The bulk capillary number  $Ca_v$  and shell thickness ratio  $\alpha$  exert a great influence on the steady-state capsule shape. When capsule typical lengths are plotted as a function of a surface capillary number  $Ca_s$ ,

Capsule v			
$K_\varphi^r l$ (a)	6.4	$K_\varphi^r l$ (b)	6.0
$K_\varphi^r a$	6.1		
$\alpha$	$\approx 5\%$		

Table 4.3 – Determined values of typical curvature  $K_\varphi^r a$  and wall thickness ratio  $\alpha$  for experimental capsule v.  $a^{exp}/l = 0.98$  and  $Ca_s = 0.05$  are known from Gubspun *et al.* (2016).

	Capsule i	Capsule ii	Capsule iii	Capsule iv	Capsule v
$G_s$ (N/m)	0.049	0.041	0.039	0.040	0.333
$M_b$ (N m)	$4.8 \times 10^{-16}$	$3.5 \times 10^{-16}$	$6.0 \times 10^{-16}$	$1.7 \times 10^{-16}$	$1.0 \times 10^{-12}$

Table 4.4 – Value of surface shear modulus  $G_s$  and bending modulus  $M_b$  for experimental capsules i-v.

increasing  $\alpha$  will soften the material, and thus the capsule shape hardly changes with  $\alpha$ . However, a typical curvature  $K_\varphi^r a$  in the rear bending area shows a distinguishable difference for different  $\alpha$ , especially when applying a high  $Ca_s$ . With varying  $\alpha$  and  $Ca_s$ , we numerically predict the membrane wrinkles formed under the combined effects of the channel confinement, membrane stretching, and shell bending resistance. A correlation law is found between the wrinkle wavelength and the shell thickness ratio. In order to characterize the membrane thickness in practice, we propose two indirect techniques based on numerical predictions and experimental observations: (i) Wrinkle measurement can characterize the thickness of a capsule whose membrane is very thin with  $\alpha < 1\%$ ; (ii) Curvature measurement can characterize the thickness of a capsule with a relatively thick membrane where  $1\% < \alpha < 10\%$ . Combining the two indirect approaches has strong flexibility for determining the values of membrane thickness and bending modulus from experiments on a variety of micron-sized capsules in confined flow.

# Membrane property determination

In order to measure the mechanical property of a batch of capsules with a cross-linked ovalbumin membrane, such as the surface shear modulus, we propose two independent microfluidic techniques, in which capsules flow in a microcapillary tube and a microrheometer. We analyze the deformation results by numerical models of the two flow situations, as shown in Fig. 5.1. The capsule wall is assumed as a two-dimensional infinitely thin surface, characterized by a surface shear modulus  $G_s$  and area dilatation modulus  $K_s$ . The numerical model can account for large membrane deformation and different material constitutive laws. The study was submitted to the journal "*Flow*" with the title "A microfluidic methodology to identify the mechanical properties of capsules: comparison with a microrheometric approach". Xing-Yi Wang and Claire Dupont performed the numerical simulations. Adlan Merlo did all experiments.

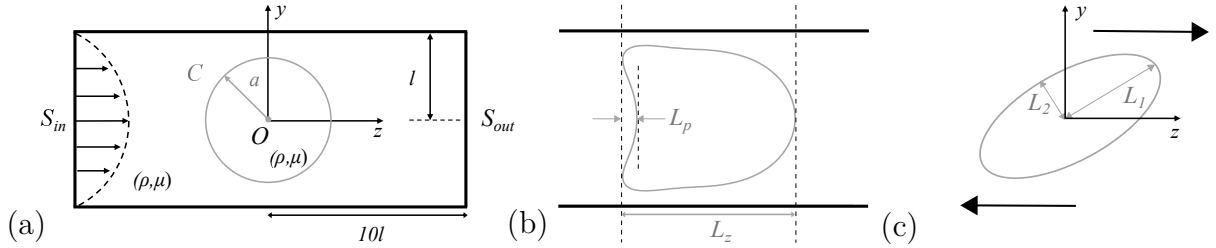





Figure 5.1 – (a) Schematic illustration of an initially spherical capsule subjected to Poiseuille flow in a cylindrical channel with radius  $l$ . Typical lengths characterizing the capsule deformation: (b)  $L_z, L_p$  in the channel and (c)  $L_1, L_2$  in an unbounded simple shear flow.

RESEARCH ARTICLE

# A microfluidic methodology to identify the mechanical properties of capsules: comparison with a microrheometric approach

Xing-Yi Wang<sup>1</sup>, Adlan Merlo<sup>1</sup>, Claire Dupont<sup></sup><sup>1</sup>, Anne-Virginie Salsac<sup>\*</sup><sup>1</sup> and Dominique Barthès-Biesel<sup></sup><sup>1</sup>

<sup>1</sup>Biomechanics and Bioengineering Laboratory (UMR 7338), Université de Technologie de Compiègne - CNRS, CS 60319, 60203 Compiègne, France

\*Corresponding author. E-mail: [anne-virginie.salsac@utc.fr](mailto:anne-virginie.salsac@utc.fr)

**Received:** XX 2020; **Revised:** XX XX 2020; **Accepted:** XX XX 2020

**Fundamental Keywords:** Capsule/cell dynamics

**Application Keywords:** Rheological measurements; fluid–structure interaction modeling, mechanical identification

## Abstract

We present a microfluidic method to measure the elastic properties of a population of microcapsules (liquid drops enclosed by a thin hyperelastic membrane). The method is based on the observation of flowing capsules in a cylindrical capillary tube and an automatic inverse analysis of the deformed profiles. The latter requires results from a full numerical model of the fluid–structure interaction accounting for nonlinear membrane elastic properties. For ease of use, we provide them under the form of databases, when the initially spherical capsule has a membrane governed by a neo-Hookean or a general Hooke’s law with different surface Poisson ratios. Ultimately, the microfluidic method yields information on the type of elastic constitutive law that governs the capsule wall material together with the value of the elastic parameters. The method is applied on a population of ovalbumin microcapsules and is validated by means of independent experiments of the same capsules subjected to a different flow in a microrheological device. This is of great interest for quality control purposes, as small samples of capsule suspensions can be diverted to a measuring test section and mechanically tested with a 10% precision using an automated process.

## Impact Statement

Encapsulation consists in enclosing a substance inside a membrane in order to protect it and control the exchanges with the environment. Recent innovative applications use capsules containing active principles, fragrances, flavors, phase change materials or organ cells. A microfluidic methodology is presented to measure the membrane elastic properties of microcapsules with a liquid core. The method is based on an inverse analysis of the deformed profiles of capsules flowing in a capillary tube. A fluid–structure numerical model that accounts for nonlinear large deformations of the capsule wall, corresponding to a strain-hardening or -softening material behavior, provides the database for the inverse analysis. The method is applied on artificial microcapsules with a cross-linked ovalbumin membrane and is validated by comparison with measures in a microrheological device. The advantage of the microfluidic method is that it is simple to implement and can be automatized for on-line measurements.

## 1. Introduction

Encapsulation consists in enclosing some internal substance inside a membrane in order to control the exchanges between the environment and the internal medium. The capsule contents are thus prevented from dispersing or degrading and can eventually be released where and when needed. Capsules are found in nature in the form of cells, bacteria, seeds, and eggs. For example, a red blood cell (RBC) is a natural capsule that transports hemoglobin, allows oxygen and carbon dioxide exchanges through the membrane, but withstands the hydrodynamic stresses prevalent in blood circulation. In industry, applications of small-scale encapsulation have become ubiquitous. Classical examples are found in cosmetics or food industry for fragrance or flavor protection (Miyazawa *et al.*, 2000; Gibbs *et al.*, 1999; Zuidam & Nedovic, 2010) but also in energy storage with phase change materials encapsulated in microcarriers (Zhao & Zhang, 2011). In medicine, new treatment techniques are being developed, such as liposome encapsulation of fragile mRNA for vaccine applications (Kowalski *et al.*, 2019) or the development of new-generation bioartificial organs where xenogenic cells (e.g. pancreas cells for diabetic patients) are encapsulated to prevent rejection reactions (Espona-Noguera *et al.*, 2019). Microencapsulation thus offers a tremendous potential in the process engineering world, but many scientific challenges remain to be tackled, especially on the engineering and physical aspects.

Encapsulated objects exist with a wide range of size (from nanometric to millimetric), shape and mechanical property (from solid to highly deformable particles). In this paper, we will focus on prototypical *initially spherical capsules*, i.e. liquid droplets enclosed by a thin elastic membrane, which are widely used in industry. We exclude solid beads, as well as vesicles, which are enclosed by a lipid bilayer with fluid membrane properties. In most applications, capsules are suspended in a carrying fluid. When the suspension is flowing, the particles are subjected to large deformations under the hydrodynamic stresses, which may lead to the membrane buckling and wrinkling and even to breakup. The motion of a microcapsule in a flowing fluid thus constitutes a formidable problem of fluid–structure interactions in the domain where the fluid stresses are mostly due to viscous and pressure effects and where the structure is undergoing large deformation. A crucial issue is thus the constitutive behavior of the wall material. Specifically, a neo-Hookean (NH) constitutive law is typically used to model walls with a strain–softening behavior, as exhibited by polymer membranes with rubber-like elasticity. For membranes with a network of strong covalent bonds, the strain–hardening behavior is often modeled by a Skalak (SK) law, which was initially designed to represent the mechanical behavior of the bi-layer membrane of the red blood cell (Skalak *et al.*, 1973). However, for artificial capsules, the generalized Hooke’s law (GH), which corresponds to the thin membrane limit of a homogeneous three-dimensional law, constitutes an interesting alternative to the SK law. Indeed, the GH law assumes a linear relation between the stress and the deformation in the reference undeformed configuration, but exhibits a nonlinear strain–hardening behavior under large deformation. Furthermore, it can account for variable degrees of wall area distensibility.

Experimentally, the measurement of the wall mechanical properties is difficult because capsules are small and fragile. For biological cells such as RBCs with a very deformable lipid bi-layer membrane, micropipette aspiration (Heinrich & Rawicz, 2005) or optical tweezers (Avsievicha *et al.*, 2020) have been proposed. Those methods are not adapted to measure artificial microcapsules with a size ranging from a few tens of micrometers to a millimeter, because the deforming forces that are applied are a few pN. If this force level is sufficient to substantially deform cells, it is much too low to have any measurable effect on capsules. Correspondingly, different techniques to test capsules have been proposed over the years, such as compression between two parallel plates for millimeter-size particles (Carin *et al.*, 2003; Risso & Carin, 2004), atomic force indentation (Fery & Weinkamer, 2007; de Loubens *et al.*, 2014), deformation in a simple shear flow created in a counter-rotating Couette viscometer (Chang & Olbricht, 1993b; Walter *et al.*, 2000; Rehage *et al.*, 2002; Koleva & Rehage, 2012) or in a planar hyperbolic flow (Barthès-Biesel, 1991; Chang & Olbricht, 1993a; de Loubens *et al.*, 2014). Those techniques are powerful, but require a sophisticated (and often expensive) set-up. Another drawback is that they are all off–line and are difficult to automatize.

Another method consists of flowing individual capsules in a microchannel (with circular or square cross section) and measuring their velocity and deformed profiles by means of video microscopy. Depending on the flow conditions, an initially spherical capsule can take a parachute or slug shape when its diameter is of the same order as the channel cross dimension. The velocity and deformed profile of each capsule are then compared to the corresponding quantities computed by a full numerical model of the capsule in flow: this inverse analysis yields a value of the shear elastic modulus of the enclosing wall (Lefebvre *et al.*, 2008; Chu *et al.*, 2011; Hu *et al.*, 2013; Gubspun *et al.*, 2016). The advantage of the technique is that it is straightforward, can be automated (Quesada *et al.*, 2020) and may thus yield statistical results for a population. However, up to now, the modulus values thus obtained have mostly been used in a relative sense to analyze the effect of a specific parameter (membrane polymerization conditions, capsules size) on the mechanical properties of a given capsule population. The modulus values have never been compared to those measured with another independent experiment (e.g. capsule in shear flow).

It is the aim of this paper to provide a robust methodology for the assessment of the mechanical properties of a microcapsule wall, based on an inverse analysis of microchannel flow measurements. In particular, we will make a full numerical study of the motion and deformation of initially spherical capsules with a GH wall when they flow in a cylindrical tube. This will allow us to evaluate the importance of the resistance to area dilation. In order to facilitate the inverse analysis, the results will be gathered in plots of the main deformation and motion parameters as functions of the confinement and flow strength. As an illustration, the methodology will be applied to evaluate the wall shear elastic modulus of artificial microcapsules with a reticulated ovalbumin membrane. We will show that changing the assumptions made regarding the wall constitutive behavior leads to different evolution of the shear modulus with the deformation level: this allows us to assess the type of rheological behavior of the capsule wall, i.e. strain-hardening or -softening. A further novelty of this study is the validation of the microchannel results by means of a comparison with those obtained from microrheometric measurements on the same capsules in a counter-rotating Couette device.

In section 2 we outline the fluid–structure interactions problem and its numerical solution. In section 3, we provide new results on the tube flow of a capsule with a GH membrane, such as deformed profiles and plots of the relevant parameters as functions of confinement, flow strength and wall Poisson ratio. We also compare the results with those obtained with different wall constitutive laws (SK and NH). In section 4, we describe the fabrication of the microcapsules, how they are tested in microfluidics and microrheometry devices, and how mechanical properties are identified from captured images of their deformed shape at steady state in both cases. We then apply the two methods to a capsule population and discuss their ability to predict the membrane elastic behavior. Section 5 is dedicated to concluding remarks.

## 2. Deformation of a spherical capsule in flow: model

We consider an initially spherical capsule (radius  $a$ ) which is filled with an internal liquid (density  $\rho$ , viscosity  $\mu$ ) and enclosed by a thin hyperelastic isotropic membrane (surface shear modulus  $G_s$ , area dilation modulus  $K_s$ ). This capsule is freely suspended in another incompressible Newtonian liquid (density  $\rho$ , viscosity  $\mu$ ), subjected to flow. Details of the analysis can be found in the review paper of Barthès-Biesel (2016) and the references therein.

### 2.1. Membrane mechanics

As the viscous forces exerted by the fluid lead to large shape distortions of the particle, care must be taken for the modeling of the wall mechanics. Correspondingly, the position of the membrane material points is denoted  $\mathbf{X}$  in the undeformed reference state and  $\mathbf{x}(\mathbf{X}, t)$  in the deformed configuration at time  $t$ . The local deformation of the membrane surface is measured by the Green-Lagrange strain tensor



$\mathbf{e} = \frac{1}{2}(\mathbf{F}^T \cdot \mathbf{F} - \mathbf{I})$ , where  $\mathbf{F} = \partial \mathbf{x} / \partial \mathbf{X}$  is the gradient of the transformation and  $\mathbf{I}$  the identity tensor. Two invariants of  $\mathbf{e}$  can be defined as

$$I_1 = \text{tr}(\mathbf{F}^T \cdot \mathbf{F}) - 2 = \lambda_1^2 + \lambda_2^2 - 2, \quad I_2 = \det(\mathbf{F}^T \cdot \mathbf{F}) - 1 = \lambda_1^2 \lambda_2^2 - 1, \quad (1)$$

where  $\lambda_1$  and  $\lambda_2$  represent the in-plane principal extension ratios. Invariant  $I_1$  measures the shear deformation, whereas  $I_2$  measures the local surface dilation. Since the membrane is infinitely thin, the three-dimensional stresses in the membrane are replaced by Cauchy tensions (forces per unit arc-length of deformed surface). The Cauchy tension tensor  $\boldsymbol{\sigma}$  depends on a strain energy function  $w_s(I_1, I_2)$  per unit undeformed surface area

$$\boldsymbol{\sigma} = \frac{1}{\lambda_1 \lambda_2} \mathbf{F} \cdot \frac{\partial w_s}{\partial \mathbf{e}} \cdot \mathbf{F}^T. \quad (2)$$

Several constitutive laws with constant material coefficients have been proposed to govern energy-deformation relationships. They are usually derived from classical three-dimensional laws in the limit where the initial thickness  $h$  of the capsule wall tends to zero. The surface shear modulus is then related to the usual three-dimensional shear modulus  $G$  by

$$G_s = hG. \quad (3)$$

The simplest law, for isotropic and hyperelastic materials, is the generalized Hooke's (GH) law, in which  $w_s$  is a quadratic function of  $\mathbf{e}$ :

$$w_s^{\text{GH}} = G_s \left( \text{tr}(\mathbf{e}^2) + \frac{\nu_s}{1 - \nu_s} [\text{tr}(\mathbf{e})]^2 \right) = \frac{G_s}{4} \left( 2I_1 - 2I_2 + \frac{1}{1 - \nu_s} I_1^2 \right), \quad (4)$$

where  $\text{tr}(\mathbf{e})$  denotes the trace of  $\mathbf{e}$  and  $-1 < \nu_s < 1$  is a surface Poisson ratio. The area dilation modulus is then  $K_s = G_s(1 + \nu_s)/(1 - \nu_s)$ , which implies that  $\nu_s \rightarrow 1$  corresponds to an area incompressible membrane. Note that  $\boldsymbol{\sigma}$  is a linear function of  $\mathbf{e}$  for small deformation ( $\mathbf{F} \simeq \mathbf{I}$ ), but becomes a nonlinear function of  $\mathbf{e}$  for large deformation, with a strain-hardening type behavior.

The two-dimensional form of the Neo-Hookean (NH) law, classically used to describe volume-incompressible rubber-like materials, is given by

$$w_s^{\text{NH}} = \frac{G_s}{2} \left( I_1 - 1 + \frac{1}{I_2 + 1} \right). \quad (5)$$

Because of the hypothesis of volume incompressibility, area dilation is balanced by membrane thinning so that  $K_s = 3G_s$ . Under large deformation, the Cauchy tensions exhibit a strain-softening type behavior.

In order to describe anisotropic biological bi-layers (such as the red blood cell membrane), Skalak *et al.* (1973) proposed a purely two-dimensional law (SK) with independent surface shear and area dilation modulus

$$w_s^{\text{SK}} = \frac{G_s}{4} \left[ (I_1^2 + 2I_1 - 2I_2) + CI_2^2 \right]. \quad (6)$$

The area dilation modulus is  $K_s = (1 + 2C)G_s$ , in which the dimensionless parameter  $C$  regulates the resistance to area dilation. Under large deformation, the Cauchy tensions exhibit a strain-hardening type behavior, that becomes more pronounced as  $C$  increases.

For  $C = 1$  and  $\nu_s = 0.5$ , corresponding to  $K_s = 3G_s$ , the three NH, GH, SK laws have the same small-deformation behavior, but predict different material responses for large strains (Barthès-Biesel *et al.*, 2002; Lac *et al.*, 2004).

When the inertia of the capsule membrane is neglected, the local equilibrium equation of the membrane reads

$$\nabla_s \cdot \boldsymbol{\sigma} + \mathbf{q} = 0, \quad (7)$$

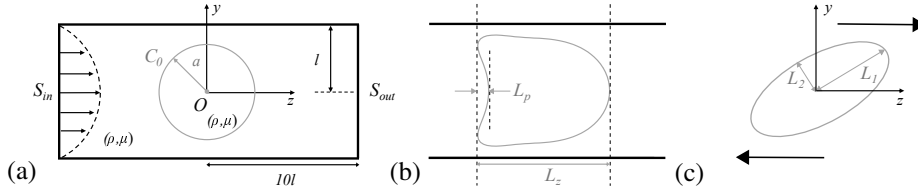


**Figure 1.** Schematic illustration of an initially spherical capsule (contour  $C_0$ ) subjected to Poiseuille flow in a cylindrical channel with radius  $l$  (a). Typical lengths characterizing the capsule deformation (contour  $C_t$  at time  $t$ ):  $L_z, L_p$  in the channel (b) and  $L_1, L_2$  in an unbounded simple shear flow (c).

where  $\nabla_s$  is the surface gradient and  $\mathbf{q}$  is the load, i.e. the external force per unit area of deformed capsule surface  $C_t$  at time  $t$ . A no-slip condition is also imposed at the capsule wall

$$\mathbf{v}(\mathbf{x}, t) = \partial \mathbf{x}(\mathbf{X}, t) / \partial t \quad \mathbf{x} \in C_t, \quad (8)$$

where  $\mathbf{v}(\mathbf{x}, t)$  is the velocity of the fluids on the capsule deformed surface.

## 2.2. Fluid–structure coupling and numerical method

The flows of the internal and external liquids are governed by the Stokes equations, subjected to no slip conditions on the capsule wall and on the flow domain outer boundary  $B$ . The velocity of the capsule wall is given by an integral equation (Pozrikidis, 2005)

$$\mathbf{v}(\mathbf{x}) = \mathbf{v}^\infty(\mathbf{x}) - \frac{1}{8\pi\mu} \left[ \int_{C_t} \mathbf{J} \cdot \mathbf{q} dS(\mathbf{y}) + \int_B \mathbf{J} \cdot \mathbf{f}^+ dS(\mathbf{y}) \right], \quad \mathbf{x} \in C_t. \quad (9)$$

where  $\mathbf{v}^\infty(\mathbf{x})$  is the unperturbed flow velocity in absence of capsule. The force  $\mathbf{q}$  on the membrane is determined from the mechanics of the capsule wall (Equation 7). The additional friction force on the domain boundaries  $\mathbf{f}^+$  must be computed as part of the solution (Hu *et al.*, 2012). The Green function  $\mathbf{J}$  is defined as

$$\mathbf{J} = \frac{1}{\|\mathbf{x} - \mathbf{y}\|} \mathbf{I} + \frac{(\mathbf{x} - \mathbf{y}) \otimes (\mathbf{x} - \mathbf{y})}{\|\mathbf{x} - \mathbf{y}\|^3}. \quad (10)$$

The problem is governed by the following non-dimensional parameters:

- The size ratio  $a/l$ , where  $l$  is the flow characteristic length,
- The membrane capillary number  $Ca_s = \mu V / G_s$ , where  $V$  is the flow characteristic velocity,
- The ratio between dilation and shear modulus  $K_s / G_s$ .

We solve this fluid–structure problem by coupling the Boundary Integral Method (BIM) to calculate the flow field, to the Finite Element Method (FEM) to calculate the force exerted by the membrane on the fluids (Walter *et al.*, 2010; Hu *et al.*, 2012). Triangular  $P_1$  elements are used to discretize all the boundaries. There are 5120  $P_1$  elements and 2562 nodes on the capsule membrane, corresponding to a characteristic element size  $\Delta h_c / l = 0.07$ . At each time step, the boundary integral equation (9) is solved to yield the velocity of the membrane. A second-order Runge-Kutta method is then used to integrate equation (8) and obtain the new deformed position of the membrane material points. This information is sent to the FEM solid solver to compute the load  $\mathbf{q}$ , which is then sent to the fluid solver to repeat the process. The explicit nature of the time integration, implies very small time steps for the scheme to be stable. Here, we use a time step  $\Delta t V / l = 5 \times 10^{-4}$ , which guarantees stability. All the reported results pertain to a steady state, for which the surface area of the capsule varies by less than  $10^{-3} \times (4\pi a^2)$  over a non-dimensional time  $tV/l = 1$ . The precision of the numerical scheme has been shown to be  $O(\Delta h_c / l)^2$  when  $P_1$  elements are used (Walter *et al.*, 2010; Dupont *et al.*, 2015).

### 3. Numerical prediction of the capsule deformed shape

#### 3.1. Deformation of a capsule flowing in a cylindrical tube

We first consider the case where a closely fitting capsule is subjected to a bounded Poiseuille flow with mean velocity  $V$ , created in a straight channel with a circular cross section of radius  $l$  (Figure 1a). We seek the steady motion and deformation of a centered capsule. Since there is a liquid film around the capsule (Figure 1b), its velocity  $v_c$  is different from  $V$  and must be computed as part of the solution. Presently, results are available for capsules with a NH or SK membrane flowing in circular (Pozrikidis, 2005; Lefebvre & Barthès-Biesel, 2007; Hu *et al.*, 2012) or square section tubes (Kuriakose & Dimitrakopoulos, 2011; Hu *et al.*, 2013). In this section, we provide new results for capsules with a GH membrane law.

The capsule centre  $O$  is initially located on the channel axis, in the middle of the tube (total length  $20l$ ) and is moved back there at each time step. The flow domain boundary  $B$  consists of the channel wall and of the entrance  $S_{in}$  and exit  $S_{out}$  sections. On the channel wall, no-slip conditions are enforced. The entrance and exit sections are far enough from the capsule for undisturbed Poiseuille flow conditions to prevail

$$v^\infty = 2V[1 - (x^2 + y^2)/l^2]e_z. \quad (11)$$

The coupled BIM-FEM solver is used, where the characteristic dimension of the channel boundary elements is  $\Delta h_w/l = 0.14$ , except in a central part with length  $2l$ , where a refined mesh is used with  $\Delta h_w/l = 0.07$ . For  $a/l \geq 0.9$ , we pre-deform the capsule into an ellipsoid that can fit inside the channel and we then follow the same procedure, while accounting for the induced pre-deformation stresses.

For a specific membrane law, the problem solution yields the capsule deformed profile and velocity  $v_c/V$  for given values of  $a/l$  and  $Ca_s$ . The overall capsule deformation is quantified with two parameters: the total length  $L_z/l$  and the parachute depth  $L_p/l$  that are easy to measure experimentally (Figure 1b).

##### 3.1.1. Capsule with a GH membrane

The combined effects of  $Ca_s$  and of  $v_s$  on the deformed profiles of the capsule are shown in Figure 2. The results are similar to those reported previously for other membrane laws. The capsule length  $L_z$  increases with flow strength. A parachute always forms for confinement ratios up to 0.9, with depth  $L_p$  increasing with  $Ca_s$ . For higher confinements  $a/l > 0.9$ , the parachute forms only when the flow strength exceeds a critical value  $Ca_{sc}$ , which increases with  $a/l$ : specifically  $Ca_{sc}$  increases from 0.03 to 0.06 when  $a/l$  increases from 1 to 1.1.

The new results in Figure 2 pertain to the effect of the membrane dilation modulus as measured by  $v_s$ . We first note that  $v_s$  has no effect on the front profile of the capsule for given values of  $a/l$  and  $Ca_s$ . The same remark applies to the global capsule profile for small flow strength (e.g.  $Ca_s = 0.01$ ) and thus moderate deformation (Figure 2a). Any influence of  $v_s$  occurs at the rear of the capsule: the main effect of a reduced resistance to dilation is an increase of the parachute depth (Figure 2b,c), resulting in a sharp parachute edge at high flow strength (Figure 2c). When such a sharp edge appears, the capsule is near the transition to continuous elongation, where it cannot reach a steady shape.

The plots in Figures 3a, b give the evolution of the two lengths  $L_z$  and  $L_p$  (characterizing the capsule deformation) with the confinement ratio  $a/l$  and capillary number  $Ca_s$ . Note that the capsule velocity  $v_c$  is larger than the average flow velocity  $V$ , due to the film around the capsule (Figure 3c). The ratio  $v_c/V$  decreases from 2 for zero size capsules (that would travel with the maximum fluid velocity) to almost unity for very large capsules (that would travel with almost the average fluid velocity).

##### 3.1.2. Effect of constitutive laws on capsule deformation

The effect of the membrane constitutive laws on capsule deformation for  $K_s = 3G_s$  is shown in Figure 4 for different confinement ratios and flow strengths. For low flow strength ( $Ca_s = 0.07$ ) and low size ratio (e.g.  $a/l = 0.8$ ), the capsule deformation is small and the three laws almost predict the same profile, as expected. As we increase  $a/l$ , while keeping  $Ca_s = 0.07$ , the stresses in the capsule membrane increase:

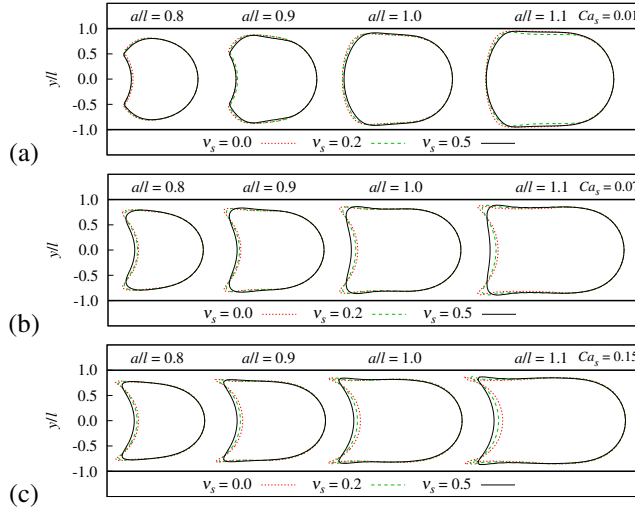


**Figure 2.** Tube flow: effect of flow strength and surface Poisson ratio  $v_s$  on the steady-state capsule profile in the  $yz$ -plane. (a)  $Ca_s = 0.01$ ; (b)  $Ca_s = 0.07$ ; (c)  $Ca_s = 0.15$ .

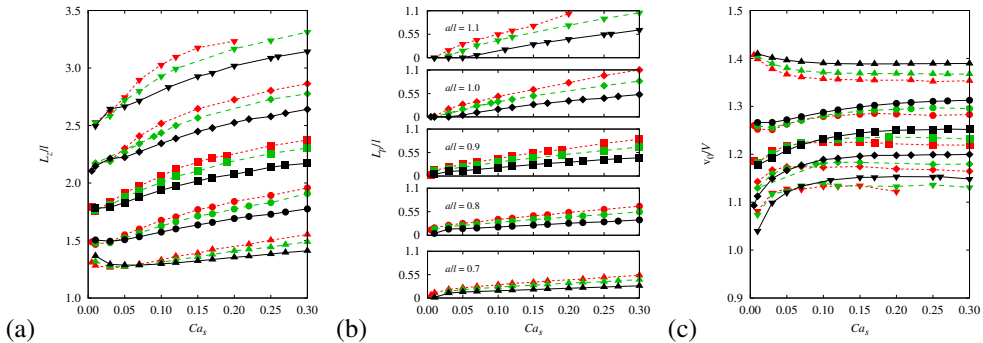


**Figure 3.** Tube flow: plots of the (a) capsule total length  $L_z$ , (b) parachute depth  $L_p$  and (c) centre of mass velocity  $v_c$  as a function of  $Ca_s$  and  $v_s$ . Same color/line style code as in Figure 2; the symbols refer to different size ratios as shown in (b).

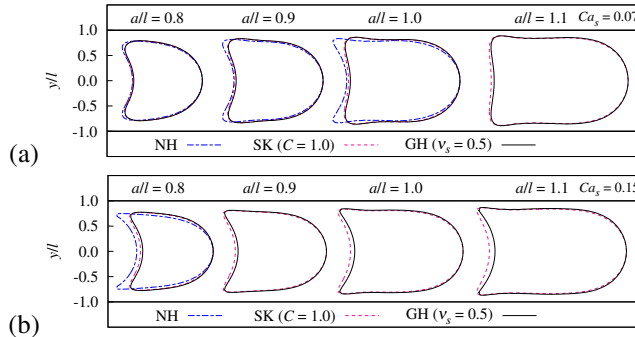


**Figure 4.** Tube flow: effect of the membrane constitutive law on the capsule deformed profile for  $K_s = 3G_s$ . (a)  $Ca_s = 0.07$ ; (b)  $Ca_s = 0.15$ .

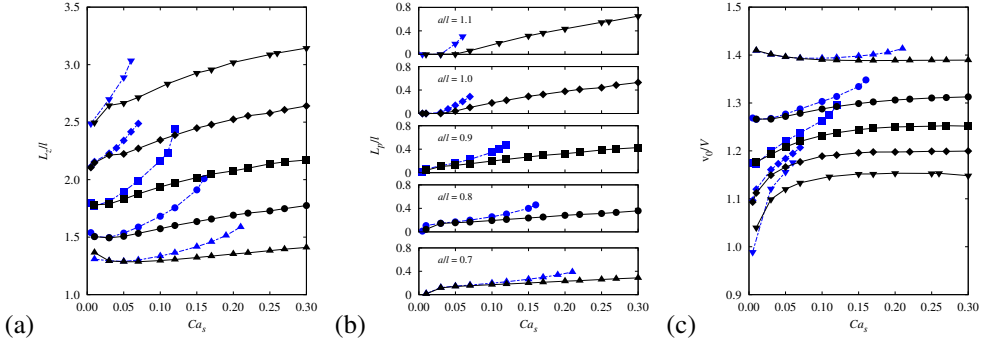


**Figure 5.** Tube flow: plots of the (a) capsule total length  $L_z$ , (b) parachute depth  $L_p$  and (c) centre of mass velocity  $v_c$  as a function of  $Ca_s$  for two membrane laws with  $K_s = 3G_s$ . Blue dotted line: NH, black full line: GH ( $v_s = 0.5$ ); the symbols refer to different size ratios as shown in (b).

as a consequence, a capsule with a strain-softening NH membrane deforms more than capsules with strain-hardening SK or GH membranes (Figure 4a). Eventually, the large ( $a/l = 1.1$ ) NH capsule does not reach steady state and undergoes continuous elongation (like the capsules with a GH law and  $v_s < 0.5$ ). As the flow strength increases (Figure 4b), continuous elongation of NH capsule occurs for lower confinement ratios, specifically for  $a/l \geq 0.85$  when  $Ca_s = 0.15$  (Hu et al., 2013). By contrast, capsules with a strain-hardening membrane can always reach a steady state. The difference between the SK or GH membranes is very small, and occurs at the rear of the capsule for large confinement ratios, only. The plots of the characteristic lengths and velocity ratio as functions of  $a/l$  and  $Ca_s$  are shown in Figure 5 for strain-softening and strain-hardening membranes (where SK results have been eliminated, as they were very close to the GH ones). All the points in Figure 5 correspond to steady situations.

The plots in Figures 3 and 5 can be used to perform the inverse analysis of the experimental profiles: from the measured values of the lengths  $L_z$  and  $L_p$ , we can deduce the size ratio  $a/l$  and capillary number  $Ca_s$  for a given membrane law. In practice it is easy to measure  $v_c$ , but difficult to control  $V$ : the plots giving  $v_c/V$  as a function of  $a/l$  and  $Ca_s$  are thus essential for the final determination of the membrane shear elastic modulus  $G_s = (\mu v_c / Ca_s)(V / v_c)$ , where  $\mu$  is the suspending fluid viscosity, which is supposedly known. From the experimental point of view, the plots in Figures 3 and 5 indicate clearly that the inverse analysis can be performed with precision only if the capsule deformation is significant enough for a parachute to form, i.e. for values of  $Ca_s > 0.05$ . Depending on their size and composition, microcapsules can have a shear modulus that varies between  $\sim 0.05$  and  $1$  N/m (Gubspun et al., 2016). They can be observed without too much blurriness only if their velocity is no more than a few mm/s. This means that the fluid viscosity must be large (of order  $1$  Pa.s) and that a high pressure is thus necessary to flow the suspension in a small diameter capillary tube. Typical experiments with the corresponding inverse analysis are described in section 4.2.

### 3.2. Deformation of a capsule in a simple shear flow

The deformation of a spherical capsule in a simple shear flow is well documented (see the review by Barthès-Biesel (2016) and the references therein). The influence of different membrane laws (NH, SK) has been studied, except for the case where the capsule wall is governed by a GH law with different values of the surface Poisson ratio. It is thus one aim of this paper to fill this void and provide a full database for this situation. We now consider the case where the capsule is freely suspended in an unbounded simple shear flow with undisturbed velocity given by

$$\mathbf{v}^\infty = \dot{\gamma} y \mathbf{e}_z. \quad (12)$$

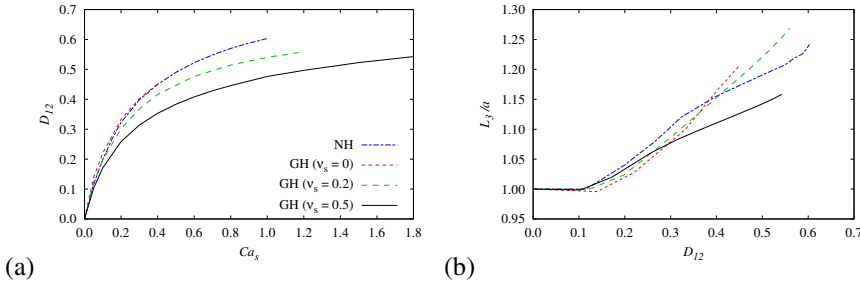


**Figure 6.** Simple shear flow: plots of the (a) capsule deformation in the shear plane and (b) profile semi-axis  $L_3$  along the vorticity direction for NH and GH laws.

where  $\dot{\gamma}$  is the shear rate. The flow problem is governed by Equation (9), where the boundary  $B$  is taken far enough from the capsule center for the perturbation  $f^+$  to be negligible. As a consequence only the first integral remains in Equation (9). The only problem parameters are then the capillary number, now defined as  $Ca_s = \mu\dot{\gamma}a/G_s$  and the ratio  $K_s/G_s$ . For a given membrane law, the model provides the deformed profile of the capsule as a function of  $Ca_s$ . As the deformed capsule is approximately ellipsoidal, we determine its ellipsoid of inertia which has semi-principal axes  $L_1, L_2$  in the shear plane (Figure 1c) and  $L_3$  in the vorticity direction. The deformation in the shear plane is then quantified by the Taylor parameter  $D_{12} = |L_1 - L_2|/(L_1 + L_2)$ . Results for  $D_{12}$  are available in the case  $K_s/G_s = 3$  for NH, SK and GH membranes (Lac & Barthès-Biesel, 2005; Walter *et al.*, 2010; Dupont *et al.*, 2015), and  $L_3$  is never given, although it is necessary to determine the deformed capsule volume. New results for GH and NH membranes are thus presented in Figure 6, where the relation between  $D_{12}$  and  $Ca_s$  is given as well as the evolution of  $L_3$  with  $D_{12}$ . For a GH membrane, the effect of decreasing  $v_s$ , i.e. the dilation modulus, is to increase the deformation for the same flow strength. For  $v_s = 0$ , the capsule undergoes continuous elongation and eventually ruptures for  $Ca_s \gtrsim 0.4$ . The same phenomenon appears around  $Ca_s = 1$  and  $D_{12} \simeq 0.6$ , for a NH membrane.

The plots of Figure 6 are simple to use: for a given membrane law, the value of deformation  $D_{12}$  yields the value of  $L_3$  and  $Ca_s$ . Knowing  $L_3, L_1$  and  $L_2$ , it is easy to compute the volume of the capsule and its initial radius  $a$ . The elastic modulus  $G_s$  is obtained from  $Ca_s$ , knowing the values of  $\dot{\gamma}$  and  $\mu$ , both given by the shear apparatus.

## 4. Experimental observation of capsule deformation and identification of the wall mechanical properties

### 4.1. Capsule fabrication

Microcapsules are fabricated by means of interfacial polymerization with cross-linking reactions (Edwards-Lévy *et al.*, 1993). Specifically, 1 ml of an aqueous solution, consisting of 10% (w/v) ovalbumin (Sigma) dissolved in phosphate buffer (pH 7.4, Sigma), is dispersed in 10 ml of vegetable oil (ISIO 4, Lesieur) at a stirring speed of 2400 rpm in a laboratory vortex (Heidolph Top-Mix 94323) for 10 seconds. Then, 10 ml of vegetable oil containing 2.5% (w/v) terephthaloyl chloride (TC, Sigma) is added to the emulsion. Interfacial reticulation is allowed to develop at rest for 15 minutes. The suspension is then centrifugated at 800 rpm for 1 minute. The supernatant is removed and replaced by vegetable oil containing 2% (v/v) Tween 20 (Sigma). The pellet is manually resuspended in this mixture by gentle successive aspirations and ejections from a pipette tip. After this first washing step, the suspension is centrifugated at 800 rpm for 1 minute. The supernatant is then removed and replaced by a 2% (v/v) solution of Tween 20 diluted in distilled water. The same resuspension procedure as in oil-Tween 20 mixture is used. This second washing step is followed by three rinsing stages, each one consisting of gently suspending the capsules in distilled water, centrifugating the suspension, and resuspending the pellet in clean distilled



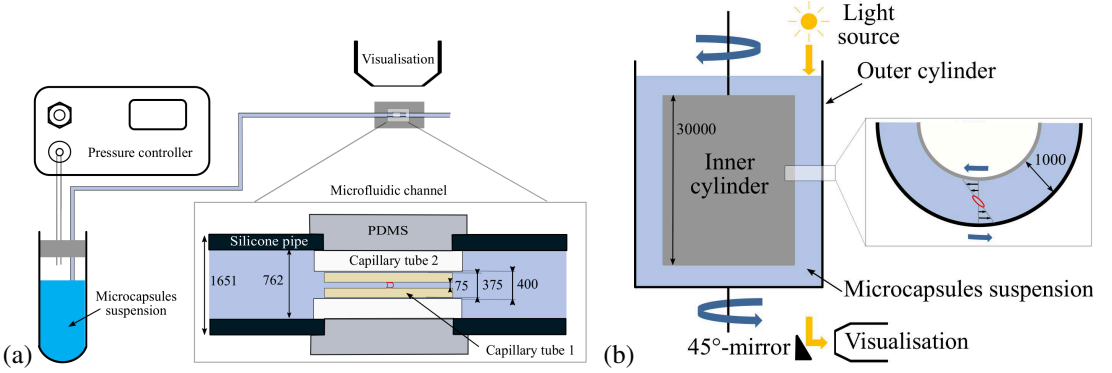


**Figure 7.** (a) Microfluidic set-up; (b) microrheometry set-up. All lengths are in  $\mu\text{m}$ .

water. This procedure yields quasi-spherical deformable capsules with radii ranging from a few tens up to a few hundreds of microns. The suspension is filtered through a  $100\ \mu\text{m}$  sieve in order to narrow the size range. The capsules are resuspended in glycerol for deformation experiment purposes. We have verified that there is no shape alteration and no apparent fluid exchanges across the membrane during at least 3 hours, which is the maximum duration of an experiment, after which the capsules are discarded.

#### 4.2. Identification of wall elasticity by flowing microcapsules in a microfluidic cylindrical capillary

The microfluidic flow system, shown in Figure 7a, consists of a straight 28-mm-long cylindrical capillary tube with an internal diameter  $2l = 75\ \mu\text{m}$  (Capillary tube 1), embedded in another tube (Capillary tube 2), which is immersed in polydimethylsiloxane (PDMS Sylgard 184, Dow Corning) to eliminate optical distortions (Lefebvre *et al.*, 2008). Just prior to an experiment,  $500\ \mu\text{l}$  of filtered capsule pellet is suspended in 12 ml glycerol (Sigma). The capsule suspension, which has a viscosity of  $\mu = 0.92\ \text{Pa}\cdot\text{s}$  at  $20^\circ\text{C}$ , is injected into the microchannel by means of a pressure controller (EZ-Flow, Fluigent). Pressure values range from 800 mbar to 1500 mbar, which provide capsule velocities from 0.8 to 6 mm/s. Image acquisitions of individual capsules flowing in the tube are performed with a fast camera (Fastcam MINI AX50, Photron) at frequencies  $f$  ranging from 2000 to 6000 Hz and an exposition time  $1/f$ . The camera is mounted on a DMI8 microscope (Leica) with a  $\times 40$  magnification and 0.6 numerical aperture objective.

Recordings are performed at least 5 mm downstream of the inlet to ensure that the capsule has reached its steady state. The capsule contours are manually extracted from the experimental images using ImageJ (NIH, USA). The capsule mid-surface and channel wall are assumed to be located in the middle of the corresponding dark contour lines (Figure 8), leading to an error of  $\pm 1$  pixel on the extracted contour points and to an error of order  $\pm 2\%$  on the extracted lengths  $L_z^{\text{exp}}$  and  $L_p^{\text{exp}}$ . The capsule velocity  $v_c^{\text{exp}}$  is determined by manually measuring the displacement of the capsule front between the first and last of 10 successive images and dividing it by the corresponding time duration. The error on  $v_c^{\text{exp}}$  is also of order  $\pm 2\%$ .

The inverse analysis strategy consists of identifying the mechanical properties from the experimental deformed profiles using the data-driven automatic procedure of Quesada *et al.* (2020). The databases contain the predicted steady-state values of  $L_z$  and  $L_p$  as functions of parameters  $Ca_s$  and  $a/l$  for the different constitutive laws (NH, GH  $\nu_s = 0.5, 0.2, 0$ ) corresponding to Figures 3 and 5. For a given constitutive law, we project the experimental values  $L_z^{\text{exp}}$  and  $L_p^{\text{exp}}$  onto the  $(L_z, L_z - L_p)$  hypersurface that contains all the admissible solutions. The corresponding  $Ca_s$  and  $a/l$  values are identified by means of diffuse approximation. This approximation uses a local weighted least squares fitting that is valid in a small neighborhood created within the lengths-space around the point  $(L_z^{\text{exp}}, L_z^{\text{exp}} - L_p^{\text{exp}})$  and containing 14 neighbors of the database. Knowing the lengths-parameters relationship for the 14

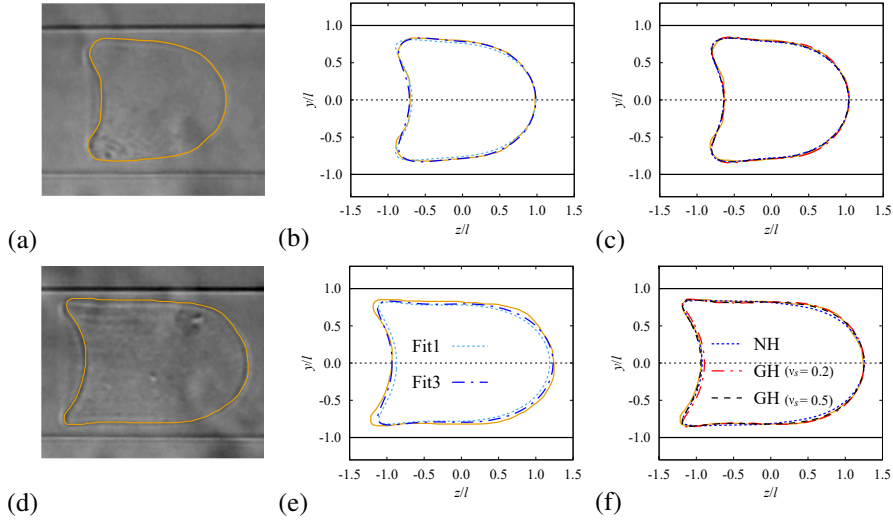


**Figure 8.** (a, d) Experimental image of the capsule in a cylindrical tube (diameter  $75 \mu\text{m}$ ) with extracted contour (full line); (b, e) two potential fits of the extracted profiles using a NH law; (c, f) Profile fits with different membrane laws. The parameters of the different fits are gathered in Table 1.

	Fit 1	Fit 2 $L_z^{exp} - 2\%$	Fit 3 $L_z^{exp} + 2\%$	Fit 4 $L_p^{exp} - 2\%$	Fit 5 $L_p^{exp} + 2\%$	NH law	GH law ( $\nu_s = 0.2$ )	GH law ( $\nu_s = 0.5$ )
	Figure 8(b)					Figure 8(c)		
$a/l$	0.88	0.89	0.88	0.90	0.87	0.90	0.91	0.89
$Ca_s$	0.06	0.04	0.07	0.05	0.07	0.05	0.04	0.07
$G_s$ (N/m)	0.044	0.067	0.037	0.053	0.037	0.053	0.071	0.035
$H/a$ (%)	1.9	1.6	2.7	1.6	3.1	1.6	2.0	1.9
	Figure 8(e)					Figure 8(f)		
$a/l$	0.98	0.99	0.97	0.99	0.96	0.99	1.02	1.01
$Ca_s$	0.08	0.07	0.09	0.07	0.09	0.07	0.08	0.13
$G_s$ (N/m)	0.037	0.043	0.033	0.043	0.033	0.043	0.036	0.022
$H/a$ (%)	5.1	4.5	5.9	3.4	7.0	3.4	2.4	2.4

**Table 1.** Size ratio  $a/l$ , surface capillary number  $Ca_s$ , surface shear modulus  $G_s$  and non-dimensional modified Hausdorff distance  $H/a$  corresponding to the different profile fits of Figure 8. The NH and GH ( $\nu_s = 0.2, 0.5$ ) results correspond to Fit 1.

data points, we deduce the values of  $Ca_s^{fit}$  and  $(a/l)^{fit}$  for the measured lengths by solving an inverse problem. The surface representing  $v_c/V$  as a function of  $a/l$  and  $Ca_s$  is decomposed into triangles with vertices on the database points. The point  $\{Ca_s^{fit}, (a/l)^{fit}\}$  corresponds to one triangle of the velocity surface and the ratio  $(v_c/V)^{fit}$  is the distance weighted average of the values of  $v_c/V$  on the three vertices (Delaunay triangulation procedure). The membrane shear modulus  $G_s$  is then

$$G_s = \frac{\mu v_c^{exp}}{Ca_s^{fit}} \left( \frac{V}{v_c} \right)^{fit}. \quad (13)$$

As a check, we compute the numerical deformed profile of the capsule, corresponding to the values  $\{Ca_s^{fit}, (a/l)^{fit}\}$  and compare it to the experimental profile. The modified (i.e. mean) Hausdorff distance  $H/a$  between the two profiles gives an estimate of the precision of the inverse analysis. Any capsule that



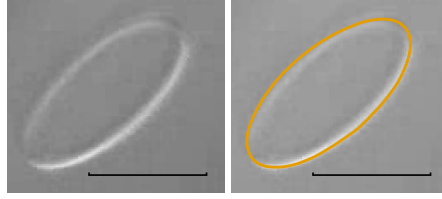


**Figure 9.** Experimental image of the capsule in a simple shear flow with extracted contour. The scale indicates 75  $\mu\text{m}$ .

cannot be fitted with  $H/a \leq 0.06$  is discarded. We also discard non symmetrical profiles which cannot be analyzed with the model.

For a given law, different fits are obtained using the values  $L_z^{exp}$ ,  $L_p^{exp}$  (Fit 1), decreasing/increasing  $L_z^{exp}$  (and thus  $L_p^{exp}$ ) by 2% (Fit 2/Fit 3 respectively) and finally, decreasing/increasing  $L_p^{exp}$  by 2% while keeping  $L_z^{exp}$  constant (Fit 4/Fit 5 respectively). This procedure allows us to evaluate the sensitivity of the inverse analysis to experimental error. It also allows us to compute a mean value and deviation for  $G_s$ . As an example, we consider two deformed profiles (Figures 8a,d) and the resulting inverse analysis fits with a NH law (Figures 8b,e showing only Fits 2 and 3 for clarity). The corresponding fit values are gathered in Table 1. For the smaller capsule ( $a/l \simeq 0.9$ ), the five fits are equally good in terms of Hausdorff distance, but lead to a 27% dispersion of shear modulus values ( $G_s = 0.048 \pm 0.0013\text{N/m}$ ): this dispersion is mostly due to the fact that, for capsules smaller than the tube radius ( $a/l \leq 0.9$ ), the lengths  $L_z$  or  $L_p$  do not vary much with  $Ca_s$  (Figure 5) thus a small variation of  $L_z$  leads to a large variation of  $Ca_s$ . For the larger capsule ( $a/l \simeq 1$ ), the Hausdorff distance is near the acceptable limit of  $0.06a$  (except for Fit 4 which is discarded), mainly, because the tips are not fitted very well. However, the capsule being large, the dispersion is only 13% on the shear modulus values ( $G_s = 0.039 \pm 0.0005\text{N/m}$ ). This shows that an absolute value of the precision of the inverse analysis procedure cannot be evaluated with a single parameter such as  $H/a$  as it depends on the quality of the fit and also on the capsule size and deformation level. The same procedure can be applied to fit the profile with other membrane laws as shown in Figures 8c,f where only the results of Fit 2 are shown. Of course, the values of  $G_s$  depend on the law as shown in Table 1.

### 4.3. Identification of wall elasticity using microrheometry

We now use a microrheometric device to determine the capsule membrane properties by subjecting the particles to a simple shear flow. A 10 ml volume of a capsule suspension in glycerol (volume concentration 0.5%) is placed in a counter-rotating Couette viscometer (MCR 702, Anton Paar). The viscometer consists of a transparent cup and an opaque inner cylinder with a 1 mm gap (Figure 7b). A  $45^\circ$  mirror, located under the cup, allows us to observe the capsules in the shear plane by means of a camera (model LM165M, Lumenera) with a x5 magnification and 0.14 numerical aperture objective, operating at 32 frames/s. The camera is focused on the mid-plane of the gap, where the flow velocity is zero. We only record the capsules that are stationary and appear clearly in the observation window (which is easier to say than to do). During an experiment, the shear rate  $\dot{\gamma}$  is kept constant for a typical duration of 10 min and is progressively increased. The contour of the deformed capsules is extracted manually with ImageJ. A least squares fit of the contour with an ellipse yields the values of the semi-axes  $L_1$  and  $L_2$  (Figure 9). Note that the pictures are not as sharp as those obtained with the microfluidic set-up, due to inferior performance of the camera included in the device and to the fact that it is challenging to keep the capsule steady. The fuzziness of the profile leads to an error of  $\pm 20\%$  on  $D_{12}$ . Correspondingly, it is unreasonable to try to analyze capsules with  $D_{12} < 0.35$ .

The inverse analysis is straightforward, because the deformation of the capsule depends on only one parameter,  $Ca_s$ . For a given law and shear rate  $\dot{\gamma}$ , the measured semi-axes  $L_1$  and  $L_2$  yield the deformation  $D_{12}$  from which we deduce  $Ca_s$  and  $L_3/a$  using the plots in Figure 6. The capsule radius

is thus  $a = \sqrt{L_1 L_2 L_3 / a}$  and the shear modulus is  $G_s = \mu \dot{\gamma} a / Ca_s$ . The capsule presented in Figure 9 is subjected to a  $350 \text{ s}^{-1}$  shear rate in a fluid with viscosity  $0.756 \text{ Pa.s}$ . The radius is  $a = 45 \text{ }\mu\text{m}$  and the deformation  $D_{12} = 0.38$  provides a value of shear elastic modulus equal to  $G_s = 0.044 \text{ N/m}$  for a NH membrane and to  $0.024$  or  $0.038 \text{ N/m}$  for a GH membrane with  $\nu_s = 0.5$  or  $0.2$ , respectively.

#### 4.4. Characterization of a capsule population

As we measure a capsule suspension in both set-ups, we can have results on a population. In order to compare the values of  $G_s$  obtained with different membrane laws, it is convenient to use the mean profile elongation  $\Lambda = p / 2\pi a$  where  $p$  is the perimeter of the capsule deformed profile in the  $yz$ -plane. The non-linear constitutive law, which is appropriate to model the capsule membrane, is the one that yields the same constant value of  $G_s$  for any deformation level  $\Lambda$ . Note that all laws should lead to the same small deformation value of  $G_s$ , since they are then equivalent.

The results from the microfluidic device are shown in Figure 10, where the values of  $G_s$ , obtained from the analysis of different deformed capsules with an estimated radius in the range  $32 - 47 \text{ }\mu\text{m}$ , are plotted as a function of  $\Lambda$  for three different membrane laws (NH and GH with  $\nu_s = 0.5$  or  $0.2$ ). The error bars correspond to the dispersion of the five fits. As explained earlier, they are larger for small deformation and/or small  $Ca_s$ . In order to visualize the trend of the data, a best fit of  $G_s$  values obtained with each law, is also shown.

The values of  $G_s$  obtained with NH law are approximately constant with a mean value  $G_s = 0.043 \pm 0.004 \text{ N/m}$ . This indicates that the NH law is a good candidate to model the ovalbumin membrane of the capsules. The results obtained with GH ( $\nu_s = 0.5$ ) law are in the same range as the results for NH law for small deformation ( $\Lambda = 1.06$ ), as expected. However, the values of  $G_s$  tend to decrease with increasing deformation: this means that the strain-hardening GH law is not fit to model the membrane behavior under large deformation, since the parameter  $G_s$  must be decreased as deformation increases. The larger dispersion of the NH values of  $G_s$  compared to that of the GH ones is linked to the fact that the values of  $Ca_s$  are larger for the GH analysis than for the NH one.

Furthermore, it is possible to verify if, indeed, the capsule membrane is shear-softening. This is done by increasing the flow strength until a continuous elongation regime is reached. The set-up described in Figure 7a did not allow for high enough flow velocity to reach this regime. However, as a proof of concept, we have flowed the same capsules in a slightly different microfluidic system consisting of a square section ( $100 \times 100 \text{ }\mu\text{m}^2$ ) channel. Continuous elongation of a capsule is then observed under high flow velocity, as shown in Figure 11.

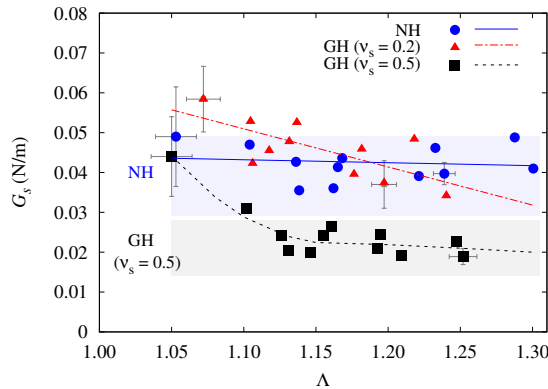


**Figure 10.** Plots of surface shear modulus  $G_s$  as a function of capsule mean deformation  $\Lambda$ . Symbols represent the constitutive law. The lines show a linear best fit for the corresponding points. The shaded areas correspond to the mean value  $G_s \pm 25\%$  obtained with microrheometry.

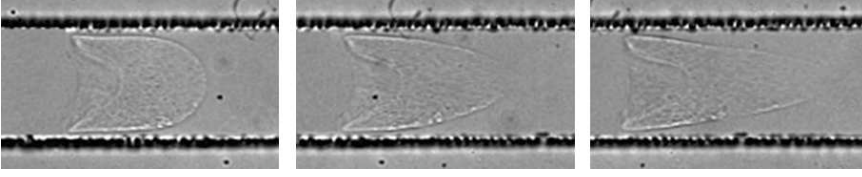


**Figure 11.** Left to right: successive profiles of a capsule showing continuous elongation in a square section channel ( $100 \times 100 \mu\text{m}^2$ ,  $a = 50 \mu\text{m}$ ,  $V_c \sim 23 \text{ mm/s}$ ,  $\mu = 0.92 \text{ Pa.s}$ ). The capsule has travelled about  $200 \mu\text{m}$  between two successive profiles and is clearly undergoing break-up in the last picture. Images taken by E. Hasiak.

When we use the GH law with  $\nu_s = 0.2$ , it is difficult to fit the experimental profiles with the same values of  $a/l$  as those used for the NH or GH ( $\nu_s = 0.5$ ) fits: the size ratio has to be increased by 10 to 15%. This leads to values  $Ca_s$  that are smaller than those obtained with the other fits and consequently to larger values of  $G_s$ , as can be noted in Figure 10. The significant decrease of  $G_s$  with deformation and the dispersion of the fit results using the GH ( $\nu_s = 0.2$ ) law indicate that  $\nu_s = 0.2$  is not appropriate to model capsules with an ovalbumin membrane. Gubspun et al. (2017) conducted pore flow experiments on capsules with a reticulated human serum albumin membrane (thus very similar to the present capsules with an ovalbumin membrane) and provide deformed profiles with their respective size ratios  $a/l$  and  $Ca_s$  values obtained assuming a GH membrane with  $\nu_s = 0.4$ . We have tried to fit the published profiles with the same law and with the indicated parameter values without success. This may indicate that the GH law with values of  $\nu_s < 0.5$  is not very appropriate to model this type of capsules.

When we analyze the microrheometric measurements, it is not possible to give a trend of the values of  $G_s$  with  $\Lambda$  because of the fairly large error on  $D_{12}$ . We have measured 25 capsules with a radius between  $30$  and  $46 \mu\text{m}$  subjected to deformation levels  $0.35 < D_{12} < 0.5$ . There is a definite effect of the membrane constitutive law because the deformation is fairly large. Correspondingly, the mean value of the shear modulus depends on the law: it is found to be  $G_s = 0.039 \pm 0.01 \text{ N/m}$  for NH law,  $G_s = 0.021 \pm 0.007 \text{ N/m}$  for GH ( $\nu_s = 0.5$ ) and  $G_s = 0.033 \pm 0.01 \text{ N/m}$  for GH ( $\nu_s = 0.2$ ), all with a standard deviation of  $\pm 25\%$ . This large deviation is mostly linked to the error in the measurement of  $D_{12}$ . Another source of error is also due to the fact that the inverse analysis uses deformation curves obtained for a viscosity ratio equal to unity between the internal and external liquids, whereas this ratio is much smaller than 1 in the experiments. However, Foessel et al. (2011) showed that the influence of this viscosity ratio is very small and does not modify significantly the relationship between  $D_{12}$  and  $Ca_s$ , up to  $D_{12} \simeq 0.5$ . This is why we have discarded results with deformation larger than 0.5.

Altogether, the microrheometric  $G_s$  values, shown as shaded areas in Figure 10, overlap well with the results obtained with the microfluidic tube for large deformation. This is clear for the NH law, for which  $G_s$  is found to have the nearly constant value  $0.043 \pm 0.004 \text{ N/m}$  by microfluidics or  $0.039 \pm 0.01 \text{ N/m}$  by microrheometry. In the case of GH ( $\nu_s = 0.5$ ) law, this conclusion applies for the range of values of  $G_s$  obtained for large deformation ( $\Lambda > 1.10$ ) i.e.  $0.027 \sim 0.015 \text{ N/m}$  by microfluidics and  $0.021 \pm 0.007 \text{ N/m}$  by microrheometry.

This validates the microfluidic approach to measure microcapsule properties.

## 5. Conclusion

The main objective of this paper was to propose a microfluidic methodology to measure the elastic properties of a population of microcapsules. Why this method? Because the operating principle is simple and the experimental set-up fairly inexpensive, apart from the visualization devices (microscope and high-speed camera), which are indispensable to any dynamic micro-apparatus. The method is based on the observation of flowing capsules in a cylindrical capillary tube and an inverse analysis of the deformed profiles. The latter requires a full numerical model of the fluid–structure interaction, that accounts for

nonlinear membrane elastic properties, which we provide under the form of databases for an initially spherical capsule with a membrane governed by a neo-Hookean or general Hooke's law with different surface Poisson ratios. We also detail how the inverse analysis can be automated to provide information on the type of elastic constitutive law that governs the capsule wall material together with the value of the corresponding elastic parameters. This is possible because the confinement imposed by the microfluidic configuration allows for large deformation of the capsule membrane. Note that a microfluidic method, based on a similar inverse analysis adapted to the specific case of red blood cells, has been proposed to analyze automatically large cell populations (Saadat *et al.*, 2020). The shape characterization is different from the one presented here, as it had to be adapted to smaller, discoidal particles.

Another microrheological method is used where the capsules are subjected to a simple shear flow in a counter rotating Couette device. The method consists in capturing the deformed profile of those capsules with their centre of mass in the zero velocity plane, which is somewhat tricky to perform. The necessary databases for the inverse analysis are also provided for an initially spherical capsule with a membrane governed by a neo-Hookean or general Hooke's law with different surface Poisson ratios.

We validate the two methods by confronting the results obtained with either one on a population of artificial capsules with cross-linked ovalbumin membrane. We test three types of membrane laws, to find for which constant values of  $G_s$  are obtained: a strain-softening NH law and two strain-hardening GH laws with dilation to shear ratios  $K_s/G_s = 3$  or  $1.5$  ( $\nu_s = 0.5$  or  $0.2$ ). The microfluidic method predicts that the membrane shear modulus  $G_s$  is approximately constant for a NH law: this indicates that this constitutive law is appropriate to model the mechanical behavior of the ovalbumin membrane. In contrast, the values of  $G_s$  decrease with deformation for GH ( $\nu_s = 0.5$ ) law and exhibit much dispersion for GH ( $\nu_s = 0.2$ ) law. With the microrheometric method, there is too much experimental uncertainty to decide which law is best adapted to describe the constitutive behavior of the membrane material. On average though, the high-deformation values of the membrane shear elastic modulus are the same with the two methods for any given law: this validates the microfluidic methodology. A further potentiality of the microfluidic methodology is that once  $G_s$  is known, it is possible in principle to check if the capsule membrane is strain-softening (NH law) or strain-hardening (GH law). This can be done by increasing the flow rate to exceed the critical value of  $Ca_s$  past which continuous elongation occurs when the membrane is strain-softening. If continuous elongation is observed, the NH law is a good candidate to model the wall behavior. If not, the wall is then strain-hardening and GH law should serve as a good approximation.

The feasibility study on artificial ovalbumin capsules allows us to define the optimal conditions to diminish the impact of inherent uncertainties. For the microfluidic method to be precise, the capsule global deformation should be large enough, i.e. the elongation ratio  $\Lambda$  of the perimeter of the observed profiles should be larger than 1.05. Furthermore, the size ratio between the capsule and the tube radii, should not be smaller than 0.9: indeed, for smaller ratios, the deformation does not vary much with flow strength, thus leading to large errors in the determination of the latter. Note that the capsule must be transparent enough to allow measurement of the penetration length of the parachute, which is an essential feature of the deformation. Consequently, the microfluidic method will not work on opaque capsules, whereas the rheometric method would still be pertinent.

Potentially, the great strength of this technique is that it allows to determine the type of membrane constitutive behavior: strain-hardening or -softening. This is very important as, under given flow stress, strain-softening capsules may be more prone to deformation induced damage than strain-hardening ones. Furthermore, the microfluidic method is well adapted for quality control, as it allows small batches of a capsule suspension to be diverted from a production line to a measuring test section. Of course, images and their contour should be acquired automatically, as done by Minetti *et al.* (2014) or Saadat *et al.* (2020), and post-treated automatically as explained in this paper.

### Funding Statement

We gratefully acknowledge funding from the China Scholarship Council (PhD scholarship of X.Y. Wang) and from the European Research Council (ERC) under the European Union's Horizon 2020 research and innovation programme (Grant agreement No. ERC-2017-COG - MultiphysMicroCaps).

### Declaration of Interests

The authors declare no conflict of interest.

### Author Contributions

A.V.S. and D.B.B. created the research plan, designed experiments and numerics and formulated the analytical/numerical problem. X.Y.W. and C.D. led the numerical simulations and implemented the inverse analysis, A.M. performed all the experiments. All the authors contributed on the analysis of the results.

### Data Availability Statement

Raw data are available from the corresponding author (A.V.S.).

### Ethical Standards

The research meets all ethical guidelines, including adherence to the legal requirements of the study country.

## References

- AVSIEVICH, TATIANA, ZHUA, RUIXUE, POPOV, ALEXEY, BYKOVA, ALEXANDER & MEGLINSKI, IGOR 2020 The advancement of blood cell research by optical tweezers. *Reviews Physics* **5**, 100043.
- BARTHÈS-BIESEL, D. 1991 Role of interfacial properties on the motion and deformation of capsules in shear flow. *Physica A* **172**, 103 – 124.
- BARTHÈS-BIESEL, D. 2016 Motion and deformation of elastic capsules and vesicles in flow. *Annual Review of Fluid Mech.* **48**, 25–52.
- BARTHÈS-BIESEL, D., DIAZ, A. & DHENIN, E. 2002 Effect of constitutive laws for two-dimensional membranes on flow-induced capsule deformation. *J. Fluid Mech.* **460**, 211–222.
- CARIN, M., BARTHÈS-BIESEL, D., EDWARDS-LÉVY, F., POSTEL, C. & ANDREI, D. C. 2003 Compression of biocompatible liquid-filled HSA-alginate capsules: Determination of the membrane mechanical properties. *Biotechnol. Bioengng* **82**, 207–212.
- CHANG, K. S. & OLBRICHT, W. L. 1993a Experimental studies of the deformation and breakup of a synthetic capsule in extensional flow. *J. Fluid Mech.* **250**, 587 – 608.
- CHANG, K. S. & OLBRICHT, W. L. 1993b Experimental studies of the deformation and breakup of a synthetic capsule in steady and unsteady simple shear flow. *J. Fluid Mech.* **250**, 609 – 633.
- CHU, T. X., SALSAC, A. V., LECLERC, E., BARTHÈS-BIESEL, D., WURTZ, H. & EDWARDS-LÉVY, F. 2011 Comparison between measurements of elasticity and free amino group content of ovalbumin microcapsule membranes: discrimination of the cross-linking degree. *J. Colloid Interface Sci.* **355**, 81–88.
- DE LOUBENS, C., DESCHAMPS, J., GEORGELIN, M., CHARRIER, A., EDWARD-LÉVY, F. & LEONETTI, M. 2014 Mechanical characterization of cross-linked serum albumin microcapsules. *Soft Matter* **10**, 4561 – 4568.
- DUPONT, C., SALSAC, A.-V., BARTHÈS-BIESEL, D., VIDRASCU, M. & LE TALLEC, P. 2015 Influence of bending resistance on the dynamics of a spherical capsule in shear flow. *Phys. Fluids* **27** (5), 051902.
- EDWARDS-LÉVY, F., ANDRY, M. C. & LÉVY, M. C. 1993 Determination of free amino group content of serum albumin microcapsules using trinitrobenzenesulfonic acid: effect of variations in polycondensation pH. *Int. J. Pharmaceut.* **96**, 85–90.

- ESPONA-NOGUERA, A., CIRIZA, J., CANIBANO-HERNANDEZ, A., ORIVE, G., HERNANDEZ, R.M., DE BURGO, L. SAENZ & PEDRAZ, J. L. 2019 Review of advanced hydrogel-based cell encapsulation systems for insulin delivery in type 1 diabetes mellitus. *Pharmaceutics* **11**, 597.
- FERY, A. & WEINKAMER, R. 2007 Mechanical properties of micro- and nanocapsules: Single capsule measurements. *Polymer* **48**, 7221–7235.
- FOESSEL, E., WALTER, J., SALSAC, A.-V. & BARTHÈS-BIESEL, D. 2011 Influence of internal viscosity on the large deformation and buckling of a spherical capsule in a simple shear flow. *J. Fluid Mech.* **672**, 477 – 486.
- GIBBS, B. F., KERMASHA, S., ALLI, I. & MULLIGAN, C. N. 1999 Encapsulation in the food industry: a review. *Int. J. Food Sci. Nutr.* **50**, 213–224.
- GUBSPUN, J., GIRES, P.Y., DE LOUBENS, C., BARTHÈS-BIESEL, D., DESCHAMPS, J., GEORGELIN, M., LEONETTI, M., LECLERC, E., EDWARDS-LÉVY, F. & SALSAC, A.V. 2016 Characterization of the mechanical properties of cross-linked serum albumin microcapsules: effect of size and protein concentration. *Colloid Poly. Sci.* **294**, 1381–1389.
- GUBSPUN, J., DE LOUBENS, C., TROZZO, R., DESCHAMPS, J., GEORGELIN, M., EDWARDS-LÉVY, F. & LEONETTI, M. 2017 Perturbations of the flow induced by a microcapsule in a capillary tube. *Fluid Dyn. Res.* **49**, 035501.
- HEINRICH, V. & RAWICZ, W. 2005 Automated, high-resolution micropipet aspiration reveals new insight into the physical properties of fluid membranes. *Langmuir* **21**, 1962–1971.
- HU, X. Q., SALSAC, A. V. & BARTHÈS-BIESEL, D. 2012 Flow of a spherical capsule in a pore with circular or square cross-section. *J. Fluid Mech.* **705**, 176–194.
- HU, X. Q., SÉVÉNIÉ, B., SALSAC, A. V., LECLERC, E. & BARTHÈS-BIESEL, D. 2013 Characterizing the membrane properties of capsules flowing in a square-section microfluidic channel: Effects of the membrane constitutive law. *Phys. Rev. E* **87**, 063008.
- KOLEVA, I. & REHAGE, H. 2012 Deformation and orientation dynamics of polysiloxane microcapsules in linear shear flow. *Soft Matter* **8**, 3681 – 3693.
- KOWALSKI, P.K., RUDRA, A., MIAO, L. & ANDERSON, D. G. 2019 Delivering the messenger: advances in technologies for therapeutic mRNA delivery. *Molecular therapy* **27**, 710–728.
- KURIAKOSE, S. & DIMITRAKOPOULOS, P. 2011 Motion of an elastic capsule in a square microfluidic channel. *Phys. Rev. E* **84**, 011906.
- LAC, E. & BARTHÈS-BIESEL, D. 2005 Deformation of a capsule in simple shear flow: effect of membrane prestress. *Phys. Fluids* **17**, 0721051 – 0721058.
- LAC, E., BARTHÈS-BIESEL, D., PELEKASIS, N. A. & TSAMOPOULOS, J. 2004 Spherical capsules in three-dimensional unbounded Stokes flows: effect of the membrane constitutive law and onset of buckling. *J. Fluid Mech.* **516**, 303–334.
- LEFEBVRE, Y. & BARTHÈS-BIESEL, D. 2007 Motion of a capsule in a cylindrical tube: effect of membrane pre-stress. *J. Fluid Mech.* **589**, 157–181.
- LEFEBVRE, Y., LECLERC, E., BARTHÈS-BIESEL, D., WALTER, J. & EDWARDS-LÉVY, F. 2008 Flow of artificial microcapsules in microfluidic channels: a method for determining the elastic properties of the membrane. *Phys. Fluids* **20**, 123102.
- MINETTI, C., PODGORSKI, T., COUPIER, G. & DUBOIS, F. 2014 Fully automated digital holographic processing for monitoring the dynamics of a vesicle suspension under shear flow. *Biomed. Optics Express* **5**, 1554–1568.
- MIYAZAWA, K., YAJIMA, I., KANEDA, I. & YANAKI, T. 2000 Preparation of a new soft capsule for cosmetics. *J. Cosmet. Sci.* **51**, 239–252.
- POZRIKIDIS, C 2005 Numerical simulation of cell motion in tube flow. *Ann. Biomed. Engng* **33**, 165–178.
- QUESADA, C., DUPONT, C., VILLON, P. & SALSAC, A. V. 2020 Diffuse approximation for identification of the mechanical properties of microcapsules. *Math. Mech. Solids* , arXiv: <https://doi.org/10.1177/1081286520977602>.
- REHAGE, H., HUSMANN, M. & WALTER, A. 2002 From two-dimensional model networks to microcapsules. *Rheol. Acta* **41**, 292.



- 502 RISSO, F. & CARIN, M. 2004 Compression of a capsule: Mechanical laws of membranes with negligible  
503 bending stiffness. *Phys. Rev. E* **69**, 061601–061608.
- 504 SAADAT, A., HUYKE, D. A., OYARZUN, D. I., ESCOBAR, P. V., VREEIDE, I. H. Ø, SHAQFEH, E. S.G. &  
505 SANTIAGO, J. G. 2020 A system for the high-throughput measurement of the shear modulus distribution  
506 of human red blood cells. *Lab on a Chip* **16**, 2927–2936.
- 507 SKALAK, R., TOZEREN, A., ZARDA, R. P. & CHIEN, S. 1973 Strain energy function of red blood cell  
508 membranes. *Biophys. J.* **13**, 245–264.
- 509 WALTER, A., REHAGE, H. & LEONHARD, H. 2000 Shear-induced deformation of polyamid microcapsules.  
510 *Colloid Polymer Sci.* **278**, 169–175.
- 511 WALTER, J., SALSAC, A. V., BARTHÈS-BIESEL, D. & LE TALLEC, P. 2010 Coupling of finite element and  
512 boundary integral methods for a capsule in a Stokes flow. *Intl J. Numer. Meth. Engng* **83**, 829–850.
- 513 ZHAO, C.Y. & ZHANG, G.H. 2011 Review on microencapsulated phase change materials (MEPCMs):  
514 Fabrication, characterization and applications. *Renewable and Sustainable Energy Reviews* **15**, 3813–  
515 3832.
- 516 ZUIDAM, N. J. & NEDOVIC, V. 2010 *Encapsulation technologies for active food ingredients and food*  
517 *processing*. New York: Springer.





# Conclusions and perspectives

---

## 6.1 Conclusions

This dissertation has enriched the numerical results of dynamic responses of an initially spherical capsule flowing through a microchannel. The capsule wall is modeled as a homogeneous thin shell with a finite thickness accounting for the bending resistance of the material. A coupling numerical model developed by Dupont *et al.* (2015) solves the fluid-structure interaction problem of a capsule in an external flow, in which a Boundary Integral Method solving for capsule flow with a Shell Finite Element Method solving for shell deformation. We adapt this model to a confined flow case for the first time to investigate the effect of wall bending resistance and channel confinement on capsule dynamics. The numerical model is stable even when the capsule membrane undergoes a large deformation with a curvature reversal shape.

We investigate the influence of wall bending resistance and flow strength on the dynamics of an initially spherical capsule subjected to an unbounded parabolic flow or a bounded Poiseuille flow. The results show that the general shape of the deformed capsule is mainly affected by the stretching of the membrane since the energy caused by bending is relatively small compared with that by membrane stretching. Under a significant flow strength, the capsule with a negligible wall thickness predicts unrealistic pointed-ends in the rear bending area. However, the capsule with a thick shell can avoid having such issues because of an increased bending resistance. An apparent decrease of capsule deformation is observed by increasing the wall thickness in this case. We also compute the bending energy density and curvature of nodes on the steady-state capsule surface for different wall thicknesses and flow strengths. A correlating study indicates that the bending energy density is not a quadratic function of mean curvature change.

Parachute shape and wrinkling of the membrane are the most remarkable post-buckling behaviors when the capsule flows in a tube with comparable dimensions. When the membrane rheological behavior follows the neo-Hookean law and varying wall thicknesses and flow strengths, we have computed the typical curvature in the rear of the parachute for the first time, as well as predicted the physical wrinkles of capsules in confined flow. We show that the wrinkle wavelength only depends on the shell bending resistance, which coincides with the wrinkle analysis of capsules subjected to a simple shear flow performed

by Dupont *et al.* (2015). A constitutive law is then obtained by correlating the wrinkle wavelength to the shell thickness. In order to determine the membrane thickness of capsules in real suspensions, we have proposed two indirect techniques to inverse analyze the experimental images. We show that the wrinkle measurement can characterize the thickness of a capsule whose wall thickness ratio  $< 1\%$ , while curvature measurement can characterize the thickness of a capsule with a relatively thick membrane with a wall thickness ratio of  $1 - 10\%$ . Such methods can help to infer values of membrane thickness and bending modulus from experiments on spherical capsules in confined flow.

Numerical simulations are also performed to investigate capsule rheological behavior when the membrane is governed by a neo-Hookean (NH) or a generalized Hooke's (GH) law and neglecting bending resistance. The simulation results show that under high flow strength, a membrane governed by NH law exhibits strain-softening elastic behavior, while it is strain-hardening for membrane governed by GH law. A database is then provided, including the capsule geometric dimensions predicted under different capsule initial sizes, flow strengths, and membrane laws. For the purpose of characterizing membrane mechanical properties of a batch of capsules, we have performed experiments with flowing capsules in a cylindrical capillary tube. We propose an automatic microfluidic method for measuring the capsule elastic properties based on experimental observation and analysis of their deformed profiles. The results show that the ovalbumin capsule exhibits strain-softening elastic behavior since a fairly constant value of membrane elastic modulus is found by assuming NH law. The advantage of the microfluidic method is that it can be automatized and performed on-line for quality control purposes with a 10% precision.

## 6.2 Perspectives

We have investigated the capsule rheological behavior when the membrane is governed by a generalized Hooke's (GH) law in Chapter 5. However, the wall thickness and bending resistance are neglected. Their effects on the dynamic behavior of a capsule subjected to an external flow have not been studied yet. Since the present shell model allows different membrane laws to govern the elastic behavior of the mid-surface, we preliminarily study the deformation of an initially spherical capsule flowing in a cylindrical channel when the membrane is governed GH law and has different wall thicknesses.

### Capsule axial deformation

We consider an initially spherical capsule subjected to a bounded Poiseuille flow. The capsule wall is modeled as a thin shell characterized by a mid-surface and wall thickness depicted in Chapter 2. The membrane elastic behavior follows GH law. Fig. 6.1 shows

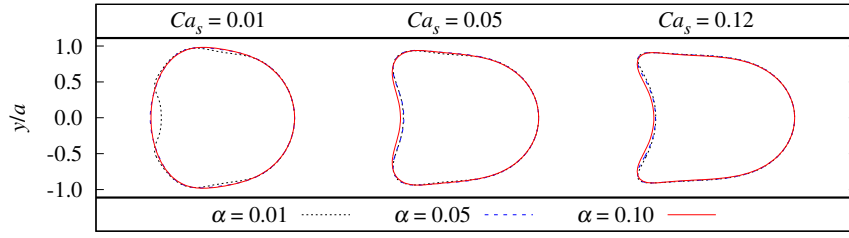


Figure 6.1 – Effect of wall thickness ratio  $\alpha$  and surface capillary number  $Ca_s$  on the longitudinal capsule profile at steady-state. Size ratio  $a/l = 0.9$ .  $\alpha = 0.01, 0.05$ , and  $0.10$ .  $Ca_s = 0.01, 0.05$ , and  $0.12$ . Membrane behavior follows the Generalized Hooke's law with a surface Poisson ratio  $\nu_s = 0.5$ .

the comparison of longitudinal capsule profiles of different  $\alpha$  under a given  $Ca_s$ . Under a small flow strength with  $Ca_s = 0.01$ , the profile of  $\alpha = 0.05$  and  $0.10$  are still very near and no curvature inversion on the shape, while  $\alpha = 0.01$  generates a small concave in the rear due to its negligible bending resistance. For a moderate flow strength with  $Ca_s = 0.05$ , the profiles of different  $\alpha$  almost superimpose and bending resistance has a small effect. For a high flow intensity with  $Ca_s = 0.12$ , capsule deformations of different  $\alpha$  are still very near and no pointed-ends in the rear, unlike the deformation results of capsule membrane with NH law.

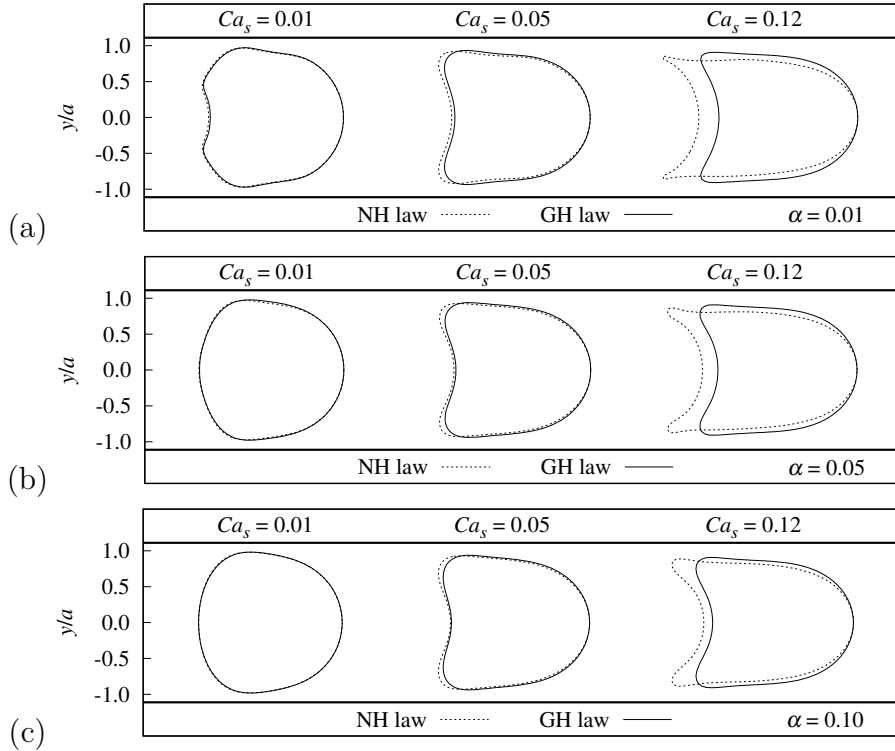


Figure 6.2 – Effect of the membrane constitutive law on the steady-state profiles for  $K_s = 3G_s$ . Size ratio  $a/l = 0.9$ .  $Ca_s = 0.01, 0.05$ , and  $0.12$ . (a)  $\alpha = 0.01$ ; (b)  $\alpha = 0.05$ ; (c)  $\alpha = 0.10$ .

Assuming an incompressible material of capsule membrane, both GH and NH laws correspond to  $K_s = 3G_s$ , where  $K_s$  is area dilatation modulus, and  $G_s$  is surface shear modulus. The effect of membrane constitutive laws on capsule deformation for  $K_s = 3G_s$  is shown in Fig. 6.2 for different flow strengths and wall thicknesses. The size ratio is fixed to  $a/l = 0.9$ . For a given  $\alpha$ , the capsule deformation is small under a small flow strength with  $Ca_s = 0.01$  and the two laws predict the same profile as expected. As we increase  $Ca_s = 0.07$  or  $0.12$ , the elastic stresses in the capsule membrane increase, leading that a capsule with a strain-softening NH membrane deforms more than capsules with strain-hardening GH membranes.

## Membrane wrinkle

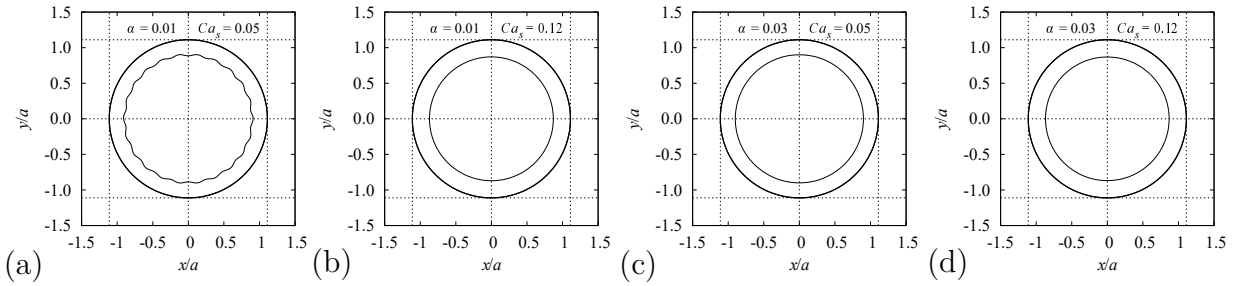


Figure 6.3 – Capsule profiles in the cross-section plane cutting along the center of mass. Size ratio  $a/l = 0.9$ . The membrane behavior is governed by the GH law. (a)  $\alpha = 0.01$ ,  $Ca_s = 0.05$ ; (b)  $\alpha = 0.01$ ,  $Ca_s = 0.12$ ; (c)  $\alpha = 0.03$ ,  $Ca_s = 0.05$ ; (d)  $\alpha = 0.03$ ,  $Ca_s = 0.12$ .

Capsule profiles in the cross-section plane cutting along the center of mass are shown in Fig. 6.3 for different wall thicknesses and flow strengths. Size ratio  $a/l = 0.9$ , and the membrane behavior is governed by the GH law. For  $\alpha = 0.01$  and  $Ca_s = 0.05$ , wrinkles occur on the capsule surface, as shown in Fig. 6.3 (a). We use the method introduced in section 4.5 to compute the non-dimensional wavelength, which is  $\lambda_w/R_m = 0.287 \pm 0.03$ . The corresponding  $\lambda_w/R_m$  when membrane follows NH law is found to be  $\lambda_w/R_m = 0.285 \pm 0.03$  in section 4.5 for the same  $\alpha$  and  $Ca_s$ . It may indicate that the correlation between wavelength and thickness in Eq. (4.2) is independent of the elasticity behavior of the material. When  $\alpha = 0.01$  and  $Ca_s = 0.12$ , as shown in Fig. 6.3 (b), wrinkles are no longer exist at a high flow intensity. It is probably due to the fact that the strain-hardening material becomes stiffer under a large deformation and thus resists the wrinkling behavior. When the thickness increases to  $\alpha = 0.03$ , as seen in Fig. 6.3 (c) and (d), there is no wrinkle on the capsule surface for small and large  $Ca_s$ , because both an increased wall bending resistance and more stiff material under large deformation can resist the formation of membrane wrinkle.

Based on this dissertation, it will be interesting to continue the research at the following aspects:

- **Characterization of the membrane thickness for a batch of artificial capsules.** Using the two indirect techniques for measuring membrane thickness introduced in section 4.7, we can determine the membrane thickness of microcapsules with a variety of sizes. It would be interesting to study the correlation between membrane thickness and capsule initial radius.
- **Effect of bending resistance on capsule dynamics when the membrane is governed by GH law.** More simulations with different size ratios, wall thicknesses, and flow strengths are required to generate a database of capsule typical dimensions and typical rear curvatures. It would help characterize the mechanical property of artificial capsules with strain-hardening elastic behaviors.
- **Dynamic behavior of ellipsoidal microcapsules in suspension: Effect of initial shapes and membrane properties.** Microcapsules or cells are usually non-spherical in nature, like red blood cells. In biotechnology and pharmacology applications, a technique to increase the transfer properties of capsules is to make the particles non-spherical as it increases the surface-to-volume ratio. It would be interesting to study the motion and deformation of ellipsoidal microcapsules in suspension when they have different initial shapes and membrane properties.



# Formula derivation

---

## Derivation process of Eq. (3.9)

The derivation starts from Eq. (3.8)

$$W_b^\Psi = \frac{1}{2} \left( \frac{\eta^3}{12} C^{\alpha\beta\lambda\mu} \psi_{\alpha\beta} \psi_{\lambda\mu} \right). \quad (3.8)$$

Substituting the expression of  $C^{\alpha\beta\lambda\mu}$  (2.62),

$$W_b^\Psi = \frac{1}{2} \left[ \frac{\eta^3}{12} G \left( A^{\alpha\lambda} A^{\beta\mu} + A^{\alpha\mu} A^{\beta\lambda} + \frac{2\nu}{1-\nu} A^{\alpha\beta} A^{\lambda\mu} \right) \psi_{\alpha\beta} \psi_{\lambda\mu} \right].$$

Substituting the expression of  $M_b$  (2.2),

$$W_b^\Psi = \frac{1}{2} M_b \nu \left[ \frac{1-\nu}{2\nu} \left( A^{\alpha\lambda} A^{\beta\mu} + A^{\alpha\mu} A^{\beta\lambda} \right) \psi_{\alpha\beta} \psi_{\lambda\mu} + \left( A^{\alpha\beta} A^{\lambda\mu} \right) \psi_{\alpha\beta} \psi_{\lambda\mu} \right].$$

Assuming an incompressible material with Poisson ratio  $\nu = 0.5$ ,

$$W_b^\Psi = \frac{1}{2} M_b \frac{1}{2} \left[ \frac{\left( A^{\alpha\lambda} A^{\beta\mu} + A^{\alpha\mu} A^{\beta\lambda} \right) \psi_{\alpha\beta} \psi_{\lambda\mu}}{2} + \left( A^{\alpha\beta} A^{\lambda\mu} \right) \psi_{\alpha\beta} \psi_{\lambda\mu} \right].$$

Considering the following mathematical transformations,

$$\begin{aligned} A^{\alpha\lambda} A^{\beta\mu} \psi_{\alpha\beta} \psi_{\lambda\mu} &= \text{tr} \left( \underline{\underline{\psi}}^2 \right) = \Psi_1^2 + \Psi_2^2, \\ A^{\alpha\beta} A^{\lambda\mu} \psi_{\alpha\beta} \psi_{\lambda\mu} &= \text{tr} \left( \underline{\underline{\psi}} \right)^2 = (\Psi_1 + \Psi_2)^2, \end{aligned}$$

where  $\Psi_1$  and  $\Psi_2$  are principal bending deformations of tensor  $\underline{\underline{\psi}}$ . Finally, Eq. (3.8) can be rewritten as

$$W_b^\Psi = \frac{1}{2} M_b \left( \Psi_1^2 + \Psi_2^2 + \Psi_1 \Psi_2 \right),$$

or

$$W_b^\Psi = 2M_b \Psi_M^2 - 0.5M_b \Psi_G. \quad (3.9)$$

## Derivation process of Eq. (3.10)

In mixed co-contravariant base, the mean bending deformation  $\Psi_M$  can be computed by

$$\begin{aligned}\Psi_M &= \frac{1}{2} \text{tr } \underline{\underline{\psi}} \\ &= \frac{1}{2} \text{tr } \left( \psi_\beta^\alpha \underline{A}_\alpha \otimes \underline{A}^\beta \right) \\ &= \frac{1}{2} \left( A^{\alpha\lambda} \kappa_{\lambda\alpha} - A^{\alpha\lambda} K_{\lambda\alpha} \right),\end{aligned}$$

and the mean curvature change  $(K_M - K_0)$  can be computed by

$$\begin{aligned}K_M - K_0 &= \frac{1}{2} \text{tr } \left( \underline{\underline{K}} - \underline{\underline{K}} \right) \\ &= \frac{1}{2} \text{tr } \left( \kappa_\beta^\alpha \underline{a}_\alpha \otimes \underline{a}^\beta - K_\beta^\alpha \underline{A}_\alpha \otimes \underline{A}^\beta \right) \\ &= \frac{1}{2} \left( a^{\alpha\lambda} \kappa_{\lambda\alpha} - A^{\alpha\lambda} K_{\lambda\alpha} \right).\end{aligned}$$

Then we make a subtraction between  $\Psi_M$  and  $(K_M - K_0)$ ,

$$\begin{aligned}\Psi_M - (K_M - K_0) &= \frac{1}{2} \left( A^{\alpha\lambda} - a^{\alpha\lambda} \right) \kappa_{\lambda\alpha} \\ &= \frac{1}{2} \text{tr } \left\{ \begin{bmatrix} A^{11} - a^{11} & A^{12} - a^{12} \\ A^{12} - a^{12} & A^{22} - a^{22} \end{bmatrix} \begin{bmatrix} \kappa_{11} & \kappa_{12} \\ \kappa_{12} & \kappa_{22} \end{bmatrix} \right\} \\ &= \frac{1}{2} \text{tr } \left\{ \left( [A^{\alpha\beta}] - [a^{\alpha\beta}] \right) [\kappa_{\alpha\beta}] \right\},\end{aligned}$$

where the contravariant metric tensors  $A^{\alpha\beta}$  and  $a^{\alpha\beta}$  are defined by

$$\underline{\underline{A}} = A^{\alpha\beta} \underline{A}_\alpha \otimes \underline{A}_\beta \quad \text{and} \quad \underline{\underline{a}} = a^{\alpha\beta} \underline{a}_\alpha \otimes \underline{a}_\beta.$$

The right Cauchy-Green deformation tensor  $\underline{\underline{C}}_s$  is defined by

$$\begin{aligned}\underline{\underline{C}}_s &= a_{\alpha\beta} \underline{A}^\alpha \otimes \underline{A}^\beta \\ &= \begin{bmatrix} \lambda_1^2 & 0 \\ 0 & \lambda_2^2 \end{bmatrix}.\end{aligned}$$

Then the inverse form is

$$\begin{aligned}\underline{\underline{C}}_s^{-1} &= a^{\alpha\beta} \underline{A}_\alpha \otimes \underline{A}_\beta \\ &= \begin{bmatrix} 1/\lambda_1^2 & 0 \\ 0 & 1/\lambda_2^2 \end{bmatrix}.\end{aligned}$$



We assume that there exists an orthogonal unit basis  $(\underline{A}_1, \underline{A}_2)$  along principal directions of  $\underline{\underline{C}}_s$ . As a result,  $[A^{\alpha\beta}]$ ,  $[a^{\alpha\beta}]$ , and  $[\kappa^{\alpha\beta}]$  become diagonal matrices. Finally, the difference between  $\Psi_M$  and  $(K_M - K_0)$  becomes

$$\begin{aligned}
 \Psi_M - (K_M - K_0) &= \frac{1}{2} (A^{\alpha\alpha} \kappa_{\alpha\alpha} - a^{\alpha\alpha} \kappa_{\alpha\alpha}) \\
 &= \frac{1}{2} (\kappa_{11} (A^{11} - a^{11}) + \kappa_{22} (A^{22} - a^{22})) \\
 &= \frac{1}{2} \left( \kappa_{11} \left( 1 - \frac{1}{\lambda_1^2} \right) + \kappa_{22} \left( 1 - \frac{1}{\lambda_2^2} \right) \right) \\
 &= \frac{1}{2} \left( \kappa_{11} \left( \frac{\lambda_1^2 - 1}{\lambda_1^2} \right) + \kappa_{22} \left( \frac{\lambda_2^2 - 1}{\lambda_2^2} \right) \right). \tag{3.10}
 \end{aligned}$$

## Derivation process of Eq. (3.11)

The Gaussian bending deformation  $\Psi_G$  can be computed by

$$\begin{aligned}
 \Psi_G &= \det \underline{\underline{\psi}} \\
 &= \det \left[ (\kappa_{\alpha\beta} - K_{\alpha\beta}) \underline{A}^\alpha \otimes \underline{A}^\beta \right],
 \end{aligned}$$

and the Gaussian curvature  $K_G - K_0^2$  change can be computed by

$$\begin{aligned}
 K_G - K_0^2 &= \det \underline{\underline{\kappa}} - \det \underline{\underline{K}} \\
 &= \det \left( \kappa_{\alpha\beta} \underline{a}^\alpha \otimes \underline{a}^\beta \right) - \det \left( K_{\alpha\beta} \underline{A}^\alpha \otimes \underline{A}^\beta \right).
 \end{aligned}$$

We also assume that there exists an orthogonal unit basis  $(\underline{A}_1, \underline{A}_2)$  along principal directions of  $\underline{\underline{C}}_s$ . Then  $\Psi_G$  can be rewritten as

$$\begin{aligned}
 \Psi_G &= (\kappa_{11} - K_{11})(\kappa_{22} - K_{22})A^{11}A^{22} \\
 &= \kappa_{11}\kappa_{22} - K_0(\kappa_{11} + \kappa_{22}) + K_0^2,
 \end{aligned}$$

with  $K_{11} = K_{22} = K_0$ , and  $A^{11} = A^{22} = 1$ .  $K_G - K_0^2$  can be rewritten as

$$\begin{aligned}
 K_G - K_0^2 &= \kappa_{11}\kappa_{22}a^{11}a^{22} - K_{11}K_{22}A^{11}A^{22} \\
 &= \kappa_{11}\kappa_{22}\frac{1}{\lambda_1^2\lambda_2^2} - K_0^2,
 \end{aligned}$$

with  $a^{11} = 1/\lambda_1^2$ ,  $a^{22} = 1/\lambda_2^2$ ,  $K_{11} = K_{22} = K_0$ , and  $A^{11} = A^{22} = 1$ . Finally, the difference between  $\Psi_G$  and  $(K_G - K_0^2)$  becomes

$$\begin{aligned}
 \Psi_G - (K_G - K_0^2) &= \kappa_{11}\kappa_{22} \left( 1 - \frac{1}{\lambda_1^2\lambda_2^2} \right) - K_0(\kappa_{11} + \kappa_{22}) + 2K_0^2 \\
 &= \kappa_{11}\kappa_{22} \left( \frac{\lambda_1^2\lambda_2^2 - 1}{\lambda_1^2\lambda_2^2} \right) - 2K_0K_M + 2K_0^2 \\
 &= \kappa_{11}\kappa_{22} \left( \frac{\lambda_1^2\lambda_2^2 - 1}{\lambda_1^2\lambda_2^2} \right) - 2K_0(K_M - K_0) \\
 &\approx -2K_0(K_M - K_0).
 \end{aligned} \tag{3.11}$$

# Bibliography

---

- ABKARIAN, M., FAIVRE, M., HORTON, R., SMISTRUP, K., BEST-POPESCU, C. A. & STONE, H. A. 2008 Cellular-scale hydrodynamics. *Biomed. Mater.* **3** (3), 034011.
- BARTHÈS-BIESEL, D. 2011 Modeling the motion of capsules in flow. *Curr. Opin. Colloid Interface Sci.* **16** (1), 3–12.
- BARTHÈS-BIESEL, D. 1980 Motion of a spherical microcapsule freely suspended in a linear shear flow. *J. Fluid Mech.* **100** (4), 831–853.
- BARTHÈS-BIESEL, D. 1991 Role of interfacial properties on the motion and deformation of capsules in shear flow. *Physica A* **172**, 103 – 124.
- BARTHÈS-BIESEL, DOMINIQUE 2016 Motion and deformation of elastic capsules and vesicles in flow. *Annu. Rev. Fluid Mech.* **48**, 25–52.
- BARTHÈS-BIESEL, D., DIAZ, A. & DHENIN, E. 2002 Effect of constitutive laws for two-dimensional membranes on flow-induced capsule deformation. *J. Fluid Mech.* **460**, 211.
- BARTHÈS-BIESEL, D. & RALLISON, J. M. 1981 The time-dependent deformation of a capsule freely suspended in a linear shear flow. *J. Fluid Mech.* **113**, 251–267.
- BARTHÈS-BIESEL, D. & SGAIER, H. 1985 Role of membrane viscosity in the orientation and deformation of a spherical capsule suspended in shear flow. *J. Fluid Mech.* **160**, 119–135.
- BATOZ, J. L. & DHATT, G. 1992 *Modélisation des structures par éléments finis: Coques*. Hermès.
- BENZA, H. I. & MUNYENDO, W. L. 2011 A review of progress and challenges in soft gelatin capsules formulations for oral administration. *Int. J. Pharm. Sci. Rev. Res* **10**, 20–24.
- BROWN, E. N., KESSLER, M. R., SOTTOS, N. R. & WHITE, S. R. 2003 In situ poly (urea-formaldehyde) microencapsulation of dicyclopentadiene. *J. Microencapsul.* **20** (6), 719–730.

- CARIN, M., BARTHÈS-BIESEL, D., EDWARDS-LÉVY, F., POSTEL, C. & ANDREI, D. C. 2003 Compression of biocompatible liquid-filled hsa-alginate capsules: Determination of the membrane mechanical properties. *Biotechnol. Bioeng.* **82** (2), 207–212.
- CARUSO, F. 2000 Hollow capsule processing through colloidal templating and self-assembly. *Chem. Eur. J.* **6** (3), 413–419.
- CERDA, E. & MAHADEVAN, L. 2003 Geometry and physics of wrinkling. *Phys. Rev. Lett.* **90** (7), 074302.
- CHANG, K. S. & OLBRICHT, W. L. 1993*a* Experimental studies of the deformation and breakup of a synthetic capsule in extensional flow. *J. Fluid Mech.* **250**, 587 – 608.
- CHANG, K. S. & OLBRICHT, W. L. 1993*b* Experimental studies of the deformation and breakup of a synthetic capsule in steady and unsteady simple shear flow. *J. Fluid Mech.* **250**, 609–633.
- CHAPELLE, D. & BATHE, K. J. 2010 *The finite element analysis of shells-fundamentals*. Springer Science & Business Media.
- CHU, T. X., SALSAC, A. V., LECLERC, E., BARTHÈS-BIESEL, D., WURTZ, H. & EDWARDS-LÉVY, F. 2011 Comparison between measurements of elasticity and free amino group content of ovalbumin microcapsule membranes: discrimination of the cross-linking degree. *J. Colloid Interface Sci.* **355** (1), 81–88.
- CLAVICA, F., HOMSY, A., JEANDUPEUX, L. & OBRIST, D. 2016 Red blood cell phase separation in symmetric and asymmetric microchannel networks: effect of capillary dilation and inflow velocity. *Sci. Rep.* **6**, 36763.
- CUOMO, F., LOPEZ, F., PILUDU, M., MIGUEL, M. G., LINDMAN, B. & CEGLIE, A. 2015 Release of small hydrophilic molecules from polyelectrolyte capsules: Effect of the wall thickness. *J. Colloid Interface Sci.* **447**, 211–216.
- DIAZ, A. & BARTHÈS-BIESEL, D. 2001 Entrance of a bioartificial capsule in a pore. *Comput. Model. Eng. Sci.* **3** (3), 321–338.
- DIAZ, A., PELEKASIS, N. & BARTHÈS-BIESEL, D. 2000 Transient response of a capsule subjected to varying flow conditions: effect of internal fluid viscosity and membrane elasticity. *Phys. Fluids* **12** (5), 948–957.
- DODDI, S. K. & BAGCHI, P. 2008 Lateral migration of a capsule in a plane poiseuille flow in a channel. *Int. J. Multiph. Flow* **34** (10), 966–986.

- DODDI, S. K. & BAGCHI, P. 2009 Three-dimensional computational modeling of multiple deformable cells flowing in microvessels. *Phys. Rev. E* **79** (4), 046318.
- DONG, W. F., FERRI, J. K., ADALSTEINSSON, T., SCHÖNHOF, M., SUKHORUKOV, G. B. & MÖHWALD, H. 2005 Influence of shell structure on stability, integrity, and mesh size of polyelectrolyte capsules: mechanism and strategy for improved preparation. *Chem. Mater.* **17** (10), 2603–2611.
- DUPIRE, J., SOCOL, M. & VIALLAT, A. 2012 Full dynamics of a red blood cell in shear flow. *Proc. Natl. Acad. Sci.* **109** (51), 20808–20813.
- DUPONT, C. 2014 Biomécanique de capsules en écoulement. PhD thesis, l'Ecole Polytechnique.
- DUPONT, C., SALSAC, A. V., BARTHÈS-BIESEL, D., VIDRASCU, M. & LE TALLEC, P. 2015 Influence of bending resistance on the dynamics of a spherical capsule in shear flow. *Phys. Fluids* **27** (5), 051902.
- EDWARDS-LÉVY, F., ANDRY, M. C. & LÉVY, M. C. 1993 Determination of free amino group content of serum albumin microcapsules using trinitrobenzenesulfonic acid: effect of variations in polycondensation ph. *Int. J. Pharmaceut.* **96** (1-3), 85–90.
- ELGETI, J., KAUPP, U. B. & GOMPPER, G. 2010 Hydrodynamics of sperm cells near surfaces. *Biophys. J.* **99** (4), 1018–1026.
- ESPONA-NOGUERA, A., CIRIZA, J., CANIBANO-HERNANDEZ, A., ORIVE, G., HERNANDEZ, R.M., DE BURGO, L. SAENZ & PEDRAZ, J. L. 2019 Review of advanced hydrogel-based cell encapsulation systems for insulin delivery in type 1 diabetes mellitus. *Pharmaceutics* **11**, 597.
- FEDOSOV, D. A., CASWELL, B., POPEL, A. S. & KARNIADAKIS, G. E. 2010 Blood flow and cell-free layer in microvessels. *Microcirculation* **17** (8), 615–628.
- FERY, A. & WEINKAMER, R. 2007 Mechanical properties of micro- and nanocapsules: Single capsule measurements. *Polymer* **48**, 7221–7235.
- FOESEL, E., WALTER, J., SALSAC, A. V. & BARTHÈS-BIESEL, D. 2011 Influence of internal viscosity on the large deformation and buckling of a spherical capsule in a simple shear flow. *J. Fluid Mech.* **672**, 477 – 486.
- GHIRARDI, P., CATENAZZO, G., MANTERO, O., MEROTTI, G. C. & MARZO, A. 1977 Bioavailability of digoxin in a new soluble pharmaceutical formulation in capsules. *J. Pharm. Sci.* **66** (2), 267–269.

- GIBBS, B. F., KERMASHA, S., ALLI, I. & MULLIGAN, C. N. 1999 Encapsulation in the food industry: a review. *Int. J. Food Sci. Nutr.* **50**, 213–224.
- GUBSPUN, J., GIRES, P.Y., DE LOUBENS, C., BARTHÈS-BIESEL, D., DESCHAMPS, J., GEORGELIN, M., LEONETTI, M., LECLERC, E., EDWARDS-LÉVY, F. & SALSAC, A.V. 2016 Characterization of the mechanical properties of cross-linked serum albumin microcapsules: effect of size and protein concentration. *Colloid Poly. Sci.* **294**, 1381–1389.
- GUBSPUN, J., DE LOUBENS, C., TROZZO, R., DESCHAMPS, J., GEORGELIN, M., EDWARDS-LÉVY, F. & LEONETTI, M. 2017 Perturbations of the flow induced by a microcapsule in a capillary tube. *Fluid Dyn. Res.* **49**, 035501.
- GUCKENBERGER, A. & GEKLE, S. 2017 Theory and algorithms to compute helfrich bending forces: A review. *J. Phys. Condens. Matter* **29** (20), 203001.
- GUCKENBERGER, A., KIHM, A., JOHN, T., WAGNER, C. & GEKLE, S. 2018 Numerical–experimental observation of shape bistability of red blood cells flowing in a microchannel. *Soft Matter* **14** (11), 2032–2043.
- HALPERN, D. & SECOMB, T. W. 1989 The squeezing of red blood cells through capillaries with near-minimal diameters. *J. Fluid Mech.* **203**, 381–400.
- HEINRICH, V. & RAWICZ, W. 2005 Automated, high-resolution micropipet aspiration reveals new insight into the physical properties of fluid membranes. *Langmuir* **21** (5), 1962–1971.
- HELFRICH, W. 1973 Elastic properties of lipid bilayers: theory and possible experiments. *Z. Naturforsch. C* **28** (11-12), 693–703.
- HU, X. Q. 2013 Biomécanique de capsules en écoulement. PhD thesis, Université de Technologie de Compiègne.
- HU, X. Q., SALSAC, A. V. & BARTHÈS-BIESEL, D. 2012 Flow of a spherical capsule in a pore with circular or square cross-section. *J. Fluid Mech.* **705**, 176–194.
- HU, X. Q., SÉVÉNIÉ, B., SALSAC, A. V., LECLERC, E. & BARTHÈS-BIESEL, D. 2013 Characterizing the membrane properties of capsules flowing in a square-section microfluidic channel: Effects of the membrane constitutive law. *Phys. Rev. E* **87** (6), 063008.

- HUANG, W. X., CHANG, C. B. & SUNG, H. J. 2012 Three-dimensional simulation of elastic capsules in shear flow by the penalty immersed boundary method. *J. Comput. Phys.* **231** (8), 3340–3364.
- I RÉ, M. 1998 Microencapsulation by spray drying. *Dry. Technol.* **16** (6), 1195–1236.
- JANSSEN, L. J. J. M. & TE NIJENHUIS, K. 1992 Encapsulation by interfacial polycondensation. i. the capsule production and a model for wall growth. *J. Membr. Sci.* **65** (1-2), 59–68.
- JOHNSTON, A. P., CORTEZ, C., ANGELATOS, A. S. & CARUSO, F. 2006 Layer-by-layer engineered capsules and their applications. *Curr. Opin. Colloid Interface Sci.* **11** (4), 203–209.
- JOUNG, S., SONG, M. & KIM, D. 2020 Synthetic capsule breakup in simple shear flow. *Phys. Fluids* **32** (11), 113603.
- KIHM, ALEXANDER, KAESTNER, LARS, WAGNER, CHRISTIAN & QUINT, STEPHAN 2018 Classification of red blood cell shapes in flow using outlier tolerant machine learning. *PLoS Comput. Biol.* **14** (6), e1006278.
- KIM, S. H., KIM, J. W., CHO, J. C. & WEITZ, D. A. 2011 Double-emulsion drops with ultra-thin shells for capsule templates. *Lab Chip* **11** (18), 3162–3166.
- KOLEVA, I. & REHAGE, H. 2012 Deformation and orientation dynamics of polysiloxane microcapsules in linear shear flow. *Soft Matter* **8**, 3681 – 3693.
- KOWALSKI, P.K., RUDRA, A., MIAO, L. & ANDERSON, D. G. 2019 Delivering the messenger: advances in technologies for therapeutic mRNA delivery. *Mol. Ther.* **27**, 710–728.
- KURIAKOSE, S. & DIMITRAKOPOULOS, P. 2011 Motion of an elastic capsule in a square microfluidic channel. *Phys. Rev. E* **84**, 011906.
- KWAK, S. & POZRIKIDIS, C. 2001 Effect of membrane bending stiffness on the axisymmetric deformation of capsules in uniaxial extensional flow. *Phys. Fluids* **13** (5), 1234–1242.
- LAC, E. & BARTHÈS-BIESEL, D. 2005 Deformation of a capsule in simple shear flow: effect of membrane prestress. *Phys. Fluids* **17**, 0721051 – 0721058.
- LAC, E., BARTHÈS-BIESEL, D., PELEKASIS, N. A. & TSAMOPOULOS, J. 2004 Spherical capsules in three-dimensional unbounded stokes flows: effect of the membrane constitutive law and onset of buckling. *J. Fluid Mech.* **516**, 303–334.

- LE, D. V. 2010 Effect of bending stiffness on the deformation of liquid capsules enclosed by thin shells in shear flow. *Phys. Rev. E* **82** (1), 016318.
- LE, D. V. & TAN, Z. 2010 Large deformation of liquid capsules enclosed by thin shells immersed in the fluid. *J. Comput. Phys.* **229** (11), 4097–4116.
- LEE, J. S. & FUNG, Y. C. 1969 Modeling experiments of a single red blood cell moving in a capillary blood vessel. *Microvasc. Res.* **1** (3), 221–243.
- LEE, P. S. & BATHE, K. J. 2004 Development of mitc isotropic triangular shell finite elements. *Comput. Struct.* **82** (11-12), 945–962.
- LEFEBVRE, Y. & BARTHÈS-BIESEL, D. 2007 Motion of a capsule in a cylindrical tube: effect of membrane pre-stress. *J. Fluid Mech.* **589**, 157.
- LEFEBVRE, Y., LECLERC, E., BARTHÈS-BIESEL, D., WALTER, J. & EDWARDS-LÉVY, F. 2008 Flow of artificial microcapsules in microfluidic channels: a method for determining the elastic properties of the membrane. *Phys. Fluids* **20** (12), 123102.
- LEYRAT-MAURIN, A. & BARTHÈS-BIESEL, D. 1994 Motion of a deformable capsule through a hyperbolic constriction. *J. Fluid Mech.* **279**, 135–163.
- LI, X. Z., BARTHÈS-BIESEL, D. & HELMY, A. 1988 Large deformations and burst of a capsule freely suspended in an elongational flow. *J. Fluid Mech.* **187**, 179–196.
- DE LOUBENS, C., DESCHAMPS, J., BOEDEC, G. & LEONETTI, M. 2015 Stretching of capsules in an elongation flow, a route to constitutive law. *J. Fluid Mech.* **767**.
- DE LOUBENS, C., DESCHAMPS, J., GEORGELIN, M., CHARRIER, A., EDWARDS-LÉVY, F. & LEONETTI, M. 2014 Mechanical characterization of cross-linked serum albumin microcapsules. *Soft matter* **10** (25), 4561–4568.
- LÉVY, M. C. & EDWARDS-LEVY, F. 1996 Coating alginate beads with cross-linked biopolymers: a novel method based on a transacylation reaction. *J. Microencapsul.* **13** (2), 169–183.
- MINETTI, C., PODGORSKI, T., COUPIER, G. & DUBOIS, F. 2014 Fully automated digital holographic processing for monitoring the dynamics of a vesicle suspension under shear flow. *Biomed. Optics Express* **5**, 1554–1568.
- MIYAZAWA, K., YAJIMA, I., KANEDA, I. & YANAKI, T. 2000 Preparation of a new soft capsule for cosmetics. *J. Cosmet. Sci.* **51** (4), 239–252.



- NAYYAR, V., RAVI-CHANDAR, K. & HUANG, R. 2011 Stretch-induced stress patterns and wrinkles in hyperelastic thin sheets. *Int. J. Solids Struct.* **48** (25-26), 3471–3483.
- NISISAKO, T. & HATSUZAWA, T. 2016 Microfluidic fabrication of oil-filled polymeric microcapsules with independently controllable size and shell thickness via janus to core-shell evolution of biphasic droplets. *Sens. Actuators B Chem.* **223**, 209–216.
- PAVLOV, A. M., SAEZ, V., COBLEY, A., GRAVES, J., SUKHORUKOV, G. B. & MASON, T. J. 2011 Controlled protein release from microcapsules with composite shells using high frequency ultrasound—potential for in vivo medical use. *Soft Matter* **7** (9), 4341–4347.
- PETROV, A. I., VOLODKIN, D. V. & SUKHORUKOV, G. B. 2005 Protein—calcium carbonate coprecipitation: a tool for protein encapsulation. *Biotechnol. Prog.* **21** (3), 918–925.
- PEYRATOUT, C. S. & DAEHNE, L. 2004 Tailor-made polyelectrolyte microcapsules: from multilayers to smart containers. *Angew. Chem. Int.* **43** (29), 3762–3783.
- POZRIKIDIS, C. 1992 *Boundary integral and singularity methods for linearized viscous flow*. Cambridge university press.
- POZRIKIDIS, C 2001 Effect of membrane bending stiffness on the deformation of capsules in simple shear flow. *J. Fluid Mech.* **440**, 269.
- POZRIKIDIS, C. 2003 *Modeling and simulation of capsules and biological cells*. CRC Press.
- POZRIKIDIS, C 2005 Numerical simulation of cell motion in tube flow. *Ann. Biomed. Engng* **33** (2), 165–178.
- QUESADA, C., DUPONT, C., VILLON, P. & SALSAC, A. V. 2020 Diffuse approximation for identification of the mechanical properties of microcapsules. *Math. Mech. Solids* .
- QUÉGUINER, C. & BARTHÈS-BIESEL, D. 1997 Axisymmetric motion of capsules through cylindrical channels. *J. Fluid Mech.* **348**, 349–376.
- RACHIK, M., BARTHÈS-BIESEL, D., CARIN, M. & EDWARDS-LÉVY, F. 2006 Identification of the elastic properties of an artificial capsule membrane with the compression test: effect of thickness. *J. Colloid Interface Sci.* **301** (1), 217–226.
- RALLISON, J. M. & ACRIVOS, A. 1978 A numerical study of the deformation and burst of a viscous drop in an extensional flow. *J. Fluid Mech.* **89** (1), 191–200.

- REHAGE, H., HUSMANN, M. & WALTER, A. 2002 From two-dimensional model networks to microcapsules. *Rheol. Acta* **41**, 292.
- RISSE, F. & CARIN, M. 2004 Compression of a capsule: Mechanical laws of membranes with negligible bending stiffness. *Phys. Rev. E* **69**, 061601–061608.
- RISSE, F., COLLÉ-PAILOT, F. & ZAGZOULE, M. 2006 Experimental investigation of a bioartificial capsule flowing in a narrow tube. *J. Fluid Mech.* **547**, 149.
- SAADAT, A., HUYKE, D. A., OYARZUN, D. I., ESCOBAR, P. V., VREEIDE, I. H. Ø, SHAQFEH, E. S.G. & SANTIAGO, J. G. 2020 A system for the high-throughput measurement of the shear modulus distribution of human red blood cells. *Lab Chip* **16**, 2927–2936.
- SECOMB, T. W. & SKALAK, R. 1982 A two-dimensional model for capillary flow of an asymmetric cell. *Microvasc. Res.* **24** (2), 194–203.
- SECOMB, T. W., SKALAK, R., ÖZKAYA, N. & GROSS, J. F. 1986 Flow of axisymmetric red blood cells in narrow capillaries. *J. Fluid Mech.* **163**, 405–423.
- SERAJUDDIN, A. T., SHEEN, P. C. & AUGUSTINE, M. A. 1986 Water migration from soft gelatin capsule shell to fill material and its effect on drug solubility. *J. Pharm. Sci.* **75** (1), 62–64.
- SHALAKA, D., NAIK, S. R., AMRUTA, A. & PARIMAL, K. 2009 Vitamin e loaded pectin alginate microspheres for cosmetic application. *J. Pharm. Res.* **2** (6).
- SHOJAEI-BAGHINI, E., ZHENG, Y. & SUN, Y. 2013 Automated micropipette aspiration of single cells. *Ann. Biomed. Eng.* **41** (6), 1208–1216.
- SKALAK, R., TOZEREN, A., ZARDA, R. P. & CHIEN, S. 1973 Strain energy function of red blood cell membranes. *Biophys. J.* **13** (3), 245–264.
- SKOTHEIM, J. M. & SECOMB, T. W. 2007 Red blood cells and other nonspherical capsules in shear flow: oscillatory dynamics and the tank-treading-to-tumbling transition. *Phys. Rev. Lett.* **98** (7), 078301.
- STASSEN, S., NIHANT, N., MARTIN, V., GRANDFILS, C., JÉRÔME, R. & TEYSSIE, P. 1994 Microencapsulation by coacervation of poly (lactide-co-glycolide): 1. physico-chemical characteristics of the phase separation process. *Polymer* **35** (4), 777–785.

- TRICKEY, W. R., BAAIJENS, F. P., LAURSEN, T. A., ALEXOPOULOS, L. G. & GUILAK, F. 2006 Determination of the poisson's ratio of the cell: recovery properties of chondrocytes after release from complete micropipette aspiration. *J. Biomech.* **39** (1), 78–87.
- WALTER, A., REHAGE, H. & LEONHARD, H. 2000 Shear-induced deformation of polyamid microcapsules. *Colloid Polymer Sci.* **278**, 169–175.
- WALTER, J., SALSAC, A. V., BARTHÈS-BIESEL, D. & LE TALLEC, P. 2010 Coupling of finite element and boundary integral methods for a capsule in a stokes flow. *Int. J. Numer. Methods Eng.* **83** (7), 829–850.
- WANG, Z., SUI, Y., SALSAC, A. V., BARTHÈS-BIESEL, D. & WANG, W. 2016 Motion of a spherical capsule in branched tube flow with finite inertia. *J. Fluid Mech.* **806**, 603–626.
- WANG, Z., SUI, Y., SALSAC, A. V., BARTHÈS-BIESEL, D. & WANG, W. 2018 Path selection of a spherical capsule in a microfluidic branched channel: Towards the design of an enrichment device. *J. Fluid Mech.* **849**, 136–162.
- YANG, Y., WEI, Z., WANG, C. & TONG, Z. 2013 Versatile fabrication of nanocomposite microcapsules with controlled shell thickness and low permeability. *ACS Appl. Mater. Interfaces* **5** (7), 2495–2502.
- YOUNGREN, G. K. & ACRIVOS, A. 1976 On the shape of a gas bubble in a viscous extensional flow. *J. Fluid Mech.* **76** (3), 433–442.
- ZHAO, C.Y. & ZHANG, G.H. 2011 Review on microencapsulated phase change materials (MEPCMs): Fabrication, characterization and applications. *Renew. Sust. Energ. Rev.* **15**, 3813–3832.
- ZHENG, YI, CHEN, JUN, CUI, TONY, SHEHATA, NADINE, WANG, CHEN & SUN, YU 2013 Characterization of red blood cell deformability change during blood storage. *Lab Chip* **14** (3), 577–583.
- ZUIDAM, N. J. & NEDOVIC, V. 2010 *Encapsulation technologies for active food ingredients and food processing*. New York: Springer.